Patricia Palenzuela
Diego-César Alarcón-Padilla
Guillermo Zaragoza

Concentrating Solar Power and Desalination Plants

Engineering and Economics of Coupling Multi-Effect Distillation and Solar Plants

Concentrating Solar Power and Desalination Plants

Patricia Palenzuela • Diego-César Alarcón-Padilla •
Guillermo Zaragoza

Concentrating Solar Power and Desalination Plants

Engineering and Economics of Coupling
Multi-Effect Distillation and Solar Plants

$\textcircled{2}$ Springer

Patricia Palenzuela
CIEMAT—Plataforma Solar de Almería
Tabernas, Almería
Spain

Diego-César Alarcón-Padilla
CIEMAT—Plataforma Solar de Almería
Tabernas, Almería
Spain

Guillermo Zaragoza
CIEMAT—Plataforma Solar de Almería
Tabernas, Almería
Spain

Contents

Chapter 1
State of the Art of Desalination Processes

Nomenclature

Acronyms

DE	External diameter
DEAHP	Double-effect absorption heat pump
DI	Internal diameter
ED	Electrodialysis
HTE	Horizontal tube evaporator
IDA	International Desalination Association
LT-MED	Low-temperature multi-effect distillation
MED	Multi-effect distillation
BF-MED	Backward-feed multi-effect distillation
FF-MED	Forward-feed multi-effect distillation
MVC-MED	Mechanical vapour compression multi-effect distillation
PF-MED	Parallel-feed multi-effect distillation
P/C-MED	Parallel/cross multi-effect distillation
MED-TVC	Multi-effect distillation with thermal vapour compression
MES	Multi-effect stack
MSF	Multi-stage flash
MVC	Mechanical vapour compression
OECD	Organisation for Economic Co-operation and Development
RO	Reverse osmosis
PSA	Plataforma Solar de Almería
TVC	Thermal vapour compression
VTE	Vertical tube evaporator

Variables

GOR   Gain output ratio
PR   Performance ratio
TDS   Total dissolved solids (mg/L)
TBT   Top brine temperature (°C)

1.1 Introduction

The integration of the desalination processes into Concentrating Solar Power Plants (CSP+D) is nowadays the best alternative to solve simultaneously the water scarcity problems and the depletion of fossil fuels. Most of the regions facing fresh water shortages have high insolation levels and are located close to the sea, with more than the 70 % of the world population living in a 70 km strip bordering the sea. Therefore, the use of solar energy for the simultaneous fresh water and electricity production is maybe the most sustainable solution. The combined production can be made either by using electricity from the CSP plant for a mechanical desalination process or by using the thermal energy to drive a thermal desalination process. This chapter presents the state of the art of desalination processes more suitable to be used in the simultaneous production of electricity and fresh water by concentrating solar power and desalination plants.

1.2 Available Technologies for Large-Scale Seawater Desalination

Many regions of the world are now suffering from water scarcity, and forecasts suggest that this will reach a critical level within the first half of this century as a result of a variety of factors, such as the increase in world population, living standards and water resource contamination. Nowadays, around 25 % of the world's population has no access to fresh water, and more than 80 countries are facing water scarcity issues serious enough to risk their economic development. Moreover, climate change and climatic variability can have a dramatic impact on water supplies, the most obvious being drought (US DoE 2006); this might even affect countries that, as yet, are not experiencing problems. By 2030, 47 % of the world's population will be living in areas of high water stress, and more than five billion people (67 %) may still be without access to adequate sanitation (OECD 2008).

Desalination is considered to be one of the most suitable options for tackling these water scarcity issues. Of the 1.4×10^{12} m^3 of water reserves on the planet, 97.6 % is salt water. Of the remaining 2.4 % of fresh water, only 1 % is in the form of liquid on the earth's surface and therefore available for human consumption—a mere 0.024 % of global water resources (Manahan 1997). Seawater desalination is particularly crucial for Middle-Eastern countries such as Saudi Arabia, the United Arab Emirates and Kuwait (Alawadhi 2002). According to the International Desalination Association, the worldwide contracted capacity of desalination plants has

reached 90.1×10^6 m³/day. This is a rise of 1×10^6 m³/day compared with 80.47×10^6 m³/day for the previous period (Pankratz 2014). Figure 1.1 shows the total worldwide capacity by feedwater category.

The desalination process consists of separating salt water flow (seawater or brackish water) into two output streams: the distillate (free of salts) or the permeate (with a low dissolved-salt content) and the brine, which is a concentrated salt solution. It is an endothermic separation process so it requires a considerable amount of energy (see Fig. 1.2).

Desalination processes can be split into two main categories: (1) thermal processes including multi-stage flash (MSF), multi-effect distillation (MED) and mechanical vapour compression (MVC); and (2) membrane processes including reverse osmosis (RO) and electrodialysis, which is limited to brackish water.

Desalination processes can also be classified into two other categories: first, by the type of energy used in the process and, second, by the type of physical process (see Table 1.1). Desalination process efficiency is characterised by the specific energetic consumption, whether thermal or electric (or both), depending on the energy source required.

Fig. 1.1 Available worldwide desalination capacity based on feedwater sources (Pankratz 2014)

Pure water 4%
Wastewater 6%
River water 9%
Brakish water 22%
Seawater 59%

Fig. 1.2 Desalination process

Energy

Seawater or brackish water → Desalination device → Fresh water

Brine
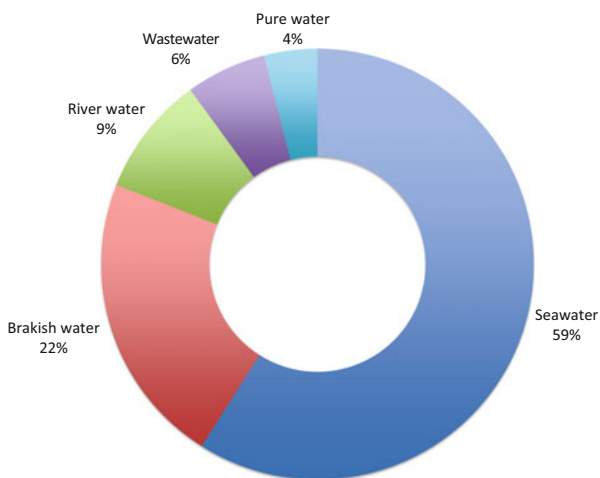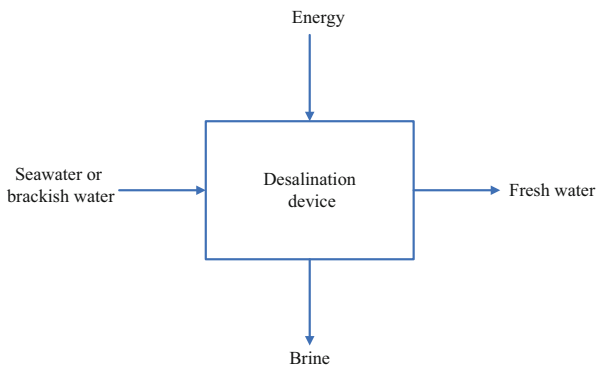
Table 1.1 Desalination process classification (Valero et al. 2001)

Energy	Process	Method
Thermal	Evaporation	Multi-stage flash (MSF)
		Multi-effect distillation (MED)
		Thermal vapour compression (TVC)
		Solar still
	Crystallisation	Freezing
		Hydrate formation
	Filtration and evaporation	Membrane distillation
Mechanical	Evaporation	Mechanical vapour compression (MVC)
	Filtration	Reverse osmosis (RO)
Electrical	Selective filtration	Electrodialysis (ED)
Chemical	Exchange	Ionic exchange (IE)
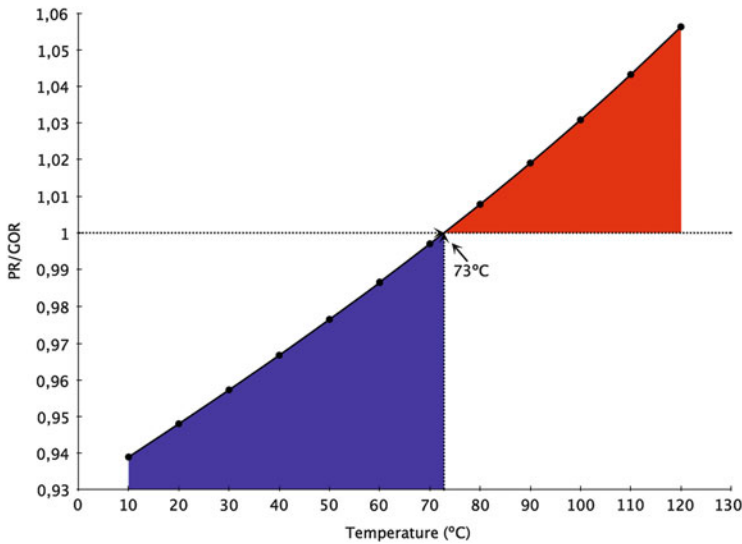
Fig. 1.3 Comparison of the gain output ratio (GOR) and performance ratio (PR) parameters as a function of temperature

Besides this, in thermal desalination processes, efficiency can be determined by two parameters: the performance ratio (PR) and the gain output ratio (GOR). The latter is a dimensionless parameter defined as the mass ratio between the distillate produced and the steam supplied to the system. The former is defined as the ratio between the mass of distillate (in kg) and the thermal energy supplied to the process normalized to 2326 kJ (1000 Btu) that is the latent heat of vaporization of water at 73 °C. This parameter is more general because it allows characterisation of not only steam-driven processes but also those driven by the sensible heat of a thermal fluid. Even though they are not strictly the same, the differences between PR and GOR are very small, as seen in Fig. 1.3, which also shows that both parameters match at a temperature of 73 °C.

Fig. 1.4 Total worldwide installed capacity by technology (Pankratz 2014)
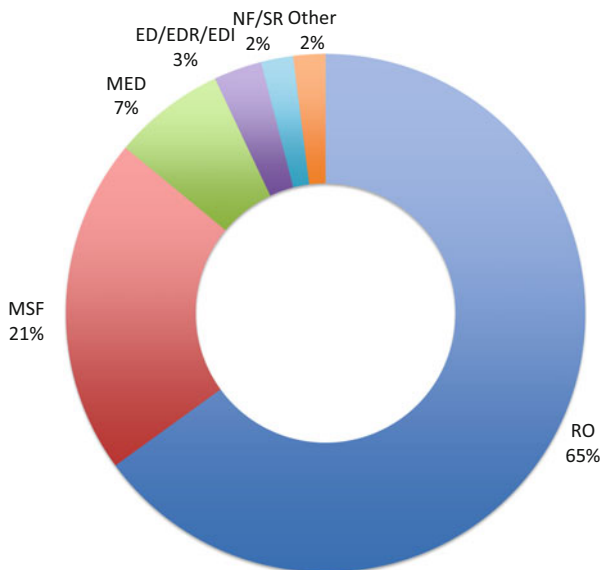
Another typical parameter characterising desalination processes is the conversion factor, which is defined as the ratio between the volume of distillate and the volume of feedwater supplied to the plant. Thus, the lower the conversion factor, the higher the specific electricity consumption is (as a result of higher pumping requirements) and the larger the amount of chemical products used (for pretreatment).

The most important industrial desalination processes are MSF, MED and RO. The RO process has the highest worldwide installed capacity followed by MSF. Figure 1.4 shows the total worldwide installed capacity, categorised by technology, according to the *IDA Desalination Yearbook 2014–2015* (Pankratz 2014). Although the MED process began before MSF and is more efficient from a thermodynamic point of view, it was pushed into the background because of the high working temperatures and the materials used (to increase capacity), which caused scaling problems in the heat exchangers, thus decreasing performance. These problems, together with those caused by corrosion, led to the abandonment of MED as a thermal desalination process. However, over the last few decades, technological development of MED processes at low temperature have made it more competitive with respect to MSF technology. Examples of this are the construction of large-capacity MED plants, such as the one installed in Marafiq (Saudi Arabia) with a total production of 800,000 m^3/day (27 units of 30,000 m^3/day each) (Pankratz 2009a).

The following subsections give a brief description of the most important desalination processes.

1.2.1 Multi-stage Flash

The MSF process is based on vapour generation from either seawater or brine as it enters a chamber, called stage, which is at a lower pressure than its saturation pressure. There is flash evaporation, produced instantaneously and violently. This evaporation takes place until the saltwater temperature reaches equilibrium with the stage pressure. Only one part of the water entering the stage is turned into steam while the remaining part becomes more concentrated in salts. This process is repeated in the rest of the stages, which are at decreasing pressures.

There is a heat exchanger in each stage, within which the vapour generated by flash evaporation condenses, transferring its phase-change enthalpy to the seawater or brine, which, in turn, is preheated on its way to the first stage. The preheated seawater leaves the first stage, increasing its temperature to its maximum value (top brine temperature, TBT) of 90–110 °C in a heat exchanger called a brine heater (Buros 2000); this is the only element in the desalination process with an external energy source. A heat exchanger of this type can use saturated vapour from either a boiler or a power plant (via a steam turbine) at 0.7–1.7 bar (Baig et al. 2011). The condensed steam from the outside part of the preheaters in each stage makes up the plant's distillate production. Figure 1.5 shows a scheme of the MSF evaporation process with brine recirculation.

A vacuum system is used to remove the air and to make the generated steam temperature in the stage correspond to its saturation pressure. This can be done by steam ejectors, hydro-ejector or a vacuum pump. Such a system is also employed for removing the non-condensable gases generated in the plant during the evaporation process. If these gases are not removed, the presence of a gas film at the interface reduces the partial pressure of the steam, heat transfer is more difficult and the steam condensation temperature is reduced.

The MSF process is especially suitable for the desalination of poor quality water (high salinity, temperature and pollution) because the system is robust enough to tackle adverse conditions. Therefore, it is used more in regions such as the Persian Gulf, particularly in Saudi Arabia, the United Arab Emirates and Kuwait.
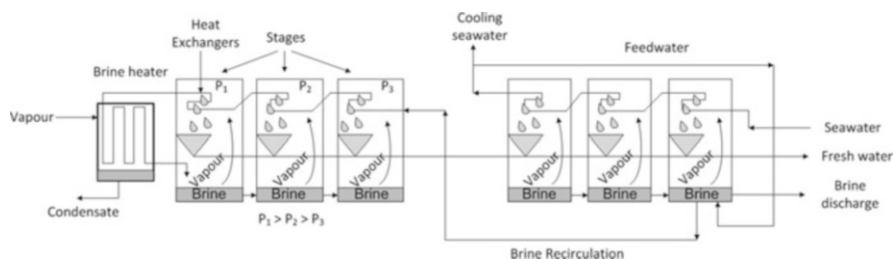
Fig. 1.5 Multi-stage flash evaporation process

MSF plants have been in use since 1950 (Buros 1980) and the Shoaiba 3 IWPP plant has the greatest capacity at present. This plant is situated in Saudi Arabia and has a fresh water production of 880,000 m^3/day (Pankratz 2009b).

1.2.2   Multi-effect Distillation

In order to understand the MED process, the operation of a distillation plant with only one effect (or stage) is shown first (see Fig. 1.6). The main components of this kind of plant are the evaporator and the condenser or preheater.

The evaporator is the component in which the external heat source transfers its thermal energy to the process. The heat source can be either a liquid or steam, coming from a power plant or a boiler. The hot fluid (liquid or steam) transfers its energy to the seawater that is being sprayed over the first tube bundle row (feedwater), forming a thin film of water. The seawater is heated to its boiling point, evaporating part of it. The vapour generated flows to the condenser through a demister and there condenses, transferring its latent heat to the seawater circulating inside the condenser's tube bundle. The demister stops brine droplets mixing with the generated vapour, or with the final product. Also, it prevents the condenser tube bundle from being exposed to brine, thus avoiding scaling problems, tube corrosion and, as a consequence, a reduction in heat transfer. Finally, the distillate (corresponding to the condensed vapour) and the resultant brine (non-evaporated brine and therefore more concentrated in salts than the original feedwater) are
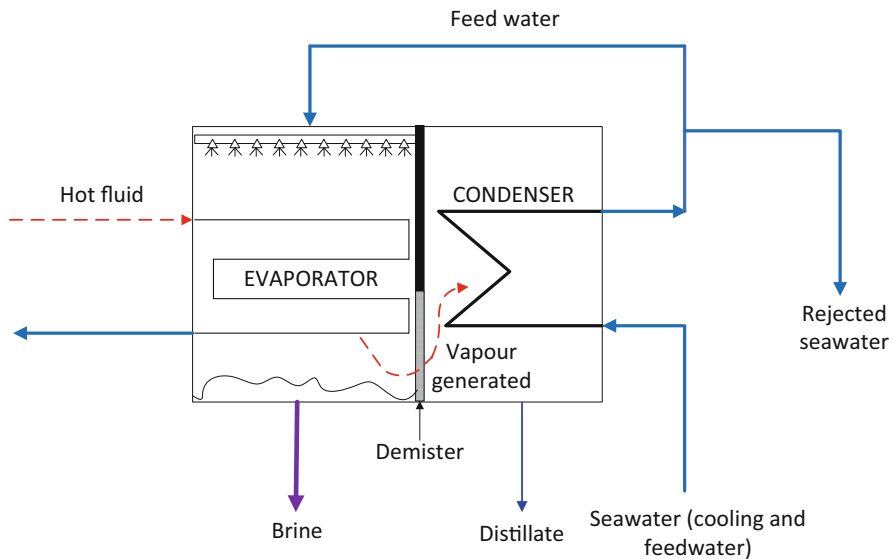
Fig. 1.6 Single-effect distillation plant
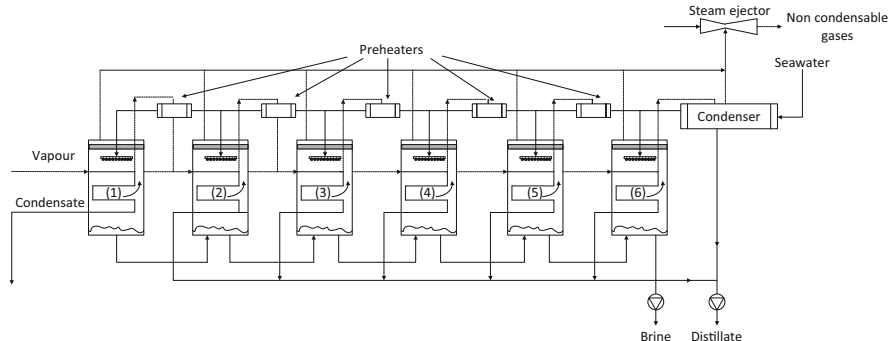
Fig. 1.7 Multi-effect distillation process

obtained as final products. The function of the cooling water in the condenser is to remove excess heat added to the system in the evaporator by the heating steam. This implies that the evaporator does not consume all the supplied heat, but does degrade its quality. As shown in Fig. 1.6, the remaining seawater not used as feedwater is discharged back to the sea. The distillation plant shown in Fig. 1.6 has a very low performance, so, in order to improve this, several effects or stages are connected in series to give place to an MED plant. In the MED process (see Fig. 1.7), the vapour obtained from each stage is used as the heat source for the next, but at a lower temperature and pressure than the stage before. Thus, there are simultaneous evaporation and condensation processes in each stage, or effect, at decreasing temperatures (and their corresponding saturation pressures). Only one external heat source is needed for the MED process, which enters the first effect tube bundle at the highest temperature. The vapour condensed inside each of the tube bundles from the second to the last effect makes up the global MED plant distillation.

The vapour condensation produced in the last effect takes place in a tube bundle located at the end of the process and called the end condenser. This is cooled by seawater so the feedwater is slightly preheated before the beginning of the desalination process. As an energy optimisation process, as the distillate and brine go from one effect to the next, part of each evaporates by flashing because the temperature of brine or distillate flowing from the previous effect is higher than the saturation temperature of the subsequent effect (Soteris 1997). Finally, the brine from the last effect is discharged to the sea.

The TBT in MED plants is 70 °C in order to avoid scaling and reduce corrosion problems (Khawaji et al. 2008). This temperature also avoids the use of sophisticated chemical pretreatments (as in the case of MSF) and only minimal antiscaling is needed. Scaling is the accumulation of inorganic salts such as calcium carbonate, calcium sulphate and magnesium hydroxide on the external surface of the tube bundles. The solubility of these salts decreases as the temperature increases, so at lower temperatures there are fewer scaling problems. Such plants are known as low temperature multi-effect distillation (LT-MED) plants.

MED processes require vacuum systems as do MSF processes. These can be steam ejectors, hydro-ejectors or a vacuum pump.

The MED process can be configured according to the way the tubes in the tube bundles are arranged, the seawater flow direction and the layout of the effects.

Tube bundles can be submerged tube evaporators, rising film vertical tube evaporators (VTE), falling film VTEs, rising film horizontal tube evaporators (HTEs), rising film HTEs or plate heat exchangers. In submerged tube evaporators, vapour enters the tubes, which are surrounded by seawater. The first commercial MED plants used these evaporators with two or three effects. The problems with submerged tube evaporators were their low heat transfer and their high propensity for scaling. The problems were overcome by maintaining a thin liquid film over the exchange surface, as with VTEs and HTEs. In VTE systems, the brine is evaporated inside the tubes and vapour is condensed outside. In HTE systems, brine is evaporated outside the tubes and vapour condenses inside. Another type of heat exchanger is that based on titanium plates; these were introduced to the industry by the company Alfa Laval Water Technologies (Denmark) (Legorreta et al. 1999). The exchangers consist of a number of corrugated titanium plates especially developed for desalination. All the plates are similar; however, there are two gasket configurations, one for plates forming the evaporator plate channels and another for plates forming the condensing plate channels. A crosscurrent flow between vapour and brine, crossing alternate channels, allows a high heat transfer coefficient.

Most MED plants have the falling film HTE configuration (El-Nashar 2000). The falling film is formed by spraying the brine through nozzles or trays. The condensation and evaporation processes on both sides permit high heat transfer coefficients, especially in corrugated tubes. As the vapour enters one side of the tube and the condensate leaves the other, the HTE configuration makes the non-condensable gases flow outside the heat exchange area. In addition, it creates stable operating conditions and decreases the residence time required for scale formation (Nafey et al. 2006).

MED plants can also be classified by the seawater flow direction: forward feed plants (FF), backward feed plants (BF) and parallel feed plants (PF). There are also hybrid configurations such as parallel/cross feed (P/C) plants.

In FF-MED plants, both feedwater and vapour flow in the same direction. Feedwater goes to the first effect (which has the highest temperature) then passes through each subsequent effect until reaching the last, from which it enters the end condenser. In BF-MED plants, feedwater and vapour travel in opposite directions. Feedwater is directed from the end condenser to the last effect (which has the lowest temperature) and then passes through each effect until reaching the first. The problem with this configuration is that the highest brine concentration occurs in the first effect, which is at the highest temperature, thus increasing the risk of scale formation. Another disadvantage is that the seawater pumping from one effect to another is at a higher pressure, increasing operating costs and maintenance as well as increasing the incidence of air leaks through the pump connections (Breidenbach et al. 1997). An advantage of this configuration is that it does not need preheaters so the capital costs are lower. In the PF-MED plants, feedwater leaving the end

condenser is split and distributed uniformly to each effect. The main advantage of this configuration is its simplicity and the lower risk of scale formation compared with the FF-MED and BF-MED configurations.

Most commercial MED plants are forward feed because the brine with the lowest concentration is at the highest temperature (in the first effect) and that with the highest concentration is at the lowest temperature (in the last effect). This avoids the risk of scale formation (Morin 1993). Nafey et al. (2006) carried out a thermo-economic analysis, comparing FF-MED and P/C-MED systems, and found that the PR for the former was 42 % higher than for the latter. On the other hand, it was shown that the energetic efficiency in the FF-MED configuration was 17 % higher than in the P/C configuration. As a result, the water cost for the FF-MED was 40 % lower than for the P/C-MED configuration with the same number of effects. In order to improve the FF-MED performance, seawater pre-heaters can be used. They consume a fraction of the vapour generated in each effect, meaning that the feedwater reaches the first effect at a suitable temperature.

Depending on the arrangement of the effects, MED plants can be horizontal or vertical (multi-effect stack, MES). Higher capacity MED plants are generally horizontal because of their stability and their operational and maintenance simplicity. Vertical MED plants have lower capacities. They can be a simple-stack arrangement, in which the evaporators are piled one on top of the other, or a double-stack arrangement, in which the effects are piled in two groups; for example, the effects 1, 3, 5, etc. are piled on top of each other in one group, while effects 2, 4, 6, etc. are piled on top of each other in another group, parallel to the first. The main difference between horizontal and vertical arrangements is that, in the latter, the brine flows under gravity from the effects at higher temperature towards the bottom with no additional pumping between stages. Morsy et al. (1994) compared a horizontal and vertical MED plant and found that the heat transfer area in the horizontal configuration was roughly double that required by the vertical configuration. The capital and maintenance costs of MES plants are lower than in other designs because only one pump is necessary to feed the process. Other important characteristics of MES plants are the lower occupancy area, higher heat transfer coefficient and great stability in partial-load operation (Morsy et al. 1994). Generally, the thermal efficiency of the process and the operating and capital costs are directly related to the number of MED plant stages: the higher the number of stages, the lower the energetic consumption is and the higher the capital costs.

An example of the implementation of a vertical arrangement MED plant is at the Plataforma Solar de Almería (PSA). A pilot plant driven by solar energy was built in 1988 within the STD Project (Solar Thermal Desalination, 1988–1994) framework, the aim being to prove the technical viability of incorporating thermal solar energy into desalination processes. The plant is a FF-MED plant with 14 stages. The original first effect worked with low-pressure saturated steam (70 °C, 0.31 bar) from a parabolic-trough solar field (Gregorzewski et al. 1991). An assessment of the plant working as a LT-MED gave a PR of between 9.4 and 10.4 (Zarza 1994). In 2005, it was replaced by a newer version able to work with hot water as the heat transfer medium (Alarcón-Padilla et al. 2007). The required heat for the first cell is

Fig. 1.8 Multi-effect distillation plant, storage system and compound parabolic collectors solar field at the Plataforma Solar de Almería

provided either by a solar field composed of static compound parabolic collectors (CPC) and a storage system composed of two tanks of 24 m^3 capacity or by a double-effect absorption heat pump (DEAPH; using LiBr-H$_2$O as absorption fluid) manufactured by Entropie in 2005 as part of the AQUASOL project framework. Assessment of the MED plant driven by hot water as the thermal energy source gave a PR of between 10.5 and 11, with a TBT of 64–67 °C. These conditions were the most optimal for the first-effect tube bundle (Blanco et al. 2011). Figure 1.8 shows the components of the AQUASOL system at the PSA.

The first commercial venture using MED was in Kuwait, with a three-effect plant and submerged tube evaporators; however, the plant experienced serious scaling problems. The plant was built in 1950 (Darwish et al. 2006).

The first MSF plant was installed in the 1960s, and became the prevailing process because of the simpler process for elimination of salt precipitation than in MED plants. At present, the thermal seawater desalination industry continues to be dominated by the MSF process. However, in recent years, the MED process has experienced significant developments and researchers predict that, in the near future, it will dominate the thermal desalination market (Torzewski and Müller 2009). MED process efficiency can be improved in one of two ways. The first way
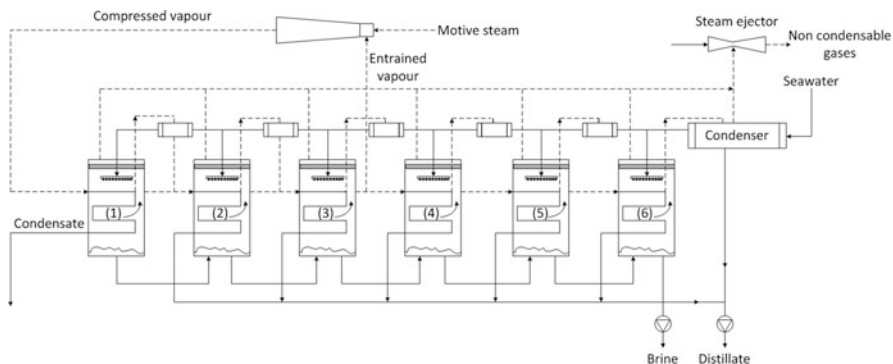
Fig. 1.9 Multi-effect distillation process with thermocompression

is to use compressed steam, whereby part of the steam formed in the MED process is extracted from the plant, recompressed and then reintroduced into the first effect. This steam compression can be thermal (TVC) or mechanical (MVC). The second way is to increase MED plant output by coupling it to an absorption heat pump. In industrial-scale MED plants, the process most commonly used to increase energy efficiency is MED with thermal vapour compression (MED-TVC), using steam ejectors (see Fig. 1.9). In this configuration, the compressor is a steam ejector (also called thermocompressor), which is fed on the one hand by medium-pressure steam (3–20 bar), called motive steam (which can come from a power plant or from a boiler), and on the other hand by low-pressure steam, known as entrained vapour, which is extracted by one of the MED plant effects and thus its pressure depends on the effect in which the extraction is made. This mixture is introduced into the ejector, creating a steam (called compressed steam) with pressure between those of motive steam and entrained vapour, which is introduced into the MED first effect. The relative flows of motive steam and entrained vapour depend on the respective pressure values and on the convergent/divergent design of the ejector nozzles.

The integration of a steam ejector into a MED plant reduces the number of effects necessary compared with LT-MED (for a required efficiency) because the process is thermodynamically more efficient. This means that the thermal energy required by the process (in the form of motive steam) to produce the same amount of fresh water is considerably less. For the same number of effects, the GOR for the MED systems can be increased by around 20 % by coupling to a steam ejector (Morin 1993), resulting in GOR values of up to 16 (Amer 2009). Regarding specific electricity consumption, this is lower in MED-TVC than in LT-MED because, when extracting steam for recompression, the amount of seawater that has to be pumped through the plant's final condenser is less. Typical specific electricity consumption values are found in the 1.5–2.5 kWh/m^3 range (Trieb 2007). The first two commercial MED-TVC plants (with two effects in each unit) were introduced in 1973 on Das Island (United Arab Emirates), with a 125 m^3/day capacity (Amer 2009). The plant located in Marafiq (Saudi Arabia) is a

MED-TVC plant and has a capacity of 800,000 m³/day (27 units of 30,000 m³/day each) (Pankratz 2009a).

The PSA has also researched and developed MED thermocompression systems with steam ejectors. For this, during phase I of the STD project, the coupling of thermocompressors to the MED plant was tested. As a thermal energy source, high-pressure steam was used (16–26 bar), generated from a small power plant coupled to the parabolic-trough collector solar field. A small amount of this steam was directed to a set of two ejectors placed in series, where the motive steam was mixed with the steam extracted from cell 14 of the MED plant. Evaluation of this configuration showed an increase in the PR with respect to the system with no thermocompression, obtaining values of between 12 and 14 (Zarza 1994).

A steam ejector is like a heat pump, although it is a very inefficient heat pump, given the physical nature of the process taking place in its interior. To improve PR values, more efficient heat pumps can be coupled to the MED systems. During the second phase of the STD project, a Double-effect absorption heat pump (DEAHP) with LiBr-H₂O was coupled to the MED plant to considerably reduce the specific cost of distillate produced by the system. The heat pump was capable of supplying 200 kW of thermal energy to the MED plant at 65 °C. The desalination process used 90 kW of these 200 kW, while the remainder (110 kW) was recuperated by the heat pump evaporator at 35 °C and pumped at an operating temperature of 65 °C. To do this, the pump required 90 kW of thermal energy at 180 °C (10 bar absolute). The result was a reduction in the energy consumption of the entire system from 200 to 90 kW (Zarza 1994). This 65 % reduction in thermal energy consumption led to an increase in the PR value to 20 (Zarza 1994). More recently, within the AQUASOL project framework, a new DEAHP prototype was developed (see Fig. 1.10). The main difference with respect to the previous pump was that this second prototype was designed to provide hot water to the MED plant's first effect. This was an

Fig. 1.10 Double-effect absorption heat pump located at the Plataforma Solar de Almería
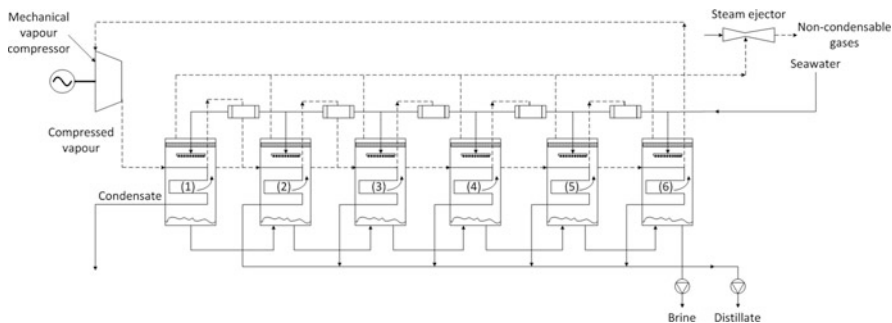
Fig. 1.11 Multi-effect distillation process with mechanical vapour compression

attempt to solve the problems that had occurred in the STD project in extracting heat from the pump when the MED plant was working with saturated steam. The experimental evaluation of this coupling demonstrated its technological advancement, achieving a PR of 21 (Alarcón-Padilla et al. 2007, 2008, 2010; Alarcón-Padilla and García-Rodríguez 2007).

MED plant evaporators can also be coupled to an MVC process (MED-MVC). In this configuration, the steam extracted from the MED plant is compressed in a mechanical vapour compressor and then used as a heat source in the first effect. The vapour compression process increases the steam pressure and, therefore, its saturation temperature becomes slightly higher (around 5 °C) than the vapour temperature generated in the first effect. This temperature difference is necessary for heat transfer in this effect (see Fig. 1.11). The advantage of the MED-MVC system is that it does not need steam and only mechanical energy is required for the compression. Its main limitation is the minimal capability of the compressors to obtain the steam needed in the MED plant, because its size is limited by the availability of the entrained vapour flow rates. Another drawback is the high electricity consumption, with values of between 8 and 15 kWh/m^3 (Sidem Entropie 2008).

In 2000, MED-MVC units with six effects were developed with a capacity of up to 5000 m^3/day (Wangnick 2000). The capacity of these plants can be increased by using a multi-stage compressor, reaching capacities of up to 10,000 m^3/day (Ophir and Gendel 2000).

Another option for augmenting MED plant yields is combining them with other desalination processes to give "hybrid desalination systems". Nafey et al. (2006) described a combined MED/MSF system, where each module is formed by a flash evaporator (MSF) and an evaporator where seawater is boiled (MED). The thermo-economic analysis carried out by Nafey showed that the operating cost decreased with an increase in the number of modules. However, the capital investment cost also increased. A comparison between MSF (20 stages), FF-MED (10 effects) and a hybrid MED-MSF system (10 modules) showed that the unitary production cost of the hybrid system was 31 % less than the MSF system and 9 % less than the FF-MED system.

1.2.3   Reverse Osmosis

Osmosis is a special form of diffusion and occurs when two solutions of different concentrations are separated by means of a semipermeable membrane. The system allows diffusion of part of the dissolvent through the membrane, from the less concentrated to the higher concentrated solution, until it reaches the so-called osmotic equilibrium. The process can best be illustrated by considering two compartments separated by a semipermeable membrane, with pure water in one and the same amount of salt water in the other (Fig. 1.12a). Because of osmosis, the pure water penetrates the membrane but the salt does not pass through (Fig. 1.12b). As a result, the liquid level in the compartment with the saline solution increases because of the pure water flow, causing a reduction in its salt concentration. Once equilibrium is reached, the difference in the levels observed corresponds to the osmotic pressure value of the saline solution.

   If an external pressure is applied to the saline solution that is greater than the osmotic pressure, a physical phenomenon called reverse osmosis (RO) takes place whereby water flows in the opposite direction to the natural physical process, leaving the saline solution at a more elevated concentration (see Fig. 1.12c).

   In an industrial RO process, a high-pressure pump is used to overcome the osmotic pressure (see Fig. 1.13). In this way, part of the water (the permeate) passes through the membrane, eliminating most of the saline ions. The rest of the water, together with the remaining saline ions, is rejected at high pressure and constitutes the brine. The greater the feedwater salt content, the greater the pressure required in the high-pressure pump and the lower the conversion factor.

   The lifetime of the membranes is from 3 to 5 years. Membranes are sensitive to PH, oxidation, a wide range of organic compounds, algae, bacteria, deposition of particles and fouling in general. Therefore, feedwater pretreatment is required prior to the separation process in order to prolong the life of the membrane and prevent fouling, as this is the main limiting factor in osmosis application.
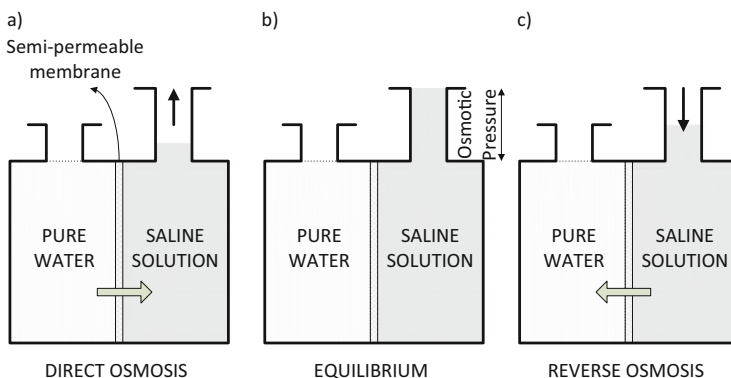
Fig. 1.12 Explanation of the reverse osmosis process
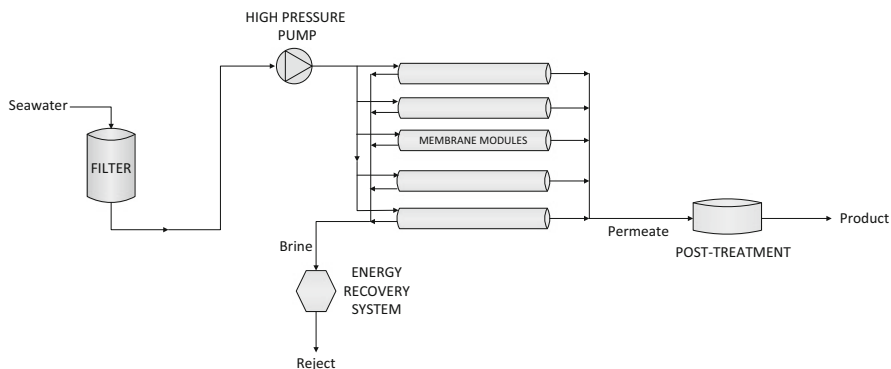
Fig. 1.13 Reverse osmosis plant

Fouling is the process by which a membrane suffers from decreased output as a result of a physical and/or chemical change caused by the presence of any minority component or contaminant in the fluid (Noble and Stern 2003). Membrane fouling can occur for different reasons. One reason is that colloidal particulates stick to the membrane surface. Fouling also occurs when the solution reaches saturation point and produces precipitation of solutes such as calcium carbonate ($CaCO_3$), calcium sulphate ($CaSO_4$), iron(III) hydroxide [$Fe(OH)_3$] and silicon dioxide (SiO_2) (Huang and Ma 2012). Moreover, if biological agents are present, they can be absorbed or adsorbed by the membranes (Noble and Stern 2003).

There are two types of seawater pretreatments used before passing water through the membrane. The classic pretreatment consists of simple mechanical cleaning using sieves, sand filters and filter cartridges to eliminate colloids, suspended solids, impurities, particulates, etc. This cleaning procedure is combined with exhaustive chemical treatments using chlorine to reduce fouling by biological agents and antiscalants to eliminate salt precipitates. Both treatments need long operating times, consume chemical products, degrade certain membranes and can cause system corrosion (Madaeni and Samieirad 2010). To avoid these drawbacks, there is another alternative: the use of ultrafiltration or microfiltration, both of which result in greater output (Bonnélye et al. 2008; Brehant et al. 2002). The difference between them is the membrane pore size, which determines the point to which the dissolved solids, turbidity and microorganisms are eliminated. The membranes used in microfiltration have a 0.1–10 μm pore size and are used to eliminate sand, clay, algae and bacteria. Membranes used in ultrafiltration have a pore size of 0.001–0.1 μm and are often used to eliminate sand, clay, algae, bacteria and viruses. The advantage, therefore, of ultrafiltration and microfiltration methods is that consumption of chemical agents is reduced (thus minimising environmental impact) and greater elimination of bacteria is achieved (Chua et al. 2003; Ebrahim et al. 2001; Vial and Doussau 2003). Furthermore, a recently used method employed in seawater pretreatment was the use of nanofiltration membranes

(Soteris 2005). These have an even smaller pore size than those mentioned above (between 0.001 μm and 1 nm) and are used for the elimination of water hardness, organic material and bacteria as well as for lowering the operating pressure of the RO process by reducing the total dissolved solids in feedwater.

Pretreatment can have a significant impact on both the cost and energy consumption of the RO process, although the main energy cost comes from pressurisation of the saline solution. Because osmotic pressure is directly related to salt concentration, the energy consumption is less in the case of brackish waters and, as a result, membrane processes are more advantageous than thermal distillation processes (in which the energy consumption is hardly influenced by the salt concentration present in the feedwater). The operating pressure is in the 15–20 bar range for brackish waters and 50–80 bar for seawater, depending on the feedwater concentration (Khawaji et al. 2008). For example, for typical salt concentrations in the Atlantic Ocean, pressures of between 60 and 70 bar are generally used.

Another factor that has a negative effect on RO membranes is concentration polarisation. This refers to the concentration gradient of salts on the high-pressure side of the RO membrane surface, which is created by the less-than-immediate re-dilution of salts left behind as water permeates through the membrane. The salt concentration in this boundary layer exceeds the concentration of the bulk water. This phenomenon impacts the performance of the RO process by increasing the osmotic pressure at the membrane surface. Moreover, given that the transfer of salts is proportional to the concentration difference on both sides of the membrane, an increase in the transfer is also produced. Another negative consequence is the precipitation of low-solubility salts if their concentration at the boundary layer exceeds the saturation point. To avoid this polarisation, turbulence in the feedwater current should be increased by increasing the flow rate. The two most common types of RO membrane used commercially are the spiral-wound membrane and the hollow-fibre membrane (Malaeb and Ayoub 2011) because of their economic efficiency (Kumano et al. 2008). They are both densely packed, which makes the permeate flow high. However, they are also highly prone to fouling.

Hollow-fiber RO membranes are constructed of hollow tubes the size of a human hair (42 μm internal diameter (DI), 85 μm external diameter (DE)). They are arranged in a U-shaped group in a cylindrical bundle around a central tube through which the feedwater is distributed. The ends of the fibres are inserted in epoxy resin connected to the outlet. The salt water passes through the distribution tube and across the outside of the fibres. Pure water passes through the membranes and enters each of the hollow fibres. The permeate is collected at the open end (see Fig. 1.14).

Spiral-wound membranes consist of a semipermeable rectangular membrane lamina folded in half in such a way that the active layer faces outwards, with a porous support fabric inserted inside. The ends of the membrane are closed on three sides to form a flexible envelope. Above the membrane's active layer there is a mesh, covered in distribution channels to spread the saline solution uniformly over the entire membrane surface. The multi-layered envelopes are wrapped around a central tube, forming a spiral configuration. The feedwater passes into the porous
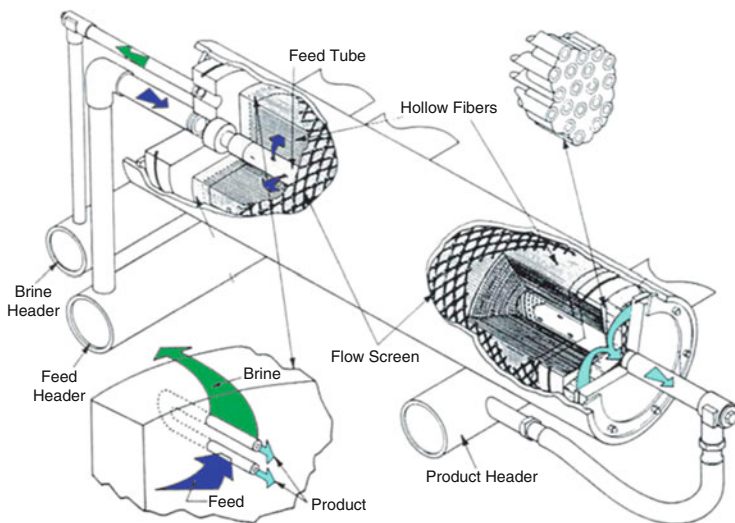
Fig. 1.14 Hollow-fiber module
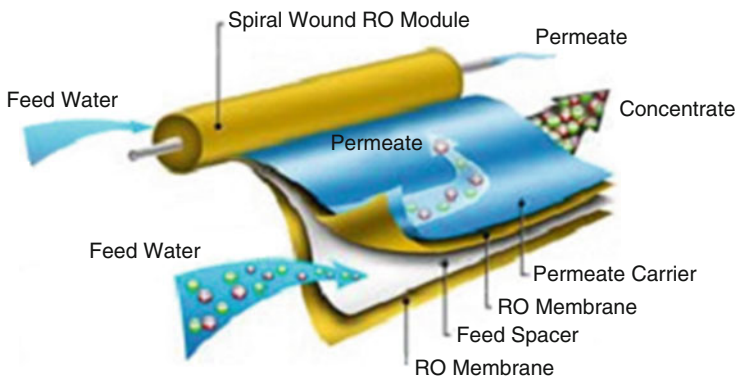
Fig. 1.15 Spiral-wound reverse osmosis module

fabric and through the membrane, accessing the perforated central tube where it is collected and extracted from the system (see Fig. 1.15). The most commonly used materials in RO membrane manufacture are cellulose triacetate and polyamide (Khawaji et al. 2008).

The RO post-treatment process normally consists of pH adjustment, addition of Ca and Na salts in the form of lime, elimination of dissolved gases such as H_2S and CO_2, and disinfection.

Two advances that have helped to reduce RO plant operating costs over the past decade are the development of membranes that operate more efficiently and for longer (Jeong et al. 2007; Kumar et al. 2007; Smuleac et al. 2004; Wiesner and Chellam 1999) and the use of energy recovery devices (ERD) (Childs and Dabiri
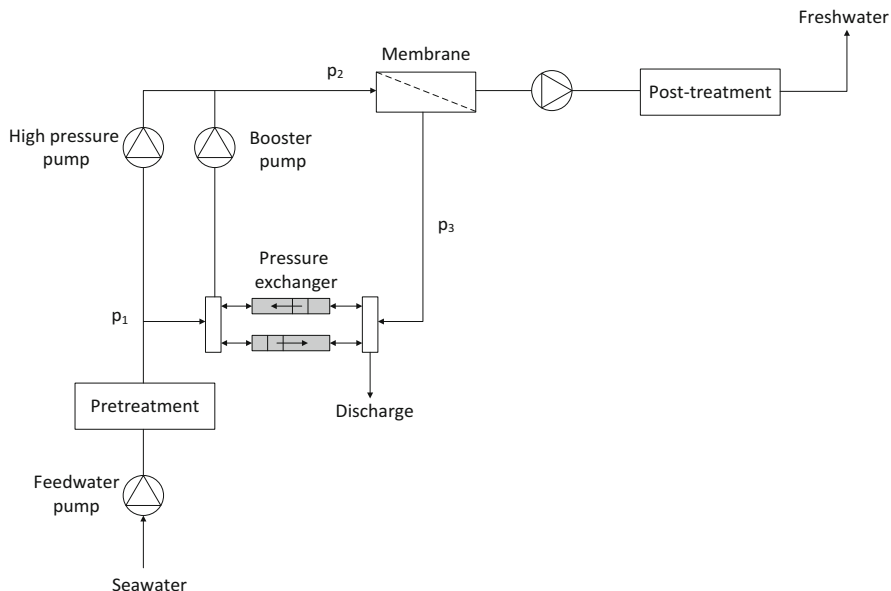
Fig. 1.16 Layout of a reverse osmosis plant with a pressure exchanger as the energy recovery system

1999; Duranceau et al. 1999; Gruendisch 1999; Leidner et al. 2012; MacHarg 2001; Shumway 1999). ERDs reduce specific electricity consumption, which, when no recovery measure is implemented, is in the 4–6 kW$_e$/m^3 range (Semiat 2008).

ERD systems are mechanical devices and generally consist of turbines or pumps that recover the energy contained in the concentrated brine that leaves the membranes at a pressure between 1 and 4 bar below the pressure at the high-pressure pump outlet (see Fig. 1.13). The first design of an ERD appeared in the 1980s and was based on centrifugal pumps and Francis, or Pelton, hydraulic turbines. These systems resulted in specific electricity consumptions below 5 kWh/m^3 (Woodcock and Morgan White 1981). Nowadays, such recovery systems have been abandoned completely for work and pressure exchangers with isobaric, hyperbaric and even hydrodynamic chambers, in which the energy contained in the brine is directly transferred to the feedwater flow, which needs to be pressurised (see Fig. 1.16). As Fig. 1.16 shows, the main high-pressure pump is backed up by a booster pump, which reuses part of the energy of the discharged brine. The global efficiency of these systems is around 94 %, and the specific electrical consumption of RO systems with these devices can be as low as 2.5 kWh/m^3 (Peñate and García-Rodríguez 2011a).

Between 2005 and 2008, the global contracted capacity for RO technology increased from 2.0×10^6 to 3.5×10^6 m^3/day (Peñate and García-Rodríguez 2012). The largest RO plant in the world is in Sulaibiya (Kuwait) and has a capacity of 375,000 m^3/day (Pankratz 2010).

1.2.4 Comparison of Desalination Technologies

All of the previously shown desalination technologies are commercially available and can be coupled to power plants for combined freshwater and power production. However, the most favourable desalination process for this coupling needs to be selected after comparing all possibilities. Once the preselection is complete, detailed thermodynamic and economic analyses should be carried out at different sites, leading to selection of the most appropriate desalination technology for coupling to a concentrating solar power plant. Table 1.2 shows the main characteristics of the presented desalination processes.

Comparing the desalination processes driven by mechanical energy, it can be observed that the average electricity consumption for MED-MVC is twice that for RO, and the investment is also greater. Moreover, MED-MVC has a volume limitation of 3000 m³/day, making the system even more costly. Therefore, we have discarded this option as a desalination process to couple with a concentrating solar power plant. Despite RO having the greatest installed capacity to date, it has the disadvantage of requiring certain sophisticated pretreatments in order to prolong membrane life and prevent fouling, which is the main limiting factor for its application in certain parts of the world. Thermal desalination processes, however, need no pretreatments because they are very robust and require less maintenance. Furthermore, another advantage of thermal processes is the possibility of obtaining almost pure fresh water, with total dissolved solid (TDS) values below 10 mg/L. By contrast, for RO, the water product has TDS values of between 200 and 500 mg/L

Table 1.2 Techno-economic data of the most common desalination processes (Trieb 2007)

Energy used	Mechanical		Thermal	
Process	MED-MVC	RO	MSF	MED/TVC
State of the art	Commercial	Commercial	Commercial	Commercial
Global capacity installed in 2004 (Mm³/day)	0.6	6	13	2
Thermal consumption (kJ/kg)	–	–	250–350	145–390
Electricity consumption (kWh/m³)	8–15	2.5–7	3–5	1.5–2.5
Plant cost ($/m³/day)	1500–2000	900–1500	1500–2000	900–1700
Commissioning period (months)	12	18	24	18–24
Production capacity per unit (m³/day)	<3000	<20,000	<76,000	<36,000
Conversion factor	23–41 %	20–50 %	10–25 %	23–33 %
Top brine temperature (°C)	70	45 (maximum)	90–120	55–70
Reliability	High	Moderate	Very high	Very high
Maintenance (cleaning/year)	1–2	Frequent	0.5–1	1–2
Pretreatment	Very simple	Difficult	Simple	Simple
Operation requirements	Very simple	Difficult	Simple	Simple
Quality of water product (ppm)	<10	200–500	<10	<10

(Bruno et al.,2008). Nonetheless, in RO processes, higher conversion factors are achieved than in thermal desalination processes. In RO plants dealing with seawater (with TDS values above 25,000 mg/L), conversion factors of up to 50 % are usually achieved after the seawater has passed through a single membrane stage. Conversion factors of up to 85 % can be reached by passing the seawater through various modules placed in series (Verdier 2011). When using brackish waters (with TDS values between 1000 and 10,000 mg/L), conversion factors in the 60–90 % range are possible. In thermal desalination processes, conversion factors of only 10–33 % are obtained.

In order to select the most favourable desalination process, a comparison of the MED and MSF thermal desalination processes is given next. In both systems, to avoid scaling the TBT is limited by the salt concentration. The salt precipitates are usually calcium carbonate (frequently found in falling-film evaporators), magnesium hydroxide and calcium sulphate. Salt precipitate formation on the heat exchanger surfaces reduces the heat transfer rate, leading to a reduction in evaporator efficiency. Precipitation also provokes increased pressure loss in the tubes through which the salty water circulates, making periodic plant shutdowns necessary in order to remove it. Despite working at low TBTs, pretreatment is also necessary before introducing water into the distillation plant. In the case of MSF plants, the pretreatment carried out at the beginning of the operation consists of acidification, deaeration and neutralisation. In spite of this pretreatment, plant cleaning is required at least once a year because of salt precipitation on the evaporator surfaces; this is normally carried out using dilute sulphamic acid (Morin 1993). The water product obtained from the MSF process typically contains 2–10 ppm (mg/L) of dissolved solids (Khawaji et al. 2008), so remineralisation (post-treatment) is advisable in order to obtain water for human consumption.

In MED plants, the most commonly used pretreatment in use at the moment is a liquid solution based on polycarboxylic acid (Belgard EV2050, a well-known commercial product) (Patel and Finan 1999). This is particularly effective at preventing the formation of calcium carbonate precipitates and, moreover, has a great capacity to disperse suspended elements present in the brine. As in the case of MSF plants, MED plants also require cleaning at least once a year, for which dilute sulphamic acid is usually used. For MED processes, the product typically contains 2–5 ppm TDS (Ophir and Lokiec 2005). Therefore, as with MSF, remineralisation is required to produce drinking water.The GOR in MSF plants is directly related to the temperature difference between the TBT and the lowest temperature at which the seawater leaves the plant. In the MED process, the GOR is mainly influenced by the number of effects in the plant, a parameter that is directly related to the investment cost, because more stages require greater investment. On the other hand, the number of effects is limited by the temperature difference between the vapour generated in the first effect and the feedwater, as well as by the minimum temperature difference between the effects (Ophir and Lokiec 2005). The lower the temperature difference between effects, the higher the number of effects needed and, therefore, the higher the GOR. Typical temperature differences in MSF plants are between 2 and 5 °C (Khawaji et al. 2008) and GOR values are in the 8–12 range, depending on the feedwater steam temperature (Semiat 2008). This process requires

a considerable amount of thermal energy for the seawater evaporation process and substantial electricity to pump the large liquid flows (feedwater pumps, auxiliary pumps, brine and distillate pumps, pumps to recirculate the brine, as well as other auxiliary pumps for pretreatment product dosing). Typical thermal consumption in MSF plants is between 40 and 120 kWh/m^3. The specific electricity consumption in these plants is in the order of 2.5–5 kWh$_e$/m^3 (Semiat 2008). The conversion factors are between 10 and 25 %. In MED plants, the typical temperature difference between effects is in the 1.5–2.5 °C range (Ophir and Lokiec 2005). Current MED plants have GOR values ranging from 10 to 16 (Semiat 2008), which are greater than those obtained in an MSF plant. Therefore, MED plants require less investment cost than MSF plants because they need less heat transfer surface to achieve the same GOR. The GOR obtained in this type of plant corresponds to a thermal consumption of between 30 and 120 kWh/m^3 (Semiat 2008). Hence, the MED process is more efficient than the MSF process from the thermodynamic and heat transfer point of view. With regards to specific electricity consumption in MED plants, this is in the order of 2–5 kWh$_e$/m^3, mainly resulting from seawater pumping. This consumption is independent on the salinity of the seawater, the contamination or the temperature (Semiat 2008). The conversion factors for these plants range from 23 to 33 %, although conversion factors up to 50 % are also possible (Shemer 2011). In addition to the already-mentioned advantages of MED over MSF, the operating temperature of a MED plant is lower than that of an MSF plant, requiring lower-pressure steam when connected to the turbine outlet in a concentrating solar power plant, thus maximising its use for power production prior to being used in the desalination process. Therefore, in the present study, MSF technology has been discarded as an option for coupling to a concentrating solar power plant. The research work presented in this book is focused on combined freshwater and power production using MED and RO desalination technologies. Besides, the combination of both processes (MED and RO) can be attractive because it can reduce the cost of both desalination and power generation (Ludwig, 2004). These processes are characterised by flexibility during operation, low specific energy consumption, low capital cost, high plant availability and a higher electricity/water ratio than with MED technology. A study of this type of plant was carried out by Messineo and Marchese (2008).

References

Alarcón-Padilla, D., & García-Rodríguez, L. (2007). Application of absorption heat pumps to multi-effect distillation: A case study of solar desalination. *Desalination, 212*, 294–302.

Alarcón-Padilla, D., García-Rodríguez, L., & Blanco-Gálvez, J. (2007). Assessment of an absorption heat pump coupled to a multi-effect distillation unit within AQUASOL project. *Desalination, 212*, 303–310.

Alarcón-Padilla, D., Blanco-Gálvez, J., García-Rodríguez, L., Gernjak, W., & Malato-Rodríguez, S. (2008). First experimental results of a new hybrid solar/gas multi-effect distillation system: The AQUASOL project. *Desalination, 220*, 619–625.

Alarcón-Padilla, D., García-Rodríguez, L., & Blanco-Gálvez, J. (2010). Experimental assessment of connection of an absorption heat pump to a multi-effect distillation unit. *Desalination, 250*, 500–505.

Alawadhi, A. A. (2002, March 8–13). Regional report on desalination: Middle East and Africa. In: *Proceedings of the IDA World Congress on Desalination Water Reuse, Manama, Bahrain*. Topsfield, MA: IDA

Amer, A. O. B. (2009). Development and optimization of ME-TVC desalination system. *Desalination, 249*, 1315–1331.

Baig, H., Antar, M. A., & Zubair, S. M. (2011). Performance evaluation of a once-through multi-stage flash distillation system: Impact of brine heater fouling. *Energy Conversion and Management, 52*, 1414–1425.

Blanco, J., Alarcón, D., Guillén, E., & Gernjak, W. (2011). The AQUASOL system: Solar collector field efficiency and solar-only mode performance. *Journal of Solar Energy Engineering, 133*, 011009–1.

Bonnélye, V., Guey, L., & Del Castillo, J. (2008). UF/MF as RO pre-treatment: The real benefit. *Desalination, 222*, 59–65.

Brehant, A., Bonnelye, V., & Pérez, M. (2002). Comparison of MF/UF pretreatment with conventional filtration prior to RO membranes for surface seawater desalination. *Desalination, 144*, 353–360.

Breidenbach, L., Rautenbach, R., Tusel, G. F. (1997, October 6–9). Thermo-economic assessment of fossil fuel fired dual purpose power/water plants. In: *Proceedings of the IDA World Congress on Desalination And Water Reuse, Madrid, Spain* (pp. 167–180). Topsfield, MA: IDA

Buros, O. K., Cox, R. B., Nusbaum, I., El-Nashar, A. M., & Bakish, R. (1980). *The U.S.A.I.D. desalination manual*. Teaneck, NJ: International Desalination and Environmental Association.

Buros, O. K. (2000). *The ABCs of desalting* (2nd ed.). Topsfield, MA: International Desalination Association.

Childs, W., & Dabiri, A. (1999). Hydraulic driven RO pump & energy recovery system. *Desalination & Water Reuse, 9*(2), 21–29.

Chua, K. T., Hawlade, M. N. A., & Malek, A. (2003). Pretreatment of seawater: Results of pilot trials in Singapore. *Desalination, 159*, 225–243.

Darwish, M. A., Al-Juwayhel, F., & Abdulraheim, H. K. (2006). Multi-effect boiling systems from an energy viewpoint. *Desalination, 194*, 22–39.

US DoE. (2006). *Energy demands on water resources: Report to Congress on the independency of energy and water*. Washington, DC: U.S. Department of Energy.

Duranceau, S. J., Foster, J., Losch, H. J., Weis, R. E., Harn, J. A., & Nemeth, J. (1999). Interstage turbine. *Desalination & Water Reuse, 8*(4), 34–40.

Ebrahim, S., Abdel-Jawad, M., Bou-Hamad, S., & Safar, M. (2001). Fifteen years of R&D program in seawater desalination at KISR. Part I Pretreatment technologies for RO systems. *Desalination, 135*, 141–153.

El-Nashar, A. M. (2000). Predicting part load performance of small MED evaporators—A simple simulation program and its experimental verification. *Desalination, 130*, 217–234.

Sidem Entropie (2008). *Multi-effect distillation—Processes for seawater desalination*. Retrieved from http://www.entropie.com/en/services/desalination/brochurequestionnaire/

Gregorzewski, A., Genthner, K., Zarza, E., Leon, J., de Gunzbourg, J., Alefeld, G., & Scharfe, J. (1991). The solar thermal desalination research project at the Plataforma Solar de Almería. *Desalination, 82*, 145–152.

Gruendisch, A. (1999). Re-engineering of the Pelton turbine for SW & brackish water energy recovery. *Desalination & Water Reuse, 9*(3), 16–23.

Huang, Q., & Ma, W. (2012). A model of estimating scaling potential in reverse osmosis and nanofiltration systems. *Desalination, 288*, 40–46.

Jeong, B., Hoek, E. M. V., Yan, Y., Subramani, A., Huang, X., Hurwitz, G., Ghosh, A. M., & Jawor, A. (2007). Interfacial polymerization of thin film nanocomposites: A new concept for reverse osmosis membranes. *Journal of Membrane Science, 294*, 1–7.

Khawaji, A. D., Kutubkhanah, I. K., & Wie, J-M. (2008). Advances in seawater desalination technologies. *Desalination, 221*, 47–69.

Kumano, A., Sekino, M., Matsui, Y., Fujiwara, N., & Matsuyama, H. (2008). Study of mass transfer characteristics for a hollow fiber reverse osmosis module. *Journal of Membrane Science, 324*, 136–141.

Kumar, M., Grzelakowski, M., Zilles, J., Clark, M., & Meier, W. (2007). Highly permeable polymeric membranes based on the incorporation of the functional water channel protein Aquaporin Z. *Proceedings of the National Academy of Sciences of the United States of America, 104*, 20719–20724.

Legorreta, C., Hinge, S., Tonner, J., & Lovato, A. (1999). Plates—The next breakthrough in desalination. *Desalination, 122*, 235–246.

Leidner, A. J., Rister, M. E., Lacewell, R. D., Woodard, J. D., & Sturdivant, A. W. (2012). An analysis of input choice, input prices, and environmental factors on the costs of seawater reverse osmosis systems. *Desalination, 291*, 48–55.

MacHarg, J. P. (2001). Exchanger tests verify 2.0 kWh/m^3 SWRO energy use. *Desalination & Water Reuse, 11*(1), 42–45.

Madaeni, S. S., & Samieirad, S. (2010). Chemical cleaning of reverse osmosis membrane fouled by wastewater. *Desalination, 257*, 80–86.

Malaeb, L., & Ayoub, G. M. (2011). Reverse osmosis technology for water treatment: State of the art review. *Desalination, 267*, 1–8.

Manahan, S. E. (1997). *Environmental science and technology*. Boca Raton, FL: CRC Press.

Messineo, A., & Marchese, F. (2008). Performance evaluation of hybrid RO/MEE system powered by a WTE plant. *Desalination, 229*, 93.

Morin, O. J. (1993). Design and operating comparison of MSF and MED systems. *Desalination, 93*, 69–109.

Morsy, H., Larger, D., & Genthner, K. (1994). A new multiple-effect distiller system with compact heat exchangers. *Desalination, 96*, 59–70.

Nafey, A. S., Fath, H. E. S., & Mabrouk, A. A. (2006). Thermo-economic investigation of multi effect evaporation (MEE) and hybrid multi effect evaporation—multi stage flash (MEE-MSF) systems. *Desalination, 201*, 241–254.

Noble, R. D., & Stern, S. A. (Eds.). (2003). *Membrane and separations technology principles and applications* (pp. 29–75). Amsterdan, The Netherlands: Elsevier.

OECD. (2008). *OECD environmental outlook to 2030*. Paris: Organisation for Economic Co-operation and Development.

Ophir, A., & Gendel, A. (2000). Development of the world's largest multi-effect mechanical vapor compression desalination plants. *Desalination & Water Reuse, 9*(4), 54.

Ophir, A., & Lokiec, F. (2005). Advanced MED process for most economical sea water desalination. *Desalination, 182*, 187–198.

Pankratz, T. (2009a). Marafiq makes first water. *Water Desalination Report by Media Analytics and Global Water Intelligence 45* (31). Houston, TX.

Pankratz, T. (2009b). Market growing at record rate. *Water Desalination Report by Media Analytics and Global Water Intelligence 45* (41). Houston, TX.

Pankratz, T. (2010). *IDA desalination yearbook 2010–2011*. Topsfield, MA: IDA.

Pankratz, T. (2014). *IDA desalination yearbook 2014–2015*. Topsfield, MA: IDA.

Patel, S., & Finan, M. A. (1999). New antifoulants for deposit control in MSF and MED plants. *Desalination, 124*, 63–74.

Peñate, B., & García-Rodríguez, L. (2011). Energy optimisation of existing SWRO (seawater reverse osmosis) plants with ERT (energy recovery turbines): Technical and thermoeconomic assessment. *Energy, 36*, 613–626.

Peñate, B., & García-Rodríguez, L. (2012). Current trends and future prospects in the design of seawater reverse osmosis desalination technology. *Desalination, 284*, 1–8.

Semiat, R. (2008). Energy issues in desalination processes. *Environmental Science and Technology, 42*, 193–201.

Shemer, H. (2011). Execution of a Chinese desalination project at minus 20°C. *Desalination & Water Reuse, 21*, 18–22.

Shumway, S. A. (1999). The work exchanger for SWRO energy recovery. *Desalination & Water Reuse, 8*(4), 27–33.

Smuleac, V., Butterfield, D. A., & Bhattacharyya, D. (2004). Permeability and separation characteristics of polypeptide-functionalized polycarbonate track-etched membranes. *Chemistry of Materials, 16*, 2762–2771.

Soteris, K. (1997). Survey of solar desalination systems and system selection. *Energy, 22*, 69–81.

Soteris, K. (2005). Seawater desalination using renewable energy sources. *Progress in Energy and Combustion Science, 31*, 242–281.

Torzewski, A., & Müller, J. (2009). Should we build any more MSF plants? *Desalination & Water Reuse, 19*(4), 16–21.

Trieb, F. (2007). *Concentrating solar power for seawater desalination. Aqua-CSP study report*. Stuttgart, Germany: DLR (German Aerospace Center).

Valero, A., Uche, J., Serra, L.(2001) *La desalación como alternativa al plan hidrológico nacional*. Zaragoza: CIRCE/University of Zaragoza. Retrieved June 25, 2015, from http://www.uv.es/choliz/Desalacion.pdf

Vial, D., & Doussau, G. (2003). The use of microfiltration membranes for seawater pre-treatment prior to reverse osmosis membranes. *Desalination, 153*, 141–147.

Wangnick, K. (2000). Present status of thermal seawater desalination techniques. *Desalination Water Reuse Quarterly, 10*(1), 14.

Wiesner, M. R., & Chellam, S. (1999). The promise of membrane technologies. *Environmental Science and Technology, 33*, 360–366.

Woodcock, D. J., & Morgan White, I. (1981). The application of pelton type impulse turbines for energy recovery on sea water reverse osmosis systems. *Desalination, 39*, 447–458.

Zarza, E. (1994). *Solar thermal desalination project: Phase II results & final project report*. Madrid, Spain: Secretaría General Técnica del CIEMAT, PSA/CIEMAT.

Chapter 2
Combined Fresh Water and Power Production: State of the Art

Nomenclature

Acronyms

PT	Parabolic-trough
CSP + D	Concentrating solar power and desalination
PSA	Plataforma Solar de Almería
RO	Reverse osmosis
MED	Multi-effect distillation
MSF	Multi-stage flash
MED-TVC	Multi-effect distillation with thermal vapour compression
SEG	Solar electric generating station

Variables

DNI	Direct normal irradiance (W/m^2)
LEC	Levelised electricity cost ($/MWh)

2.1 Introduction

This chapter deals with the combined fresh water and power production by concentrating solar power (CSP) and desalination plants (CSP + D). First, the cogeneration of electricity and desalinated water from conventional power plants is described to provide a better understanding of the integration processes. Later in the chapter, the CSP plant technologies available are described, focusing particularly on parabolic-trough collectors. Finally, the latest studies related to CSP + D plants and the existing refrigeration systems within CSP plants are expounded.

2.2 Combined Fresh Water and Power Production from Conventional Power Plants

Generally, an increase in demand for fresh water goes hand in hand with an increase in demand for power. Given that both require a primary energy source, a compelling and efficient option is the cogeneration plant concept for simultaneous fresh water and power production; these are also called dual-purpose plants.

Figure 2.1 shows the basic layout of a cogeneration plant. Cogeneration is defined as the procedure by which both electricity and useful thermal energy (heat) are obtained simultaneously from the same fuel. There are two alternatives for simultaneously generating fresh water and electricity, depending on the form of energy required in the desalination process. In the case of a thermal desalination process (e.g. multi-effect distillation [MED]), the steam at the turbine outlet (exhaust steam) is used as the energy supply for the desalination process. When the desalination process is driven by mechanical energy (e.g. reverse osmosis [RO]), the electricity needed for the high-pressure pump comes from the power plant. As can be observed, this latter case is not strictly a cogeneration process.

This section reviews the power cycles used at the industrial level as well as the state of the art in the fresh water and power cogeneration field.

2.2.1 Power Cycles

Power is produced through thermodynamic cycles; these can be steam or gas, depending on the phase of the working fluid used in the cycle. In gas cycles, the working fluid remains in the gas phase throughout the whole cycle, whereas in steam cycles the working fluid stays in the steam phase for part of the cycle and in the liquid phase for the rest. Four types of power cycle are normally used in power plants: the Rankine cycle, the Brayton cycle, the Otto cycle and the Diesel cycle. The Rankine cycle is used in steam cycles, whereas the rest are applied in gas cycles. The Brayton cycle is generally used in industrial applications, whereas the other two (Otto and Diesel) are applied in small-scale power production. The Brayton cycle can be classified as either an open or closed cycle. In closed cycles, the working fluid (air) returns to its initial state at the end of the cycle and is then recirculated. In open cycles, the working fluid is refreshed at the end of each cycle instead of being recirculated. In Fig. 2.2, an ideal closed Brayton cycle is shown together with the corresponding temperature–entropy diagram $(T-s)$ showing the processes taking place in the cycle.

The thermal efficiency of the cycle is defined as the ratio between the net work produced and the total heat delivered. In an ideal Brayton cycle, this efficiency depends on the ratio between the pressure inside and outside the combustion chamber, which is 40–45 % in an ideal cycle (Cengel and Boles 2007). However,
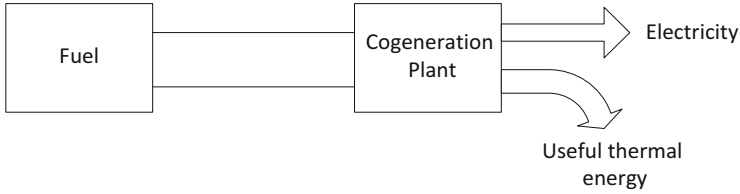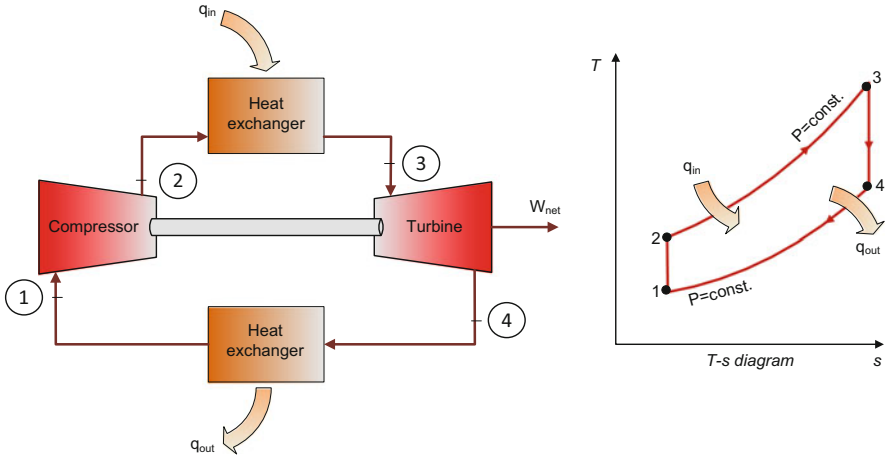
Fig. 2.1 A cogeneration system

Fig. 2.2 An ideal closed Brayton cycle

in practice, as a result of irreversibilities, efficiencies of approximately 30 % are obtained for a simple cycle. The simple cycle can be modified to achieve higher efficiencies, as in the case of the Brayton cycle with regeneration, where the air leaving the compressor is heated using a heat exchanger by the gases at the turbine outlet (this being an open cycle). Such cycles can achieve efficiencies of up to 37 %. Furthermore, Brayton cycle efficiency can be increased still further (up to 55 %) using intercooling, reheating and regeneration. Figure 2.3 shows the schema of an ideal simple Rankine cycle and its corresponding $T-s$ diagram, in which the different processes in the cycle are indicated. The efficiency of an ideal Rankine cycle is around 43 % (Cengel and Boles 2007). As with the Brayton cycle, however, the real efficiency of this type of cycle is usually around 36 % as a result of irreversibilities. Power plants with steam cycles are responsible for a large part of the world's electricity production; thus an increase in cycle efficiency could lead to great savings in fuel consumption. As with gas cycles, an increase in thermal efficiency can be achieved by modifying the steam cycles. All of the cycle modifications are based on an increase in the average temperature at which heat is transferred to the working fluid in the boiler, or a decrease in the
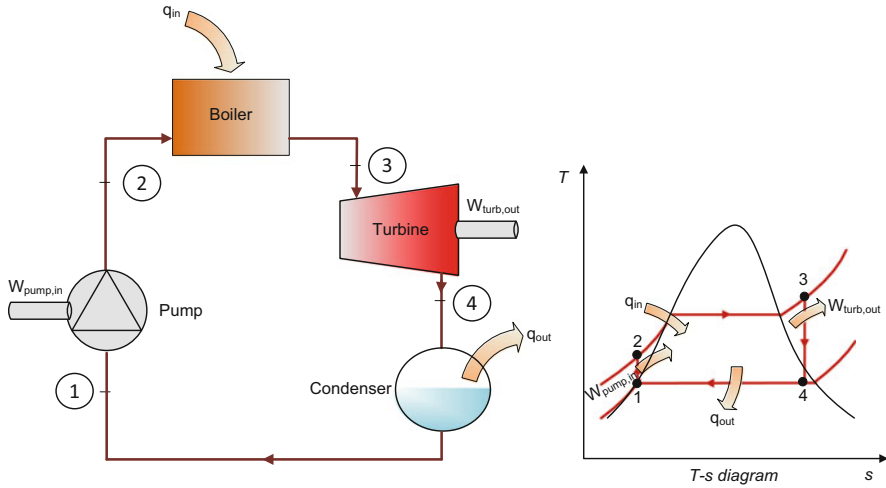
Fig. 2.3 An ideal simple Rankine cycle

average temperature at which heat is rejected from the working fluid in the condenser.

Modifying the steam cycle by adding a reheating process improves cycle efficiency and also offers a practical solution to deal with the steam's excessive moisture content at the turbine outlet, which decreases the turbine efficiency and erodes the turbine blades. A Rankine cycle with reheating differs from the simple cycle in that the isentropic expansion process takes place in two stages (see Fig. 2.4). In the first stage (the high-pressure turbine), steam is expanded isentropically to an intermediate pressure and sent back to the boiler, where it is reheated at a constant pressure, usually to the inlet temperature of the first turbine stage. The steam then expands isentropically in the second stage (the low-pressure turbine) to the condenser pressure. The reheating process improves the cycle efficiency by 4–5 % (Cengel and Boles 2007).

Another alternative for increasing Rankine cycle efficiency is to increase the temperature of the liquid (called feedwater) at the pump outlet before it enters the boiler. This is achieved by a regeneration process that consists of steam extraction from the turbine to heat the feedwater. The device where this is carried out is called the feedwater heater (FWH). There are two types, open or closed. Open FWHs are basically mixers; the steam extracted from the turbine is mixed with the feedwater leaving the pump (see Fig. 2.5). In closed FWHs, heat is transferred from the steam extracted from the turbine to the feedwater without any mixing. The thermal efficiency of these cycles increases linearly with increasing number of FWHs used. However, there is an economic limit to the number of heaters. Efficiencies in the 38–40 % range can be achieved with these types of cycles (Cengel and Boles 2007).
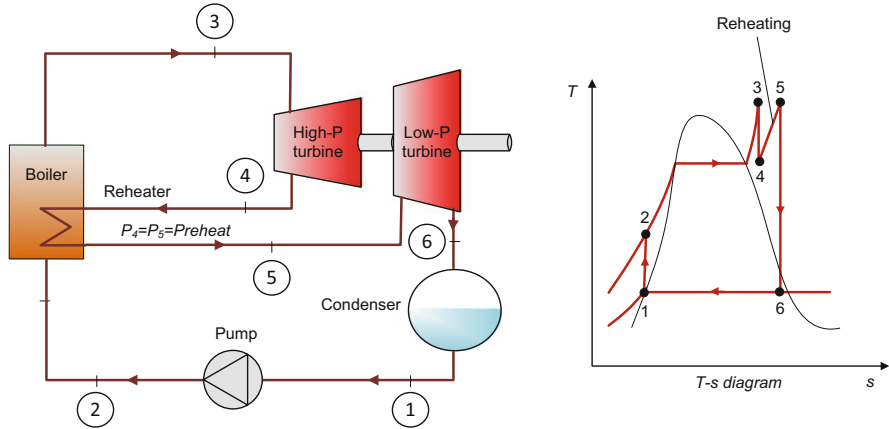
Fig. 2.4 An ideal Rankine cycle with reheating
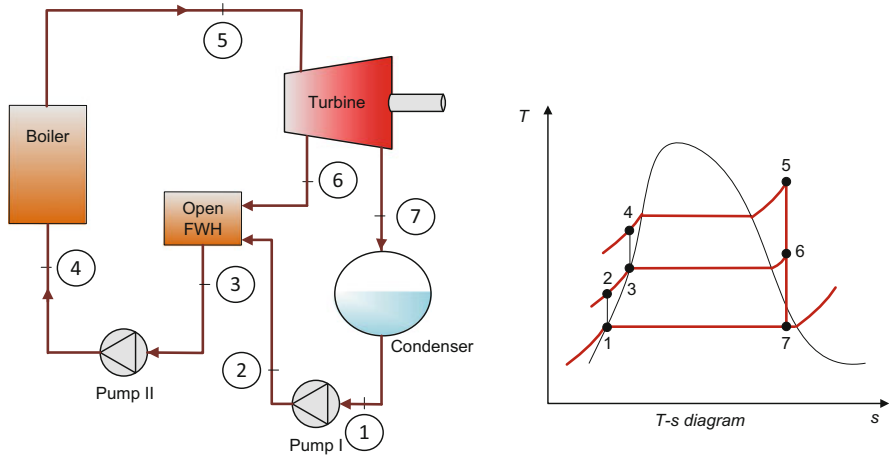
Fig. 2.5 An ideal Rankine cycle with regeneration

The steam turbines used in Rankine cycles are classified (based on the exhaust steam pressure) into condensing turbines and back-pressure (or non-condensing) turbines. Both types can include steam extraction or steam bleeding in the intermediate stages, from which the necessary steam for process heat is obtained. Back-pressure turbines are more widely used in steam generation applications (cogeneration) and generate electricity by expanding the high-pressure steam to the required pressure, using regulating valves to achieve the necessary conditions. Condensing turbines operate in a similar way as the back-pressure turbines, but the steam expands to a pressure lower than atmospheric pressure, directing the steam straight to the plant condenser. These turbines are generally used in power plants whose only purpose is electricity generation. Furthermore, in these turbines, part of the
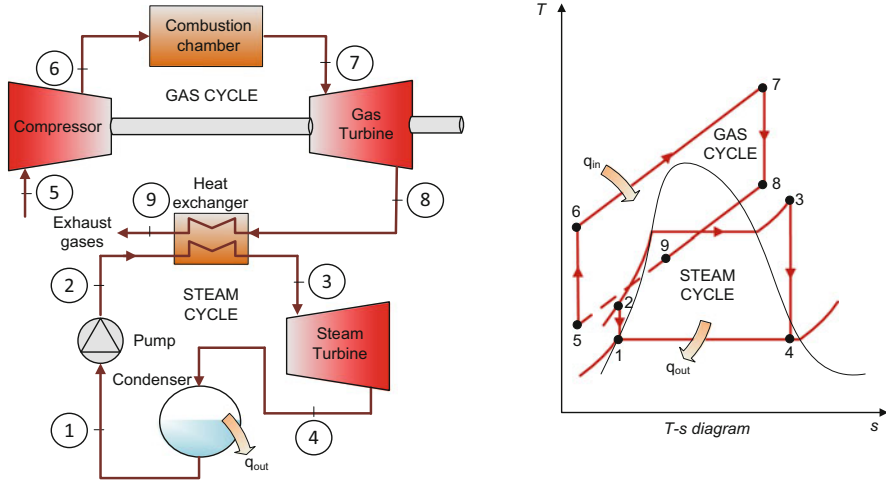
Fig. 2.6 A combined gas–steam cycle

steam can be extracted, or bled, at one or various points around the turbine before reaching the outlet to the condenser; thus they can be used in specific industrial processes. Brayton cycles normally operate at considerably higher temperatures than Rankine cycles. The maximum working fluid temperature at the turbine inlet is approximately 620 °C for current power plants with steam turbines, compared to more than 1425 °C for gas turbine power plants (Cengel and Boles 2007). Because of these high temperatures, gas cycles have a greater potential for achieving higher thermal efficiencies. However, the disadvantage is that the gas leaves the turbine at a very high temperature (normally above 500 °C), which reduce the potential for achieving higher efficiencies. Such efficiencies can be increased by combining gas and steam cycles. Figure 2.6 shows a schema of this cycle, with its corresponding $T-s$ diagram. Here, the energy contained in the gases at the gas cycle outlet is recovered by transferring it to the steam in the steam cycle using an energy-recovery heat exchanger (also called a heat recovery steam generator). These combined cycles are a very attractive option because power plant efficiency is increased with hardly any increase in investment cost. Thermal efficiencies above 40–50 % can be obtained with these types of cycles (Cengel and Boles 2007).

2.2.2 Simultaneous Fresh Water and Power Production

The scientific literature is replete with works concerning the combined production of fresh water and electricity, a research line that began more than four decades ago (Clelland and Stewart 1966).

Among the first publications are important works published by Hornburg and Cruver (1977) and El-Nashar and El-Baghdady (1984). In these studies, gas and

steam turbine power plants were considered for power generation, along with multi-stage flash (MSF) and RO desalination processes for fresh water production. Since then, a significant number of studies have been published in this field. Some authors have described and compared the alternatives of such a coupling. El-Nashar (2001) presented different options for combining power plants with desalination plants. Four of these options consisted of combining gas turbine power plants with MSF desalination plants, and another two combined steam turbine power plants (back-pressure or condensing turbines) with the same desalination process. Kronenberg (1996) and Kronenberg and Lokiec (2001) evaluated cogeneration systems with two low-temperature heat sources (waste heat from a diesel power plant and steam coming from an existing power plant) feeding a low temperature MED (LT-MED) plant. Kamal (2005) evaluated the benefits of integrating RO desalination plants with existing dual-purpose plants in the Middle East. The dual-purpose plants considered were comprised of a conventional coal-fired power plant coupled to an MSF plant. Darwish and Al Najem (2004) presented the coupling of RO, MSF and MED-thermal vapour compression (MED-TVC) with a combined cycle. In order to reduce the cost of products and the environmental impact, Hosseini et al (2012) dealt with a multi-objective optimisation for designing a combined-cycle power plant and an MSF dual-purpose plant. As in the previous works, the use of only one desalination technology was considered.

The combination of a power plant with two or more different desalination technologies (hybrid systems) is another option of special interest. Hamed (2005) presented a general perspective for the combination of a hybrid MSF/RO system with power plants. Almulla et al. (2005) carried out the evaluation of a triple hybrid system that included the integration of three desalination processes (MSF, MED and RO) into a power plant. The use of other energy sources has also been investigated for the cogeneration of fresh water and electricity. Various works have been published in which the integration of MED, MSF, TVC, RO and hybrid desalination processes into nuclear power plants were studied (Darwish et al. 2009a, b; Al-Mutaz 2003; Manesh and Amidpour 2009; Ansari et al. 2010; Adak and Tewari 2014).

Choosing the optimal configuration for fresh water and power production depends on various factors such as the required power-to-water ratio, the cost of fuel energy used in the desalination process, electricity sales, capital costs and local requirements. Some authors have addressed economic analyses to evaluate the weight of each of the cited factors. Hamed et al. (2006) analysed the impact of variations in the fossil fuel prices, the amount of the fuel used and the local requirements for a cogeneration plant consisting of an MSF plant integrated into a steam turbine power plant. Kamal (2005) analysed the water costs for different cogeneration schemes integrating a steam-turbine power plant with various desalination technologies (LT-MED, MSF and RO). Rensonnet et al. (2007) analysed the electricity costs for different combinations of a gas turbine power plant with MED, RO and a hybrid RO/MED system. Yang and Shen (2007) carried out an economic analysis to determine the energy cost for fresh water production from cogeneration plants, which consisted of integrating MED-TVC plants into steam-turbine power plants. On the other hand, Uche et al. (2001) published a thermo-economic

optimisation of a cogeneration plant consisting of an MSF desalination plant integrated into a steam-turbine power plant. This optimisation was based on local optimisation of the different system units. Mahbub et al. (2009) made a detailed thermo-economic analysis of different cogeneration plants composed of a combined-cycle plant with MSF, MED, RO, MSF/RO and MED/RO systems. Shakib et al. (2012) presented an optimisation study from a thermo-economic analysis of a MED-TVC plant coupled to a gas-turbine power plant. Hosseini et al. (2011, 2012) presented works based on the thermo-economic analysis of a gas-turbine plant combined with an MSF plant.

Other authors have focused their research on the thermodynamic analysis of cogeneration plants. Madani (1996) presented an analysis of a cogeneration plant consisting of a desalination plant comprising direct contact multi-stage evaporators integrated into a regenerative-cycle power plant with reheating, using seawater as the working fluid and superheated steam as the heat transfer media. Wang and Lior (2007) carried out a study of the energy, exergy and efficiency of integrated systems that used gas turbines with steam injection to produce electricity and a MED-TVC desalination plant to produce fresh water.

Bouzayani et al. (2009) analysed the efficiency of three systems that combined an RO plant, which had an energy recovery system, and a steam-cycle power plant. In one case, the energy recovery system was a pressure exchanger, and in the other two, this recovery was carried out using a hydraulic turbine. The coupling of an RO plant to a power plant was only mechanical in one case (the power plant providing the necessary mechanical energy to the RO plant pumps) and thermal and mechanical in the other two cases (part of the discharged heat from the power plant condenser was transferred to the seawater). Luo et al. (2011) also analysed the efficiency of a cogeneration plant. In this case, an innovative system that combined a gas turbine power plant with a chemical recovery process and a MED-TVC desalination plant was studied.

2.3 Concentrating Solar Power Plants

According to the last report from the International Energy Agency (OECD/IEA 2014), the global energy demand is set to grow by 37 % by 2040, but the development path for a growing world population and economy is less energy-intensive than it used to be. Furthermore, climate change, which is caused in part by greenhouse gas emissions from the burning of fossil fuels, along with a slight increase in their use, makes it almost mandatory to use renewable energies to both satisfy energy demand and achieve a sustainable future energy supply. In particular, solar energy is predicted to figure strongly because it is the energy source with the greatest potential of all the renewable sources (Webber 2008).

This is the reason why electricity generation using concentrating solar power (CSP) plants will play an important role in the future (Zachary and Layman 2009).

Some scenarios predict participation from thermal solar energy of about 11 % of global electricity generation by 2050 (OECD/IEA 2014). The current projects under construction estimate a power of 980 MW$_e$, and projects for a total of 7500 MW$_e$ have already been announced. A prominent project is the well-known Desertec Industrial Initiative (Desertec Foundation 2010), which began in 2009. The aim is to provide electricity to southern Europe as well as to the Middle East and North Africa (these last two are grouped under the acronym MENA, Middle East and North Africa) using the installation of CSP plants in desert regions.

   All the technologies used in the generation of electricity using CSP plants are based on concentrating solar radiation to obtain thermal energy at high temperature, which is then used to generate electricity via conventional power cycles using steam or gas turbines (or Stirling engines). To concentrate the solar energy, most systems use glass mirrors with up to 95 % reflectivity, which constantly follow the path of the sun using the direct normal irradiance (DNI). These technologies demonstrate optimal integration in hybrid systems, combining with fossil fuels or other sources of renewable energies. The advantage of CSP plants compared with other systems that also use renewable energies (such as solar photovoltaic and wind power) is that they can mostly replace the use of fossil fuel by oversizing the solar collector field used to concentrate the solar radiation and storing part of the generated energy in a thermal storage system. There are two types of concentrators: those that concentrate the solar radiation at a focal point (central receiver and parabolic dish systems) and those that concentrate the solar radiation onto a line (parabolic-trough and linear Fresnel). Figure 2.7 shows the CSP technologies mentioned, which are described in more detail below.

2.3.1   Parabolic-Trough Collectors

Parabolic-trough collectors consist of long U-shaped mirrors with a linear axis tracking system. The mirrors reflect direct solar radiation along their focal line, where an absorber tube is located. The receiver/absorber tube is made of steel and has a selective coating that maintains high absorbance in the solar spectrum wavelength range, but high reflectance in the infrared spectrum (i.e. it emits as little as possible). In order to prevent heat loss to the ambient air, the absorber tube is enveloped by an evacuated glass tube. A heat transfer fluid flows into the absorber tube and absorbs the radiation that has been concentrated 30–100 times. The most commonly used fluid is thermal oil, although the use of water/steam or molten salt is also being researched (Fernández-García et al. 2010). In a CSP plant with parabolic-trough technology (PT-CSP), once the fluid has absorbed the radiation, it is used to generate steam in a heat exchanger at around 390 °C, which is then sent to a conventional Rankine cycle to produce electricity. A hybrid operation is also possible using all types of fossil fuels and renewables (Trieb et al. 2009).
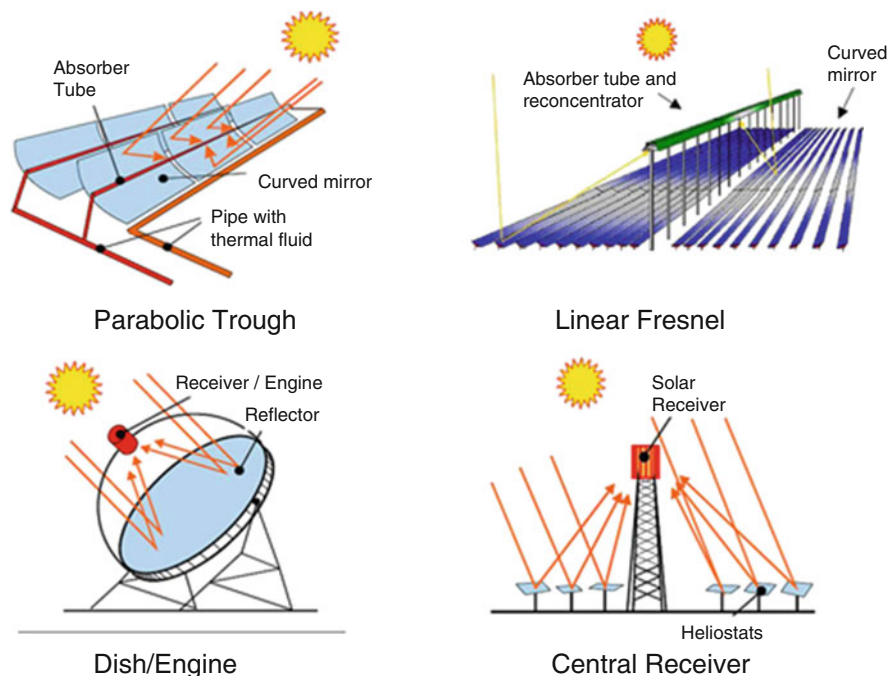
Fig. 2.7 Concentrating solar power technologies

Because of the variable nature of solar radiation, it is necessary to design the collector field to generate more energy than the turbine can accept under normal conditions. This excess of energy is used to charge the storage system, which provides the required energy to the turbine during periods when there is insufficient solar radiation (Tamme et al. 2004). The storage systems in the first PT-CSP plants were based on two storage tanks, in which the heat transfer fluid also served as the storage medium. This concept was demonstrated successfully in the first of the solar electric generating systems (SEGS) plants (Winter et al. 1990). However, the heat transfer fluid used in these PT-CSP plants was very expensive, greatly increasing the total cost of scaling up the storage capacity. For this reason, a study was carried out to evaluate the concept of molten salts as the thermal storage medium in PT-CSP plants, using data from the solar tower plant "Solar Two". The study concluded that, given its characteristics and cost, this type of storage could also be used in PT-CSP plants, with indirect storage in two molten salt tanks. It is an efficient, low-cost storage medium and, moreover, the molten salts are neither flammable nor toxic (Sandia National Laboratories 2008). This is the system currently used in commercial plants, such as ANDASOL, the first commercial plant with such technology in Spain (Solar Millennium 2009). The basic system consists of circulating the oil through the collector solar field, then transferring its thermal energy through a heat exchanger to the thermal storage medium, in this case molten salts (see Fig. 2.8).
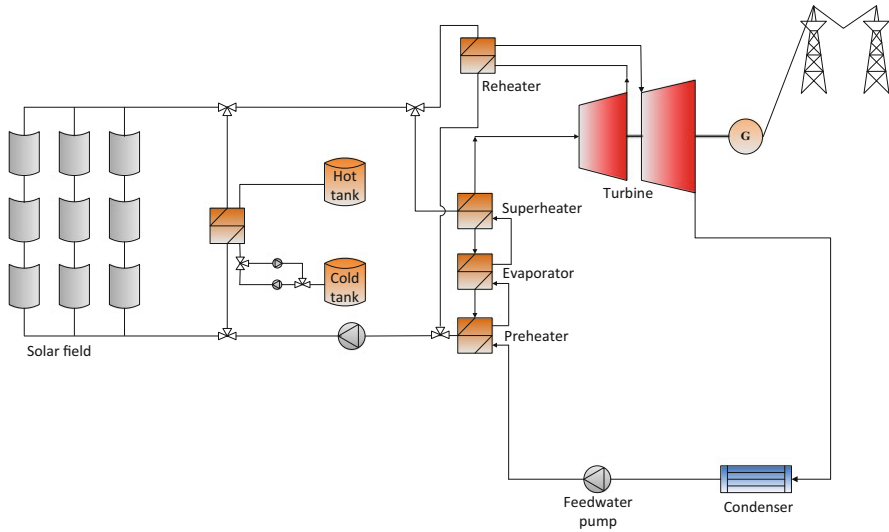
Fig. 2.8 Parabolic-trough collector field coupled to a steam cycle

One of the tanks is used to store the hot molten salts (the hot tank) and the other to receive the cold molten salts (the cold tank). During the thermal storage charging cycle, part of the oil coming from the solar collector field is sent to the oil–salt heat exchanger. In this way, thermal energy is transferred from the oil to the salt stored in the hot tank. During the discharge cycle, the salt and oil pathways in the oil–salt heat exchanger are inverted and, therefore, the thermal energy is transferred from the salt to the oil on its way to the cold tank.

Direct steam generation in parabolic-trough absorber tubes is seen as a promising option for increasing the economic efficiency of CSP plants (Eck and Steinmann 2005) as they can reach higher temperatures and thus achieve greater efficiencies (Trieb et al. 2009). Furthermore, the environmental risks from oil are avoided, as well as the heat exchanger between the collector field and the power cycle unnecessary. Within an European project framework carried out at the Plataforma Solar de Almería (PSA), the operation and control of this new technology has been successfully proven under transitory and steady-state conditions. For this purpose, a loop 700 m length was constructed with a 5.70-m parabolic-trough aperture, in which steam temperatures of up to 400 °C and pressures of 100 bar have been achieved. The long-term objective is to heat steam to a temperature of 550 °C and 120 bar and to develop a thermal storage system that matches this technology, based on phase-change storage (Eck 2009).

Parabolic-trough systems dominate the global market in CSP plants. The first to be installed using this technology were the SEGS plants in the Mojave Desert in California (Pharabod and Philibert 1991). This was at the beginning of the 1980s when plants with more than a 350 MW$_e$ capacity were put into operation. By the middle of 2009, 95 % of the 560 MW$_e$ produced by CSP plants in the world

corresponded to plants whose technology was based on parabolic-trough collectors. Currently, parabolic-trough technology for the CSP plants is the one most widely installed in the world (90 % of the total). These systems achieve solar–electric conversion efficiencies of between 10 and 15 %, but have the potential of reaching 18 % in the medium-term (Trieb 2007). Solar–electric efficiency includes the conversion of solar energy to thermal energy by means of a solar collector field and the conversion of thermal energy to electricity using a power block. A maximum solar–electric efficiency of 21.5 % was measured in a 30 MW$_e$ plant in California (Trieb 2007).

2.3.2 Linear Fresnel

In linear Fresnel systems, as with parabolic-trough collector systems, solar radiation is concentrated onto a line and can be coupled to steam cycles for electricity generation. These systems have been developed with the aim of attaining a simpler design and at less cost than the parabolic-trough systems. The first prototypes have shown promise and the first CSP plants that include this technology are currently in the construction phase.

The collectors in a linear Fresnel system are made up of a large number of mirror segments that can individually follow the path of the sun (see Fig. 2.7). Unlike parabolic-trough collectors, the absorber tubes in the Fresnel systems are in a fixed position above the mirrors in the centre of the solar field and, therefore, do not move together with the mirrors as they follow the sun. The system can operate with oil, water or molten salts. Current designs use water directly in the receiver tubes at 50 bar pressure and 280 °C, or alternatively molten salts (US DoE 2009). The storage methods applicable for these systems are similar to those used for parabolic-trough collector systems.

The steam cycle efficiency of linear Fresnel systems is less than that of parabolic-trough collector systems because the steam temperature is lower. However, the Fresnel systems have certain advantages over parabolic-trough systems. The Fresnel collectors have a lighter structure; those designed by Novatec-Biosol are 80 % lighter per square metre (Trieb 2007). Consequently, such systems require less investment and have lower operation and maintenance costs than parabolic-trough collectors. Regarding the disadvantages, the simple optical design of the Fresnel system means that the optical efficiency of a field formed by these mirrors is less; therefore, approximately 33 % more aperture area is necessary for the same thermal energy production compared with parabolic-trough collectors (Trieb 2007). In terms of integrating the solar field into the environment, the Fresnel system has considerable advantages over parabolic-trough collectors. The land use is far better because less distance is required between mirrors. The aperture area of the collectors covers between 80 and 95 % of the land required, compared with only 30 % covered by parabolic-trough mirrors as a result of the considerable distance needed between the collector rows to avoid shadowing. Therefore, the land-use efficiency of linear Fresnel collectors is approximately three times greater than for parabolic-

trough collectors (Trieb 2007). Taking into account that the Fresnel system has less optical efficiency (about 67 % of that for a parabolic trough), the production per square metre of land from this type of solar field is twice that of a parabolic-trough field. This fact might be of little importance in isolated desert areas where land use is not limited, but could be of relevance when it is integrated into a CSP plant in industrial or tourist complexes, or near urban centres. However, this technology is not as mature as parabolic-trough technology and it remains in the demonstration phase. Two plants are currently in operation, with a total capacity of 6.4 MW$_e$.

2.3.3 Central Receiver Systems (Solar Tower)

Central receiver (or solar tower) systems use a large field of mirrors with solar tracking on two axes (called heliostats) that reflect the sunlight onto a central receiver located at the top of a tower. In the receiver, the concentrated solar energy is absorbed by the working fluid that circulates around it, converting the solar energy into thermal energy. Typical concentration factors fluctuate between 200 and 1000 (Trieb et al. 2009). The working fluid can be water or steam, molten salts, liquid sodium or air. The concentration factors achieved are so high in these systems that temperatures of 1200 °C can be reached (Alexopoulos and Hoffschmidt 2010), which enables them to be integrated into steam, gas or combined cycles (Price and Kearney 1999; Buck et al. 2000; de Lalaing 2001). Moreover, these systems can be integrated into fossil fuel plants for hybrid operation, offering a great variety of options. Commercial solar towers also use molten salts as the thermal storage medium, allowing the system to extend its operating hours or increase capacity during periods when the electricity flowing into the network is at a higher price. Furthermore, ceramic material can be used as the storage medium (if the heat transfer fluid is a gas) or a phase-change medium (if the heat transfer fluid is water/steam).

These systems can achieve high efficiencies when integrated into gas cycles, and efficiency can even be increased using combined cycles, reaching cycle efficiencies of up to 50 % (Trieb 2007). Moreover, they have the advantage of being able to operate with natural gas during the start-up or when the solar radiation is not sufficient, with a high fossil fuel to electricity conversion efficiency. For large-scale plants, this technology has potentially fewer costs than linear concentration systems as a result of the high working temperature and pressure and, therefore, greater thermodynamic efficiency. This is particularly important in dry refrigeration applications, which operate at elevated ambient temperatures. In these cases, the high working temperatures used in the solar towers means that the drop in power cycle performance is less than with the parabolic-trough or linear Fresnel systems, in spite of the higher working temperature in the condenser.

Solar tower receivers can be tubular or volumetric. In tubular receivers, the solar radiation strikes the tubes through which the heat-transfer fluid circulates. This fluid can be water/steam, liquid sodium, molten nitrate salts or air. With water/steam, the steam leaving the receiver is sent directly to the turbine to generate electricity, without the need for a heat exchanger. Conversely, volumetric receivers absorb the concentrated solar radiation in the interior of a porous body. Here, air is used as the heat-transfer medium, which flows through the porous material and produces convective heating. Creating air suction through the volumetric matrix, the convective losses are negligible. As the gas passes through the absorber volume, its temperature increases at the same time as the temperature of the material increases with depth. Consequently, highest temperatures are reached in the inside of the absorber matrix, thus minimising radiation losses. The porous material can be metallic when working with temperatures of up to 800 °C, or ceramic when the working temperatures are even higher (Fend et al. 2004). There are two main types of volumetric receivers: open (or atmospheric) volumetric receivers and closed (or pressurised) volumetric receivers. The first uses ambient air that is introduced from the outside into the receiver. Once the air has been heated, it flows through a steam generator in a Rankine cycle to produce electricity. The second type of volumetric receiver is closed by a quartz window in which the pressurised air coming from the compressor of a gas turbine cycle is heated (see Fig. 2.9).

At the PSA, an experimental pressurised volumetric receiver system was installed and tested. This plant generated 230 kW$_e$ of electricity and temperatures of 1050 °C were reached in the receiver, with pressures of up to 15 bar. The only commercial solar tower plants are found in Spain. In Seville, there are two power plants known as PS10 and PS20, whose capacities are 11 MW$_e$ and 20 MW$_e$, respectively. Both plants are based on water-steam tubular receiver technology. There is also another tower technology plant located in Seville called Gemasolar, which has a capacity of 19.9 MW$_e$ and uses molten salts both for storage and as the working fluid inside the tubular receiver. Another characteristic of this plant is that
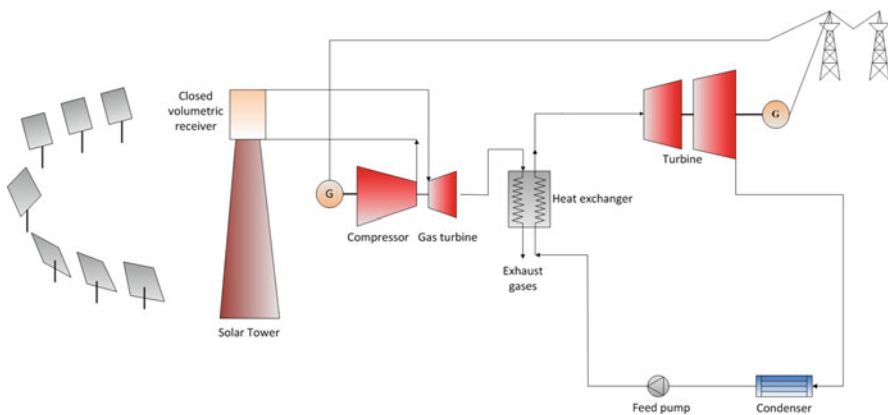

Fig. 2.9 Solar tower coupled to a combined cycle

the storage system is designed so that the plant can operate 24 h a day with only solar energy on certain days of the year.

2.3.4 Parabolic Dishes

Parabolic dishes are made up of an arrangement of mirrors on a parabolic surface, which tracks the sun on two axes in such a way that the focal point is always located in the optical axis of the parabola. The reflective surface (the mirror) reflects the incident solar radiation and concentrates it at the parabolic focal point, close to which the Stirling motor is situated to directly produce electricity using a generator. A Stirling motor is a thermal motor (with a cycle of the same name) that uses gas as the working fluid. The advantage of these systems is the high concentration factors that can be reached, between 1500 and 4000 (Kaltschmitt et al. 2007). In contrast to the systems mentioned previously, parabolic dishes do not require steam generation because the motor works with helium (it has also been tested with hydrogen). The characteristics of these systems are their high efficiency, modularity, autonomous operation and great potential to work with hybrid systems (with solar energy, fossil fuels or both). These systems have proven their high solar-to-electric conversion efficiency (31.25 %) (Moser et al. 2011). The modularity of these systems makes them ideal for isolated systems. The technology is under development phase and its large-scale potential is currently being evaluated. The systems with a Stirling dish have a relatively low electricity generation capacity of less than 25 kW_e. The technology has already been shown to be capable of capacities almost up to 1 MW_e (Braun et al. 2011).

2.3.5 Selection of the Concentrating Solar Power Plant

In principle, all the CSP plants presented above can be used to generate electricity. However, the aim of the research work presented in this book is to select the most favourable of these technologies regarding performance, cost and integration with a desalination plant. Table 2.1 gives a comparison of the different types of CSP plants.

As can be seen in Table 2.1, the maturity of point concentrating systems is not as great as that for line concentrating systems. It is still uncertain whether central receivers will be able to compete with line concentrating systems in the lower temperature range (up to 550 °C) for steam generation. On the other hand, parabolic dish systems only operate in the kilowatt range, so they could be applied for decentralised, remote desalination but not for large-scale applications as presented in this chapter. Until now, line concentrating systems have had clear advantages over other systems as a result of lower costs, less material demands, simpler construction and higher efficiency, making them the best candidates for CSP coupled to desalination. Apart from the line concentrating systems, parabolic-trough collectors have a better track record and reliability than Fresnel systems.

Table 2.1 Characteristics of current concentrating solar power technologies (based on reference (Fichtner and DLR 2011) except where indicated)

Characteristics	Concentration method			
	Line concentrating system		Point concentrating system	
Solar field type	Parabolic trough	Linear Fresnel	Central receiver	Parabolic dish
State of the art	Commercial	Recently commercial	Commercial (Pitz-Paal et al. 2012)	Demonstration projects
Cost of the solar field ($€/m^2$)	300–350	200–250	300–400	>350 (Trieb et al. 2009)
Investment costs ($€/m^2$) for SM1–SM2[a]	3500–6500	2500–4500	4000–6000	6000–10000 (SM1 only)
Typical unit size (MW)	10–250	5–200	10–100	0.1–1
Peak solar efficiency (%)	21	15	<20	31.25
Annual solar efficiency (%)	10–16 (18 projected)	8–12 (15 projected)	10–16 (25 projected)	16–29
Concentration ratio	50–90	35–170	600–1000	up to 3000
Construction requirements	Demanding	Simple	Demanding	Moderate
Operating temperature (°C)	350–415 (550 projected)	270–450 (550 projected)	550–1000	750–900
Heat transfer fluid	Synthetic oil, water/steam	Synthetic oil, water/steam	Air, molten salts, water/steam	air
Thermodynamic power cycle	Rankine	Rankine	Brayton/Rankine	Stirling, Brayton
Power unit	Steam turbine	Steam turbine	Gas, steam turbine	Stirling engine
Experience	High	Low	Moderate	Moderate
Reliability	Long-term proven	Recently proven	Recently proven	Moderate
Thermal storage media	Molten salts, concrete, phase-change material	Molten salts, concrete, phase-change material	Molten salts, concrete, ceramics, phase-change material	No storage available
Combination with desalination	Simple	Simple	Simple	Simple
Integration into the environment	Demanding	Simple	Moderate	Moderate
Operation requirements	Demanding	Simple	Demanding	Simple
Land requirements	High	Low	High	Moderate

[a]*SM* solar multiple

Furthermore, large-scale power production is well proven in commercial plants. Indeed, CSP plants using parabolic-trough collectors represent currently around 90 % of the world's installed capacity, so the research work presented in this book use parabolic-trough technology for CSP in combination with seawater desalination.

2.3.6   Commercial Concentrating Solar Power Plants with Parabolic-Trough Collector Technology

The major development in parabolic-trough collectors emerged in 1985 with the design, commercialisation and installation of nine large CSP plants, known as SEGS. These plants have a nominal power of 340 MW$_e$. They were commercially developed by a group of American, Israeli and German companies and were exploited by the company Luz International Inc. (Los Angeles, CA, USA). These plants were the first to prove the viability of parabolic-trough collector technology to generate electricity, acting as the precursor for the current commercial development in diverse parts of the world, and especially in Spain.

Of the nine new SEGS plants installed by Luz in California, eight are currently in daily operation. A fire occurred in February 1999 in the first of the plants (SEGS-I), which put it out of operation. Table 2.2 lists the location and nominal production of all of these plants.

The nine SEGS plants constructed by the company Luz are located in the Mojave Desert (southern California), and are thermally fed by parabolic-trough collectors, also developed by the same company. The plants were designed to supply maximum power at peak demand, which means a low capacity factor (30 %) and a number of hours equivalent to full-charge running between 2500 and 3000 h/year. A further significant limiting factor is that the SEGS plants are designed to correspond to federal regulations (US Federal Energy Regulatory Commission), meaning that the consumption of fossil fuels in these plants (natural gas) is limited to 25 % of the annual thermal energy input so that they can benefit from the feed-in-tariff legislation regarding renewable energy use. Because of this, and because of the elevated unit cost of thermal storage, these plants have low capacity factors.

The power block of the Californian SEGS plants is conventional. The thermodynamic cycle used in the first plants was a Rankine cycle with no reheating, whereas from SEGS-VI onwards a Rankine cycle with reheating has been used. All these cycles are highly regenerative compared with the cycles in conventional thermal plants, where it is not economically viable to have so many turbine extractions. This difference is a common aspect in all CSP plants and it is a result of the elevated investment costs associated with the plant's solar infrastructure. Any improvement in thermodynamic cycle performance means savings in solar equipment.

Table 2.2 SEGS plants overview

Plant	Net capacity (MW$_e$)	Site	Inaugurated
SEGS I	14	Dagget, CA	1984
SEGS II	30	Dagget, CA	1985
SEGS III	30	Kramer Jn, CA	1986
SEGS IV	30	Kramer Jn, CA	1986
SEGS V	30	Kramer Jn, CA	1987
SEGS VI	30	Kramer Jn, CA	1988
SEGS VII	30	Kramer Jn, CA	1988
SEGS VIII	80	Harper Lake, CA	1989
SEGS IX	80	Harper Lake, CA	1990

All of the Californian SEGS plants use oil as the heat transfer fluid and oil–water heat exchangers, which limit the maximum cycle temperature achievable. Thus, in spite of using highly regenerative cycles, the thermal efficiency is low (30 %) compared with that of conventional fossil fuel plants. To overcome this limitation, SEGS-I to SEGS-VII use a hybrid scheme that allows fossil fuel heat input to increase the thermal efficiency of the cycle. However, this involves the use of a boiler, which carries with it low functioning flexibility making coupling to the solar field difficult.

There follows a brief summary of the main characteristics of the nine SEGS plants (García-Casals 2000).

SEGS-I Plant

The oldest of the SEGS plants had a nominal potential of 13.8 MW$_e$, working with a regenerative Rankine cycle. It occupied a surface area of 90,000 m^2 and started to work on 20th December 1984, costing \$62 million. The solar field had a collector surface area of 82,969 m^2 and comprised 560 collectors, installed in 140 parallel rows. As shown in Fig. 2.10, the thermal oil (ESSO 500) was pumped from the cold oil tank to be heated to 307 °C in the solar field and was then stored in the hot oil tank. From there, the hot oil passed to the steam generator, producing saturated steam at 36.3 bar. The saturated steam was reheated to 416 °C in a natural gas heater before passing to the turbine, where it was expanded.

The hot and cold thermal storage tanks contained 3×10^6 L of oil, providing a storage capacity of 140 MW$_{th}$, which allowed the turbine to keep running on full charge for 3 h. The SEGS-I plant used first-generation collectors (model LS-1) and had a small auxiliary gas heater available that was able to heat the oil in parallel with the solar collector field. With these characteristics, the net thermal cycle efficiency was around 29.6 %. As mentioned above, this plant is now out of service.
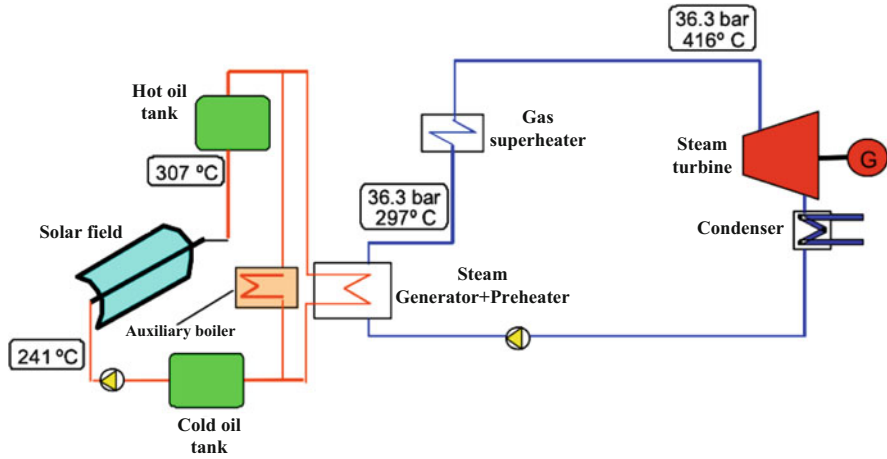
Fig. 2.10   Operating layout of the SEGS-I plant in California

SEGS-II Plant

The SEGS-II plant began construction in February 1985 and went into operation in December of the same year. It has a nominal power of 30 MW$_e$ and cost $95.6 million. The solar collector field covers a surface area of 165,376 m^2. The type of collector used is the LS-1, the same as in the previous plant. However, this plant replaced the mineral oil used in SEGS-I by synthetic oil, allowing an increase in the temperature at the solar field outlet from 307 to 316 °C. This synthetic oil, more expensive than the oil used before, together with the power produced (double that of SEGS-I) made the cost of investment in a storage system prohibitively expensive. As can be seen in Fig. 2.11, this plant retained the use of a gas superheater to improve the solar system's steam characteristics. Moreover, the absence of a storage system motivated the use of a hybrid scheme using a natural gas boiler in parallel with the solar field, offering the possibility of running the plant solely on fossil fuels and thus increasing reliability.

The thermodynamic cycle used in SEGS-II is a regenerative Rankine cycle with no reheating. When running only with solar energy, the high-pressure steam characteristics are even worse than in SEGS-I. Operating like this, the steam temperature from the solar field is between 295 and 300 °C, the pressure remains limited at around 27.2 bar and the cycle's thermal efficiency is 26.7 %. However, in either hybrid mode or running only on fossil fuels, the steam is generated at 510 °C and 103 bar, increasing the net thermal efficiency to 33.9 %.

Such different steam characteristics made it necessary to have a high-pressure turbine, fed exclusively from the auxiliary gas boiler, and a low-pressure chamber fed from the solar system, in this case leaving the high-pressure turbine unused. This cycle characteristic is repeated in the layouts of SEGS plants III–VII.
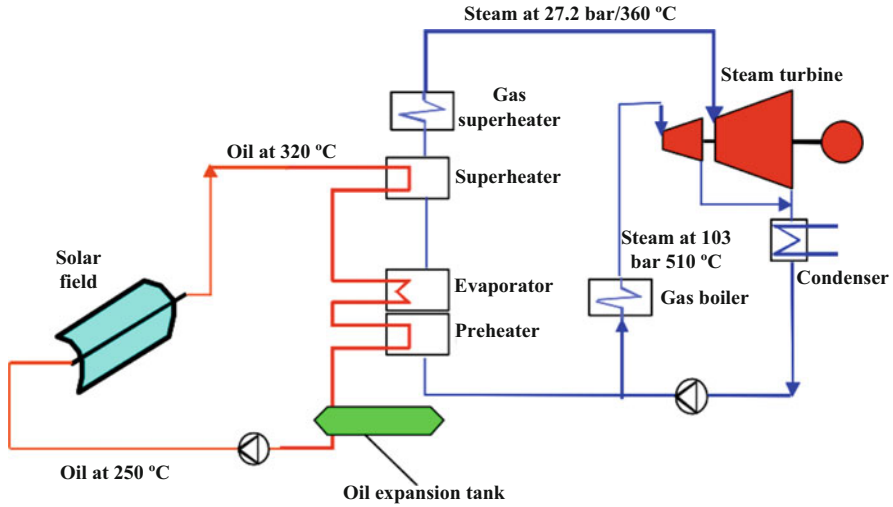
Fig. 2.11 Operating layout of the SEGS II plant in California

SEGS Plants III–V

All of these plants have a nominal potential of 30 MW$_e$, with a regenerative Rankine cycle but no reheating, similar to SEGS-II. The novelty of these plants was the incorporation of a new collector design (LS-2), which was bigger and more economical than the LS-1 model. The construction of SEGS plants III and IV began at the start of 1986 and they went into service on the 18th and 23rd December 1986, respectively. Both had solar collector fields with a surface area of 203,980 m^2. The gas superheater from the SEGS-II plant design was eliminated, and the oil temperature at the outlet of the solar field was raised. As a result of the improvements, each of these plants generated 6 % more electricity than the SEGS-II plant.

The SEGS-V plant went into service in September 1987. Its configuration is essentially the same as that of SEGS plants III and IV. The available solar field collector area is 233,120 m^2. Because the working temperature in these plants is 40 °C above that in the previous two, another type of thermal oil is used, Therminol VP-1 by Solutia, which costs considerably more than ESSO 500. Although the raised working temperature brings with it the inconvenience of a more expensive oil, it has the advantage of achieving greater cycle efficiency (Fig. 2.12).

In these plants, the oil is heated in the solar collector field from a temperature of 250 °C until it reaches 350 °C. The hot oil passes into a steam generator with two chambers, the evaporator and the superheater. In the evaporator, water enters at 177 °C and leaves as saturated steam at 259 °C. This saturated steam is superheated in the second steam generator chamber up to a temperature of 330 °C and pressure of 43.4 bar. The superheated steam passes through to the low-pressure turbine, where it expands. The steam produced by the auxiliary boiler is expanded in the high-pressure turbine.
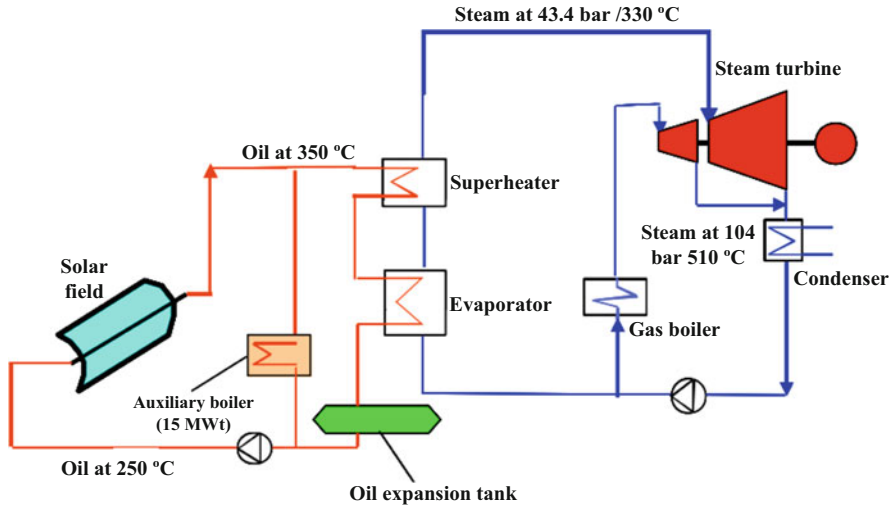
Fig. 2.12 Operating layout of SEGS plants III, IV and V

SEGS plants III, IV and V can run in three different operating modes:

- Feeding the turbine with steam coming from the solar system
- Feeding the turbine with steam only coming from the auxiliary boiler
- In hybrid mode, feeding the turbine simultaneously with steam coming from both the solar system and the auxiliary boiler

These plants have an auxiliary oil boiler (15 MW$_{th}$) to protect the solar field from the dangers of ice and to produce steam for the turbine overnight.

SEGS Plants VI and VII

Starting with SEGS plant VI, the Luz Company incorporated improvements in the design of the parabolic-trough collectors, resulting in an increase in the oil temperature at the solar field outlet up to 395 °C. Other design improvements were also implemented, such as the introduction of a reheater in the regenerative Rankine cycle. SEGS plants VI and VII have the same layout and the solar collectors are also LS-2 type.

The hybrid layout chosen was the same as that for SEGS plants II–V, with a gas boiler in parallel with the solar field, as can be seen in Fig. 2.13. The power of these plants was 30 MW$_e$.

The higher oil temperature at the solar field outlet allows the thermal cycle to generate steam at much higher pressures (100 bar instead of the 43.4 bar in SEGS plants III, IV and V). The reheating process also eliminates the problem of droplet presence in the steam leaving the turbine, which can damage the turbine blades. These conditions, together with use of a specially designed turbine developed by
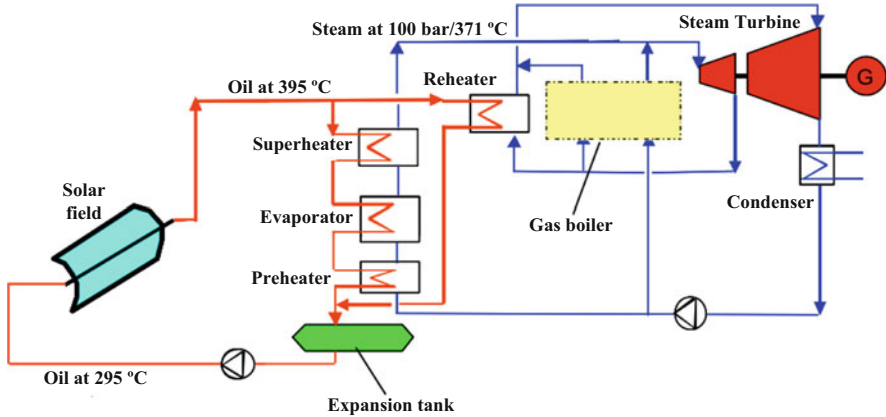
Fig. 2.13 Operating layout of SEGS plants VI and VII

Asea Brown Boveri, led to an increase in overall thermal efficiency of 23 %. There is also an auxiliary boiler in these plants able to produce reheated steam at 510 °C and 100 bar to feed the high-pressure turbine.

SEGS plants VI and VII can operate in three different modes, solar, conventional and hybrid:

- In *solar mode*, the high-pressure turbine is fed with superheated steam at 371 °C and 100 bar produced in the steam generator, which is fed with oil heated to 395 °C from the collector field. After being expanded in the high-pressure turbine, the steam is reheated in the reheater to 371 °C and 17.2 bar, which again is fed by oil coming from the collector field. This reheated steam is expanded in the low-pressure turbine, where it is recondensed before passing again to the preheater of the steam generator, thus closing the cycle. Under these conditions, the thermal efficiency is 34.1 %, which is considerably better than previous attempts.
- In *conventional mode*, the auxiliary boiler produces superheated steam at 510 °C and 100 bar, which is expanded in the high-pressure turbine. Then, the steam again passes to the auxiliary boiler where it is heated to a lower pressure. This reheated steam is then expanded in the low-pressure turbine, where it is finally condensed before passing again to the auxiliary boiler starting the cycle.
- In *hybrid mode*, the turbine is fed simultaneously with steam produced both in the auxiliary boiler and from the steam generator fed from the solar collector field. This operating mode is used during peak electricity demand to keep the turbine running at full charge. Under these conditions, the thermal efficiency is 35.9 %.

By having just one operating pressure in both modes (fossil fuel and solar), the high- and low-pressure turbines are used in all cases. Thus, the high-pressure turbine is not unused when operating only in solar mode.

SEGS Plants VIII and IX

Starting with the construction of SEGS VI and VII, the company Luz International began developing 80 MW$_e$ plants. This size of plant not only has the advantage of economy of scale but also improves the plant's operation as well as significantly reducing operating and maintenance costs. As a consequence, the increase in size provided a 25 % reduction in the cost of electricity generated. The first 80 MW$_e$ plant was SEGS-VIII. Its construction began on 5th April 1989 and it went into service on 28th December of the same year. The two gas boilers of the SEGS V, VI and VII plants were replaced by a single boiler in parallel with the solar field, thus simplifying the layout of the plant. The advantage of this type of hybridisation is that it uncouples the power cycle from the solar part of the plant, providing steady-state conditions at the outlet of the solar/fossil system. The SEGS-IX plant went into service in 1990 and was the last plant installed by Luz before the company ceased operation in 1991. Although Luz had projects at quite advanced stages for four further plants, the company's financial bankruptcy meant they were never realised.

In SEGS plants VIII and IX (Fig. 2.14) there is no steam-to-gas reheater and the turbine has two bodies that work with steam at 371 °C/104 bar and 371 °C/17 bar, respectively. The thermal oil is heated in the solar collectors up to approximately 390 °C, being divided beforehand into two parallel circuits. In one of the circuits, the oil passes through a superheated steam generator and preheater (placed in series) that generate steam at 371 °C and 104 bar. This steam is expanded in the first turbine body and then passes to the reheater, which is thermally fed by the other
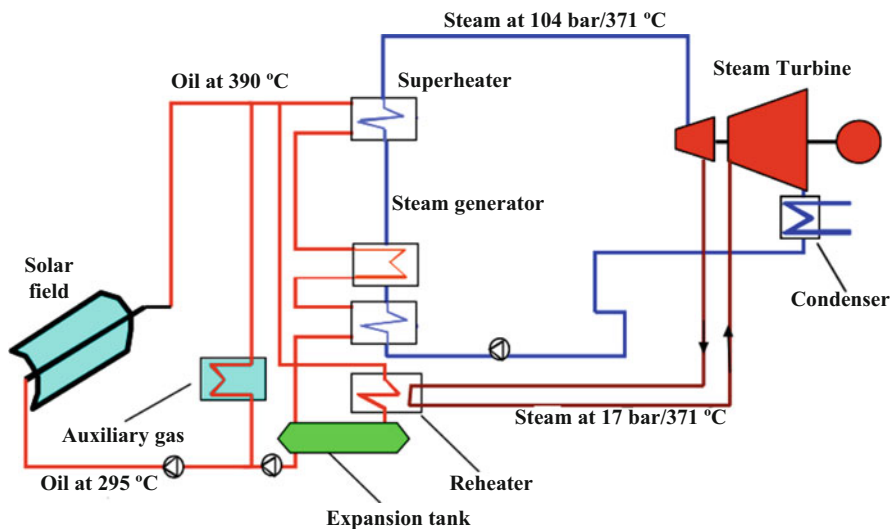

Fig. 2.14 Operating layout of SEGS plants VIII and IX

hot oil circuit. In this way, reheated steam is again obtained at 371 °C and 17 bar. Under these conditions, the net thermal efficiency reached is 34.2 %, running either on solar or hybrid/fossil fuel. During the months of June, July, August and September, the auxiliary gas boiler is used to keep the turbine running at full capacity during peak demand. For the rest of the time, the turbine is only operated using the solar system.

Research and development took place both on the design and improvement of solar collector field components as well as on integrating the power system to allow the technology in large-scale commercial plants to compete directly with conventional power stations. Thanks to this effort, the cost of the solar field per unit area was reduced by 75 % and the thermal performance of the solar system increased by 8 %. After the extensive development of CSP plants that occurred in the 1980s, fossil fuel prices dropped to a quarter of their initial price so no further CSP plants were built for the next 15 years. Currently, commercial activity has re-ignited in this sector with the construction of new plants. In the next section, two representative examples of modern commercial plants are described.

Andasol Plant

Andasol is a solar complex in the province of Granada, Spain, consisting of three CSP plants called Andasol 1, 2 and 3, fed by parabolic-trough collectors. It is expected to be the largest solar CSP plant in Europe, covering more than 202 ha and generating 179,000,000 kWh of electricity a year, operating solely in solar mode.

On 20th July 2006, construction began on Andasol-1 (Fig. 2.15) with a capacity of 50 MW_e. This plant uses synthetic oil as the heat-transfer fluid and has a collector field aperture area of approximately 510,120 m^2, with loops of SKAL-ET parabolic-trough collectors and indirect storage in molten salt tanks with a capacity of 7.5 h at full load. This fact, along with the large field size (the solar field is capable of supplying twice the thermal energy that the turbine can absorb) makes it possible to better control power generation and allow energy to be sent to the electricity grid according to demand.

Nevada Solar One Plant

Nevada Solar One is the largest CSP plant built in the USA since the last SEGS plant in 1991. Owned by Solargenix and Acciona, it has a nominal capacity of 64 MW_e and generates more than 130,000 kWh annually. The plant comprises 357,000 m^2 of second-generation Solargenix (SGX2) parabolic-trough collectors, developed by Solargenix and NREL. The absorber tubes used were supplied by Solel in Israel (30 %) and Schott in Germany (70 %). Flabeg Solar provided the reflector mirrors, although the company also installed other mirror models for testing. The power block consists of a regenerative Rankine cycle with reheating. The turbine was supplied by Siemens. As the State of Nevada only permits 2 % of

Fig. 2.15 Solar field of the Andasol-1 plant

Fig. 2.16 Nevada Solar One CSP plant

fossil fuel hybridisation, the auxiliary natural gas boiler is very small and is basically used to avoid oil solidification. It is for this reason that the system has a 30-min storage capacity, which serves to minimise transitory effects. Figure 2.16 shows an aerial view of the plant.

2.4   Combination of CSP and Desalination Plants

Seawater desalination demands a great deal of energy and, with the looming energy crisis caused by the end of the petrol era, it is predicted that water shortage problems will be greater in the short to medium term. On the other hand, most of the regions facing severe water deficits also have high levels of solar radiation and are near the sea (Blanco et al. 2009). Such is the case in the Mediterranean and the Arabian Gulf areas, both of which are experiencing ever-greater water shortage problems. The Arabian Gulf region in particular has substantial potential to develop and implement CSP plants, given the high solar radiation levels it receives. The cogeneration of water and electricity using solar energy (CSP + D) offers one of the most sustainable solutions, because this concept can potentially resolve both water and energy problems in parts of the world that are arid or semi-arid (Blanco et al. 2010). These systems are of considerable interest as they offer a reduction in both the water and electricity generating costs compared with individual solar plants. Furthermore, costs can be optimized by using the infrastructure better and benefiting from the economy of scale from the steam turbine (Blanco et al. 2009). Another advantage is the reduction in greenhouse gas emissions from fresh water production, as most desalination plants currently in operation use fossil fuels as the energy source for the desalination process. As an important preventative measure, the use of these systems can help to mitigate existing national and international conflicts caused by water and energy shortages, and can reduce potential economic risks related to the increase in non-renewable fuel costs (Trieb et al. 2001; Weinrebe et al. 1998).

As mentioned before, RO and MED processes have been selected as the most promising desalination technologies for coupling to CSP plants using parabolic-trough collector technology. In the thermal desalination process (MED), the steam coming from the turbine outlet is used as the energy source for the desalination process. In this instance, the CSP plant should be situated as close as possible to the desalination plant because the low steam density exiting the turbine makes it necessary to have large diameter pipes through which the steam flows towards the desalination plant. On the other hand, if the desalination process is driven using mechanical energy (RO), the electrical energy needed to pressurise the salt water comes from the CSP plant and the CSP plant and the desalination plant can be situated in different places. The preference for a desalination system using evaporation or a system driven by mechanical energy coupled to a CSP plant depends on various factors, such as the electricity/water ratio required, the cost of the energy needed in the desalination process, electricity sales, investment costs and the requirements at the time of designating the location for this type of system (Mussati et al. 2003). However, there are many technological aspects of these integrated systems that remain problematic. For this reason, research and development as well as demonstration activities are necessary to define the best possible cogeneration concepts and layouts.

One such aspect is the cost and availability of land in cases where the CSP plant is situated in areas close to the sea. Furthermore, in such areas, the DNI value is normally less so it is preferable that these plants are as far from the coast as

possible. CSP + D coupling can also involve a reduction in the efficiency of the CSP plant as a result of, on the one hand, the plant's RO electricity consumption and, on the other, less efficient turbines in the case of MED because a higher steam temperature is required at the turbine outlet. Other aspects to bear in mind are the high water consumption necessary in the CSP plant, both in the cooling system (in the case that it is wet cooling) and for mirror washing, as well as the reduction in electricity generation that a dry cooling system involves.

Solar energy, and indeed renewable energy sources in general, are resources that typically vary depending on the weather. This is a problem for desalination plants because they need to be operating continually, even when working at partial load. Therefore, a techno-economic analysis that accommodates this, and other aspects, is necessary in selecting the best alternative for producing fresh water and electricity safely and sustainably. Such an analysis is carried out in the research work presented in this book, focusing on the Mediterranean and the Arabian Gulf regions. Although no CSP + D plant yet exists, a bibliographic revision of the scientific literature has allowed us to identify a series of theoretical works dealing with the coupling of desalination units to CSP plants. The first works on the subject were published by Trieb et al. (2002, 2009), and Trieb and Müller-Steinhagen (2008), who researched the possibility of combining CSP and desalination plants in the MENA region and southern Europe. In these works, the authors concluded that CSP + D systems are a safe and sustainable solution, capable of addressing the growth deficits present in these regions. Other works have demonstrated CSP + D potential in specific locations, such as the Gaza Strip (Hamdan et al. 2008), New Mexico (Téllez et al. 2009), Oman (Gastli et al. 2010), south-east Spain (Palenzuela et al. 2011a) and Abu Dhabi (Palenzuela et al. 2011b). Economic studies have also been reported. Olwig et al. (2012) performed a techno-economic study of the combination of parabolic-trough power plants for electricity and water production with MED and ultrafiltration (UF)-RO plants at two specific locations in Israel (Ashdod) and Jordan (Aqaba). The results showed that the configuration with RO had economic benefits compared with the CSP + MED configuration, except for very high electricity prices. Fylaktos et al. (2014) carried out an economic analysis of three different CSP configurations: a CSP plant for electricity only, for electricity with RO and for electricity with MED. The results showed that the CSP + D concept was feasible, although the best economic results were for the electricity-only plant.

Because of the lack of real plant implementation, all the analyses carried out for CSP + D plants so far have been based on simulations. Some authors have developed time-dependent models in order to determine the cogeneration plant annual production, combined with the costs of the electricity and water production (Schmitz et al. 2009; Moser et al. 2010; 2011). Others developed time-dependent system-level models in order to optimise the operation of a cogeneration solar–thermal plant (Ghobeity et al. 2011), and others developed transient models for the CSP plant considering different cooling systems for the power cycle: once-through cooling and a combination of MED and once-through systems (Casimiro et al. 2013).

Research work has also been carried out on cogeneration plant layouts, where the desalination plant consists of a hybrid system. Alrobaei (2008) published a thermal and environmental analysis of two cogeneration layouts. The first consisted of a CSP plant of parabolic-trough collectors with a steam cycle coupled to a hybrid RO/LT-MED system. The second layout consisted of the same cogeneration plant but integrated with a gas turbine. This gas turbine was tasked with increasing electricity generation in the steam turbine using its residual heat to generate additional steam. The results showed that the latter cogeneration layout was the more effective of the two from technical, economic and sustainability points of view.

2.5 Cooling Systems in CSP plants

An important aspect to bear in mind with CSP plants is the selection of the most appropriate power block cooling system. In the case of combined CSP + D systems, this choice is all the more important. Current CSP plants are similar in design to conventional power plants and normally use wet cooling systems to condense the steam leaving the turbine. This can be accomplished in two ways: once-through cooling or evaporative cooling. With once-through cooling, the exhaust steam coming from the power plant is condensed in a shell and tube condenser using water as the coolant. Normally, seawater is used, which is taken from the sea and passes through the condenser tube bundle before returning back to the sea at a considerably higher temperature, transferring the sensible heat to the steam that circulates inside the shell. Once-through cooling demands large volumes of water, generally in quantities in the order of 90,000–100,000 m^3/MWh (US DoE 2009). In this case, a grave danger exists of serious environmental impact as a result of the death of marine fauna in the water suction process and severe alterations in the ecosystem caused by returning large volumes of seawater at significantly higher temperatures than when they were taken. Furthermore, in this process a large amount of energy is dissipated into the environment, thus contributing to global warming and climate change as well as severely damaging the biosphere. On the other hand, in evaporative water cooling, the cooling water gives up the heat it has acquired passing through the condenser. Here, the coolant is fresh water instead of seawater to avoid scaling problems in the cooling tower. The hot water coming from the condenser is vaporised in a water distribution system and falls uniformly onto a porous filling, through which counter-current air circulates. Coming into contact with the hot water, the air forms a film of humid air around each droplet. This water thus evaporates, extracting the necessary heat for the liquid's evaporation and thus cooling it. The humid air passes up and out of the cooling tower, visible as plumes (and as such having a certain visual impact) (see Fig. 2.17). As part of the fresh water is evaporated, this cooling method requires a constant supply of water. The main advantage is that the water input is far less than with once-through cooling and therefore the environmental impact of the CSP plants using evaporative water cooling is likewise less. Evaporative water cooling is, by far, the most-used system for eliminating excess heat in thermo-solar, cogeneration and combined-cycle plants.

Fig. 2.17 Cooling towers
in a CSP plant

However, if the tendency to use wet cooling continues to grow in the new CSP plants, water consumption for this purpose could more than double by 2030 (US DoE 2006). Added to this is the fact that the geographical areas where CSP plants are more productive are usually the same areas that experience water scarcity, commonly suffering restrictions in water supply and severe environmental regulations. Air or dry cooling systems thus offer a viable alternative to traditional wet systems. These systems considerably reduce water consumption of the CSP plant to about 0.30–0.34 m^3/MWh (Turchi and Kutscher 2009). However, although there is considerable potential for water-use savings with dry cooling systems, they also carry with them drawbacks such as reduced electricity generation, increased need for auxiliary power (the air condensers require more electricity for ventilation than wet systems) and increased investment costs. Some studies show that the cost per unit of energy generated (levelised electricity cost, LEC) rises by 5–10 % (Richter and Dersch 2009). The LEC parameter is used to study the economic viability of different electricity-generating installation alternatives and is defined as the annual cost divided by the average annual production forecast.

Several works have evaluated and compared the existing cooling methods of a power plant. The authors of this book carried out an evaluation of wet (evaporative water and once-through) and dry cooling technologies for different CSP + D configurations (with MED and RO desalination plants) in the Mediterranean area and the Arabian Gulf (Palenzuela et al. 2013, 2015). It was found that the use of evaporative water cooling was the most economical in terms of electricity production. However, the cost of water was higher than for the once-through and dry cooling systems. Furthermore, an exergy analysis was performed to compare two

different cooling technologies for the power cycle of a 50 MW$_e$ solar thermal power plant (Blanco-Marigorta et al. 2011). The first design configuration used a cooling tower and the second configuration used an air-cooled condenser. It was concluded that, from an exergetic point of view, the use of an air-cooled condenser was not an efficient solution for working at low exit turbine pressures, which is the case for the Mediterranean area. However, it became more competitive at the higher pressures corresponding to much warmer regions.

Another more economic way to lower water consumption is the use of hybrid systems. With these, electricity generation close to 100 % can be achieved, even at high ambient temperatures. However, they involve elevated costs because both a cooling tower and an air condenser are required. Normally, hybrid cooling systems working in parallel are used (see Fig. 2.18).

Hybrid cooling systems have likewise been analysed by various authors. Barigozzi et al. (2011) carried out a detailed simulation of a hybrid cooling system used to cool the outlet steam from a cogeneration plant located in Brescia, northern Italy. The results of the simulation showed that the best cooling strategy consisted of cooling most of the steam using wet cooling, thus reducing the operating cost of the dry cooling system. On the other hand, Richter and Dersch (2009) carried out a study of various wet and dry cooling system combinations using simulations. They concluded that using hybrid systems reduced the energy cost penalisation compared with using only a dry cooling system, and resulted in a saving of approximately 80 % of the water required compared with a plant solely cooled by water.
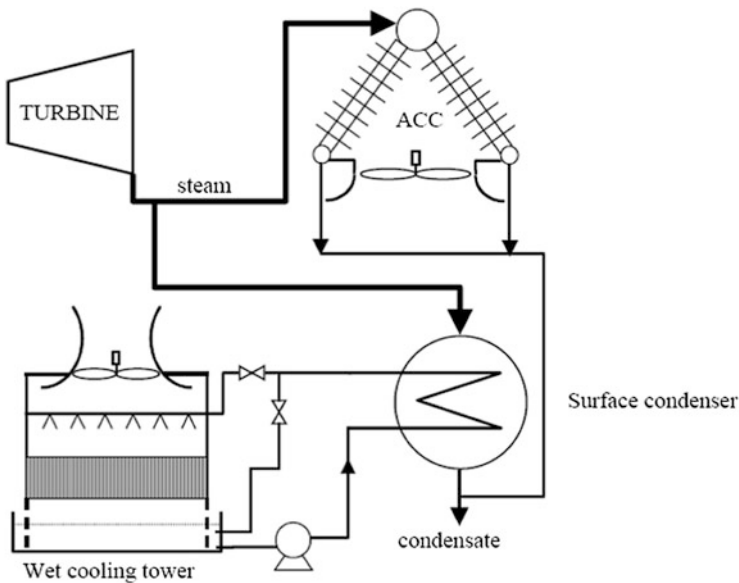

Fig. 2.18 Layout of a hybrid cooling system working in parallel

References

Adak, A. K., & Tewari, P. K. (2014). Technical feasibility study for coupling a desalination plant to an advanced heavy water reactor. *Desalination, 337*, 76–82.

Alexopoulos, S., & Hoffschmidt, B. (2010). Solar tower power plant in Germany and future perspectives of the development of the technology in Greece and Cyprus. *Renewable Energy, 35*, 1352–1356.

Al-Mutaz, I. S. (2003). Coupling of a nuclear reactor to hybrid RO-MSF desalination plants. *Desalination, 157*, 259–268.

Almulla, A., Hamad, A., & Gadalla, M. (2005). Integrating hybrid systems with existing thermal desalination plants. *Desalination, 174*, 171–192.

Ansari, K., Sayyaadi, H., & Amidpour, M. (2010). Thermoeconomic optimization of a hybrid pressurized water reactor (PWR) power plant coupled to a multi effect distillation desalination system with thermo-vapor compressor (MEDTVC). *Energy, 35*, 1981–1996.

Alrobaei, H. (2008). Novel integrated gas turbine solar cogeneration power plant. *Desalination, 220*, 574–587.

Barigozzi, G., Perdichizzi, A., & Ravelli, S. (2011). Wet and dry cooling systems optimization applied to a modern waste-to-energy cogeneration heat and power plant. *Applied Energy, 88*, 1366–1376.

Blanco, J., Malato, S., Fernández-Ibañez, P., Alarcón, D., Gernjak, W., & Maldonado, M. I. (2009). Review of feasible solar energy applications to water processes. *Renewable and Sustainable Energy Reviews, 13*, 1437–1445.

Blanco, J., Alarcón, D., Zaragoza, G., Guillén, E., Palenzuela, P., & Ibarra, M. (2010, September 21–24). Expanding CSP research frontier: Challenges to be addressed by combined solar power and desalination plants. In: *Proceedings of the 15th SolarPACES Symposium. The CSP Conference: Electricity, Fuels and Clean Water from Concentrated Solar Energy, Perpignan, France.*

Blanco-Marigorta, A. M., Sanchez-Henríquez, M. V., & Peña-Quintana, J. A. (2011). Exergetic comparison of two different cooling technologies for the power cycle of a thermal power plant. *Energy, 36*, 1966–1972.

Bouzayani, N., Galanis, N., & Orfi, J. (2009). Thermodynamic analysis of combined electric power generation and water desalination plants. *Applied Thermal Engineering, 29*, 624–633.

Braun, F. G., Hooper, E., Wand, R., & Zloczysti, P. (2011). Holding a candle to innovation in concentrating solar power technologies: A study drawing on patent data. *Energy Policy, 39*, 2441–2456.

Buck, R., Lüpfert, E., & Tellez, F. (2000, March). Receiver for solar-hybrid gas turbine and combined cycle systems (REFOS). In: *Proceedings IEA Solar Thermal 2000 Conference, Sydney, Australia.* Retrieved from http://www.dlr.de/TT

Casimiro, S., Cardoso, J., Alarcón-Padilla, D. C., Turchi, C., Ioakimidis, C., & Farinha Mendes, J. (2013). Modeling multi effect distillation powered by CSP in TRNSYS. *Energy Procedia, 49*, 2241–2250.

Cengel, Y. A., & Boles, M. A. (2007). *Thermodynamics. An engineering approach* (6th ed.). New York: McGraw Hill.

Clelland, D. W., & Stewart, J. M. (1966). The optimisation and design of large scale multi-stage flash distillation plants. *Desalination, 1*, 61–76.

Darwish, M. A., & Al Najem, N. (2004). Co-generation power desalting plants: New outlook with gas turbines. *Desalination, 161*, 1–12.

Darwish, M. A., Al-Awadhi, F. M., Akbar, A., & Darwish, A. (2009a). Alternative primary energy for power desalting plants in Kuwait: The nuclear option I. *Desalination and Water Treatment, 1*, 25–41.

Darwish, M. A., Eleshaky, M. E., Al-Najem, N. M., & Alazmi, B. S. A. (2009b). Alternative primary energy for power desalting plants in Kuwait: The nuclear option II-The steam cycle and its combination with desalting units. *Desalination and Water Treatment, 1*, 42–57.

de Lalaing, J. (2001). The Solarmundo project—Advanced Fresnel technology for thermal power generation, Conferences in Frankfurt and Brussels, http://www.solarmundo.de

Desertec Foundation. (2010). *Red paper: An overview of the Desertec concept*. Hamburg, Germany: Desertec Foundation. Retrieved June 25, 2015 from http://www.desertec.org/fileadmin/downloads/desertec-foundation_redpaper_3rd-edition_english.pdf

Eck, M. (2009, September 15–18). Test and demonstration of the direct steam generation at 500°C. In: *Proceedings of the 15th SolarPACES Symposium. The CSP Conference: Electricity, Fuels and Clean Water from Concentrated Solar Energy, Berlin, Germany*.

Eck, M., & Steinmann, W. (2005). Modelling and design of direct solar steam generating collector fields. *Journal of Solar Energy Engineering, 127*, 371–380.

El-Nashar, A. M. (2001). Cogeneration for power and desalination: State of the art review. *Desalination, 134*, 7–28.

El-Nashar, A. M., & El-Baghdady, A. (1984). Analysis of water desalination and power generation expansion plans for the Emirate of Abu Dhabi—A preliminary study. *Desalination, 49*, 271–292.

Fend, T., Pitz-Paal, R., Reutter, O., Bauer, J., & Hoffschmidt, B. (2004). Two novel high-porosity materials as volumetric receivers for concentrated solar radiation. *Solar Energy Materials and Solar Cells, 84*, 291–304.

Fernández-García, A., Zarza, E., Valenzuela, L., & Pérez, M. (2010). Parabolic-trough solar collectors and their applications. *Renewable and Sustainable Energy Reviews, 14*, 1695–1721.

Fichtner and DLR. (2011). *MENA regional water outlook. Part II: desalination using renewable energy*. Stuttgart, Germany. Retrieved from http://www.dlr.de/tt/Portaldata/41/Resources/dokumente/institut/system/projects/MENA_REGIONAL_WATER_OUTLOOK.pdf

Fylaktos, N., Mitra, I., Tzamtzis, G., & Papanicolas, C. M. (2014). Economic analysis of an electricity and desalinated water cogeneration plant in Cyprus. *Desalination and Water Treatment*. doi:10.1080/19443994.2014.940219.

García-Casals, V. (2000). *Optimización del acoplamiento entre subsistema solar y ciclo termodinámico en plantas termosolares. Doctoral Thesis*. Madrid, Spain: Universidad Politécnica de Madrid.

Gastli, A., Charabi, Y., & Zekri, S. (2010). GIS-based assessment of combined CSP electric power and seawater desalination plant for Duqum—Oman. *Renewable and Sustainable Energy Reviews, 14*, 821–827.

Ghobeity, A., Noone, C. J., Papanicolas, C. N., & Mitsos, A. (2011). Optimal time-invariant operation of a power and water cogeneration solar-thermal plant. *Solar Energy, 85*, 2295–2320.

Hamdan, L. K., Zarei, M., Chianelli, R. R., & Gardner, E. (2008). Sustainable water and energy in Gaza Strip. *Renewable Energy, 33*, 1137–1146.

Hamed, O. A. (2005). Overview of hybrid desalination systems—Current status and future prospects. *Desalination, 186*, 207–214.

Hamed, O. A., Al-Washmi, H. A., & Al-Otaibi, H. A. (2006). Thermoeconomic analysis of a power/water cogeneration plant. *Energy, 31*, 2699–2709.

Hornburg, C. D., & Cruver, J. E. (1977). Dual purpose power/water plants utilizing both distillation and reverse osmosis. *Desalination, 20*, 27–42.

Hosseini, S. R., Amidpour, M., & Behbahaninia, A. (2011). Thermoeconomic analysis with reliability consideration of a combined power and multi stage flash desalination plant. *Desalination, 278*, 424–433.

Hosseini, S. R., Amidpour, M., & Shakib, S. E. (2012). Cost optimization of a combined power and water desalination plant with exergetic, environment and reliability consideration. *Desalination, 285*, 123–130.

Kaltschmitt, M., Streicher, M., & Wiese, A. (2007). *Renewable energy*. Berlin, Heidelberg: Springer.

Kamal, I. (2005). Integration of seawater desalination with power generation. *Desalination, 180*, 217–229.

Kronenberg, G. (1996). Cogeneration with the LT-MED desalination process. *Desalination, 108*, 287–294.

Kronenberg, G., & Lokiec, F. (2001). Low-temperature distillation processes in single- and dual-purpose plants. *Desalination, 136*, 189–197.

Luo, C., Zhang, N., Lior, N., & Lin, H. (2011). Proposal and analysis of a dual-purpose system integrating a chemically recuperated gas turbine cycle with thermal seawater desalination. *Energy, 36*, 3791–3803.

Madani, A. A. (1996). Analysis of a new combined desalination-power generation plant. *Desalination, 105*, 199–205.

Mahbub, F., Hawlader, M. N. A., & Mujumdar, A. S. (2009). Combined water and power plant (CWPP)-a novel desalination technology. *Desalination and Water Treatment, 5*, 172–177.

Manesh, M. H., & Amidpour, M. (2009). Multi-objective thermoeconomic optimization of coupling MSF desalination with PWR nuclear power plant through evolutionary algorithms. *Desalination, 249*, 1332–1344.

Solar Millennium. (2009). *The parabolic trough power plants Andasol 1 to 3: The largest solar power plants in the world—Technology premiere in Europe*. Erlangen: Solar Millennium. Retrieved 26 June, 2015, from http://www.rwe.com/web/cms/mediablob/en/1115150/data/1115144/1/rwe-innogy/sites/solar-power/andasol-3/facts-figures/Further-information-about-Andasol.pdf

Moser, M., Trieb, F., & Kern, J. (2010, October 3–7). Combined water and electricity production on industrial scale in the MENA countries with concentrating solar power. In: *Proceedings of EuroMed Conference: Desalination for Clean Water and Energy—Cooperation Among Mediterranean countries, Tel Aviv, Israel.*

Moser, M., Trieb, F., Kern, J., Allal, H., Cottret, N., Scharfe, J., Tomasek, M., & Savoldi, E. (2011). The MED-CSD project: Potential for concentrating solar power desalination development in Mediterranean countries. *Journal of Solar Energy Engineering, 133*, 031012. doi:10.1115/1.4004352 (8 pages).

Mussati, S., Aguirre, P., & Scenna, N. (2003). Dual-purpose desalination plants. Part II optimal configuration. *Desalination, 153*, 185–189.

OECD/IEA. (2014). *World Energy Outlook 2014*. Paris: International Energy Agency. Retrieved from https://www.iea.org/publications/freepublications/publication/WEO_2014_ES_English_WEB.pdf.

Olwig, R., Hirch, T., Sattler, C., Glade, H., Schmeken, L., & Will, S. (2012). Techno-economic analysis of combined concentrating solar power and desalination plant configurations in Israel and Jordan. *Desalination and Water Treatment, 41*, 9–25.

Palenzuela, P., Zaragoza, G., Alarcón, D., & Blanco, J. (2011a). Simulation and evaluation of the coupling of desalination units to parabolic-trough solar power plants in the Mediterranean region. *Desalination, 281*, 379–387.

Palenzuela, P., Zaragoza, G., Alarcón-Padilla, D. C., Guillén, E., Ibarra, M., & Blanco, J. (2011b). Assessment of different configurations for combined parabolic-trough (PT) solar power and desalination plants in arid regions. *Energy, 36*, 4950–4958.

Palenzuela, P., Zaragoza, G., Alarcón-Padilla, D. C., & Blanco, J. (2013). Evaluation of cooling technologies of concentrated solar power plants and their combination with desalination in the mediterranean area. *Applied Thermal Engineering, 50*, 1514–1521.

Palenzuela, P., Alarcón-Padilla, D. C., & Zaragoza, G. (2015). Large-scale solar desalination by combination with CSP: Technoeconomic analysis of different options for the Mediterranean Sea and the Arabian Gulf. *Desalination, 366*, 130–138.

Pharabod, F., & Philibert, C. (1991). *LUZ solar power plants. Success in California and worldwide prospects*. Cologne, Germany: DLR/SolarPACES.

Pitz-Paal, R., Amin, A., Oliver Bettzuge, M., Eames, P., Flamant, G., & Fabrizi, F. (2012). Concentrating solar power in Europe, the Middle East and North Africa: A review of development issues and potential to 2050. *Journal of Solar Energy Engineering, 134*, 024501–024506.

Price, H., & Kearney, D. (1999, January). *Parabolic-trough technology roadmap: A pathway for sustained commercial development and deployment of parabolic-trough technology* (Final Report). Golden, CO: U.S. Department of Energy, National Renewable Energy Laboratory. Retrieved June 25, 2015, from http://library.umac.mo/ebooks/b12549289.pdf

Rensonnet, T., Uche, J., & Serra, L. (2007). Simulation and thermoeconomic analysis of different configurations of gas turbine (GT)-based dual-purpose power and desalination plants (DPPDP) and hybrid plants (HP). *Energy, 32*, 1012–1023.

Richter, C., & Dersch, J. (2009, September 15–18). Methods for reducing cooling water consumption in solar thermal power plants. In: *Proceedings of the 15th SolarPACES Symposium. The CSP conference: Electricity, fuels and clean water from concentrated solar energy, Berlin, Germany.*

Sandia National Laboratories. (2008). Sandia, Stirling Energy Systems set new world record for solar-to-grid conversion efficiency. Albuquerque, New Mexico: Sandia National Laboratories. Retrieved June 25, 2015, from http://www.sandia.gov/news/resources/releases/2008/solargrid.html

Schmitz, K. D., Riffelmann, K. J., & Thaufelder, T. (2009, September 15–18). Techno-economic evaluation of the cogeneration of solar electricity and desalinated water. In: *Proceedings of the 15th SolarPACES Symposium. The CSP Conference: Electricity, Fuels and Clean Water from Concentrated Solar Energy, Berlin, Germany.*

Shakib, S. E., Amidpour, M., & Aghanajafi, C. (2012). Simulation and optimization of multi effect desalination coupled to a gas turbine plant with HRSG consideration. *Desalination, 285*, 366–376.

Tamme, R., Laing, D., & Steinmann, W-D. (2004). Advanced Thermal Energy Storage Technology for Parabolic Trough. *Journal of Solar Energy Engineering, 126*, 794–800.

Téllez, D., Lom, H., Chargoy, P., Rosas, L., Mendoza, M., Coatl, M., Macías, N., & Reyes, R. (2009). Evaluation of technologies for a desalination operation and disposal in the Tularosa Basin, New Mexico. *Desalination, 249*, 983–990.

Trieb, F., & Müller-Steinhagen, H. (2008). Concentrating solar power for seawater desalination in the Middle East and North Africa. *Desalination, 220*, 165–183.

Trieb, F. et al. (2001). Electricity and water from solar powered steam cycle plants (Strom und Trinkwasser aus solaren Dampfkraftwerken). *Energiewirtschaftliche Tagesfragen 51*(6): 386–390. Retrieved from www.dlr.de/tt/system.

Trieb, F., Nitsch, J., Kronshage, S., Schillings, C., Brischke, L-A., Knies, G., & Czisch, G. (2002). Combined solar power and desalination plants for the Mediterranean region-sustainable energy supply using large-scale solar thermal power plants. *Desalination, 153*, 39–46.

Trieb, F., Müller-Steinhagen, H., Kern, J., Scharfe, J., Kabariti, M., & Al Taher, A. (2009). Technologies for large scale seawater desalination using concentrated solar radiation. *Desalination, 235*, 33–43.

Turchi, G., & Kutscher, C. (2009). *Water use in concentrating solar power (CSP), Tucson.* Retrieved from http://www.swhydro.arizona.edu/renewable/presentations/thursday/turchi.pdf

Uche, J., Serra, L., & Valero, A. (2001). Thermoeconomic optimization of a dual-purpose power and desalination plant. *Desalination, 136*, 147–158.

US DoE. (2006). *Energy demands on water resources: Report to Congress on the Interdependency of Energy & Water.* Retrieved from http://powi.ca/wp-content/uploads/2012/12/Energy-Demands-on-Water-Resources-Report-to-Congress-2006.pdf

US DoE. (2009). *Concentrating solar power commercial application study: Reducing water consumption of concentrating solar power electricity generation.* Washington, DC: U.S. Department of Energy. Retrieved June 25, 2015, from https://www1.eere.energy.gov/solar/pdfs/csp_water_study.pdf

Wang, Y., & Lior, N. (2007). Performance analysis of combined humidified gas turbine power generation and multi-effect thermal vapor compression desalination systems: Part 2: The evaporative gas turbine based system and some discussions. *Desalination, 207*, 243–256.

Webber, M. E. (2008). Catch-22: Water vs. Energy. *Scientific American, 18*, 34–41.

Weinrebe, G., Bönkhe, M., & Trieb, F. (1998). Life cycle assessment of an 80 MW SEGS plant and a 30 MW PHOEBUS Power Tower. In*: Proceedings of the ASME International Solar Energy Conference, Albuquerque.* Retrieved from http://www.dlr.de/system

Winter, C. J., Sizmann, R. L., & Vant-Hull, L. L. (1990). *Solar power plants: Fundamentals, technology, systems, economics.* Berlín, Germany: Springer. ISBN 3-540-18897-5.

Yang, L., & Shen, S. (2007). Assessment of energy requirement for water production at dual-purpose plants in China. *Desalination, 205*, 214–223.

Zachary, J., & Layman, C. M. (2009, September 15–18). Integration of desalination in hybrids for solar and conventional fossil power plants. In: *Proceedings of the 15th SolarPACES Symposium. The CSP Conference: Electricity, Fuels and Clean Water from Concentrated Solar Energy, Berlin, Germany.*

Chapter 3
Steady-State Modelling of a Low-Temperature Multi-effect Distillation Plant

Nomenclature

Symbols

A	Heat transfer area (m^2)
C_p	Specific heat (kJ/kg°C)
M	Mass flow rate (kg/s)
M'	Mass flow rate by flashing process (kg/s)
N	Total number of effects
NEA	Non-equilibrium allowance (°C)
PR	Performance ratio
Q	Heat transfer rate (kW)
T	Temperature (°C)
T'	Temperature by flashing process (°C)
U	Overall heat transfer coefficient (kW/m^2°C)
X	Salt concentration (g/kg)
TTL	Thermodynamic loss (°C)

Greek

λ	Latent heat of evaporation (kJ/kg)

Subscript

b	Reject brine
v	Vapour entering, leaving (as distillate) and generated inside the evaporator or effect
c	Condenser

cw   Cooling seawater
sw   Seawater
d   Distillate
da   Distillate from the distribution system
dr   Distillate entering the mixers in the distribution system
dm   Portion of distillate distributed between the effects and the mixers
vh   Vapour consumed by preheater or distillate generated in the preheater
gb   Generated vapour by boiling
gf   Generated vapour by flashing
f   Feedwater
fv   Generated vapour by boiling and flashing
s   Heating steam in the first effect
eff Effect
ph   Preheater
vc   Vapour in the condenser

3.1 Introduction

This chapter describes the development of a mathematical model of a vertically stacked, forward feed (FF), low-temperature multi-effect distillation (LT-MED) plant. The model was developed by taking into consideration the same design and operational characteristics as the pilot multi-effect distillation (MED) plant at Plataforma Solar de Almería, in the southeast of Spain. The model has been validated, comparing the results of the model with the experimental data from the pilot plant.

3.2 MED Plants: State of the Art

Numerous MED models have been developed and described in the scientific literature. El-Sayed and Silver (1980) developed one of the earliest models for a FF-MED plant, in which they calculated the performance ratio and heat transfer areas using several simplifying thermodynamic assumptions. El-Dessouky and Ettouney (1998, 1999, 2002) developed detailed mathematical models to study how design and operation variables affect the parameters related to the cost of desalinated water production. Darwish et al. (2006, 2008) analysed various configurations of MED plants, finding the trade-off between performance ratio and required heat transfer area. The work published by Druetta et al. (2013) was also based on the modelling of different configurations of MED (different flow-patterns for the distillate and the vapour streams), which were simultaneously optimized to determine the best stream flow patterns with respect to the flow patterns in a conventional FF-MED plant. Results showed that modification of the flow patterns

improved process performance, reducing the process-specific total heat transfer area by about 5 % compared with the conventional case. Gautami and Khanam (2012) also studied a selection of the optimum configuration for MED plants. They presented 14 models, which were compared in terms of the conversion factor and vapour consumption of the desalination plant.

Other works considering optimisation in MED process have also been published. Jyoti and Khanam (2014) developed the model of a MED system for different operating configurations, such as steam splitting, condensate flashing and vapour bleeding. Likewise, they optimized the number of flash tanks in the system on the basis of an economic analysis. As a result, a modified system was found that enhanced the steam economy by 23.77 % and reduced steam consumption by 36.76 %. Piacentino and Cardona (2010) proposed a thermo-economic analysis of a single-effect plant for optimisation of a six-effect MED plant, which led to an in-depth understanding of the interactions between exergy and fluid flows. It was shown that the thermodynamic margins for improvement are limited by the functional scope of heat exchangers at the evaporators. Zhao et al. (2011) presented a steady-state mathematical model of a backward feed MED plant for desalination of high-salinity wastewater from a typical refinery. The focus of this work was optimisation of process parameters such as the number of effects, performance ratio, feed steam flow rate, minimum temperature difference between effects and economic efficiency.

Other authors focused on the effect of several parameters of the MED system on its performance. El-Allawy (2003) examined how the energy efficiency of a MED system (with and without thermal vapour compression) varied with the top brine temperature (TBT) and the number of effects. Results revealed that an increase in the number of effects from three to six resulted in an increase in the gained output ratio (GOR) of almost twofold. Aly and El-Figi (2003) developed a steady-state mathematical model to study the performance of a FF-MED plant and found that the performance ratio depends significantly more on the number of effects than on the TBT. Ameri et al. (2009) studied the effect of design parameters on MED system specifications and found that the optimum performance depends on the optimum number of effects, which itself depends on seawater salinity, feedwater temperature, and temperature differences between effects.

Other authors have published models of MED plants that use renewable energy as the heat source for the unit. El-Nashar and Qamhiyeh (1990, 1995) and El-Nashar (2000) presented a mathematical simulation of the operation at transient and steady-state of a solar MED plant located in Abu Dhabi (United Arab Emirates). Empirical correlations of the heat transfer coefficients of the plant components were obtained from experimental data of the pilot MED plant. The model was able to predict the distillate production and specific heat consumption for each operating condition with reasonable accuracy. Leblanc et al. (2010) implemented the modelling of a pilot MED plant fed by hot water from a solar pond, using a Visual Basic–Excel environment. The model was used for plant design and the agreement between the experimental and simulation results was found to be good. Other authors, such as Wang et al. (2011), proved the feasibility of a system

consisting of a MED plant that uses geothermal energy as the heat source. The validation was proved with experimental data from a real plant. Yilmaz and Söylemez (2012) developed a model of a FF-MED plant using hybrid renewable energy sources (solar and wind). The model was implemented in a Visual Basic environment and has been used for simulations in a case study of a plant located in Turkey. Reddy et al. (2012) proposed a transient model of a MED plant coupled to flat plate collectors. This model was implemented in a MATLAB environment and was used to optimize the plant configuration by studying the effect of several design and operational parameters on its performance. Palenzuela et al. (2014) developed a steady-state model based on the design of a FF-MED pilot plant using low steam temperature coming from parabolic-trough solar collectors with increased energy efficiency, operating in Almeria (Spain). In 2005, the first effect of such a MED plant was exchanged for a cell working with hot water coupled to a solar field. The same authors (Palenzuela et al. 2013) obtained empirical correlations for the overall heat transfer coefficient of this effect. The model is described later in this chapter (Sect. 3.4).

3.3 Description of the Plant

The MED plant at the Plataforma Solar de Almería (MED-PSA, see Fig. 3.1) is a FF-MED unit manufactured and delivered by Entropie in 1987. It has 14 cells in a vertical arrangement, with decreasing pressures and temperatures from the first cell (on the top) to the fourteenth (Zarza 1991, 1994). Each cell is composed of an effect or evaporator and, in the case of FF-MED units, a preheater next to each effect (they are both horizontal tube bundles) to increase the seawater temperature while it is being pumped up to the first effect. The temperature rise is the result of the latent heat of condensation of part of the vapour generated in each effect. Thus, the seawater temperature reaching the first effect is close to the evaporation temperature. The MED-PSA has 13 preheaters, one for each cell except for the last cell, where there is a condenser that is much bigger than the other preheaters.

The first effect works with low-pressure saturated steam at a limit temperature of 70 °C (0.31 bar) to avoid scaling. This steam is provided by a parabolic-trough collector solar field.

The flow sheet of the process is shown in Fig. 3.2. The seawater is preheated and pumped to the first cell, where it is sprayed through a spraying tray and falls over the horizontal-tube bundle of the first effect. A film is built up that coats the surface of the tubes entirely. The low-pressure heating steam flows inside the tube bundle and releases its latent heat to sprayed feedwater, evaporating part of it. Vapour generated in the first effect flows to the preheater located next to it, through a wire mesh demister that removes the brine droplets. Here, part of the vapour condenses, transferring its latent heat to the seawater that is circulating inside the tube bundle of the preheater. The distillate generated in the preheater is part of the distillate

generated in the next effect, and the rest of the vapour (which has not been condensed) flows through inside the second effect tube bundle.

In the second effect, the vapour transfers its latent heat to the brine, now more concentrated in salts, that falls by gravity from the previous effect and is sprayed over the spraying tray of the second effect. The vapour that condenses is mixed with the distillate generated in the previous preheater, forming the first distillate of the process. The same process is repeated in the rest of effects, the vapour produced in the previous effect being the thermal energy source of the effect. In each effect, as in the first, part of the vapour generated is used to preheat the seawater that flows through the preheaters. In addition to the vapour formed by boiling seawater, a small portion is formed by flashing as the brine passes from one effect to another, because it is at a lower pressure than the equilibrium pressure. Finally, the vapour produced in the last effect is condensed in the final condenser, transferring the latent heat of evaporation to the seawater that passes through this tube bundle, thereby increasing its temperature. One part of this seawater is pumped to the first effect
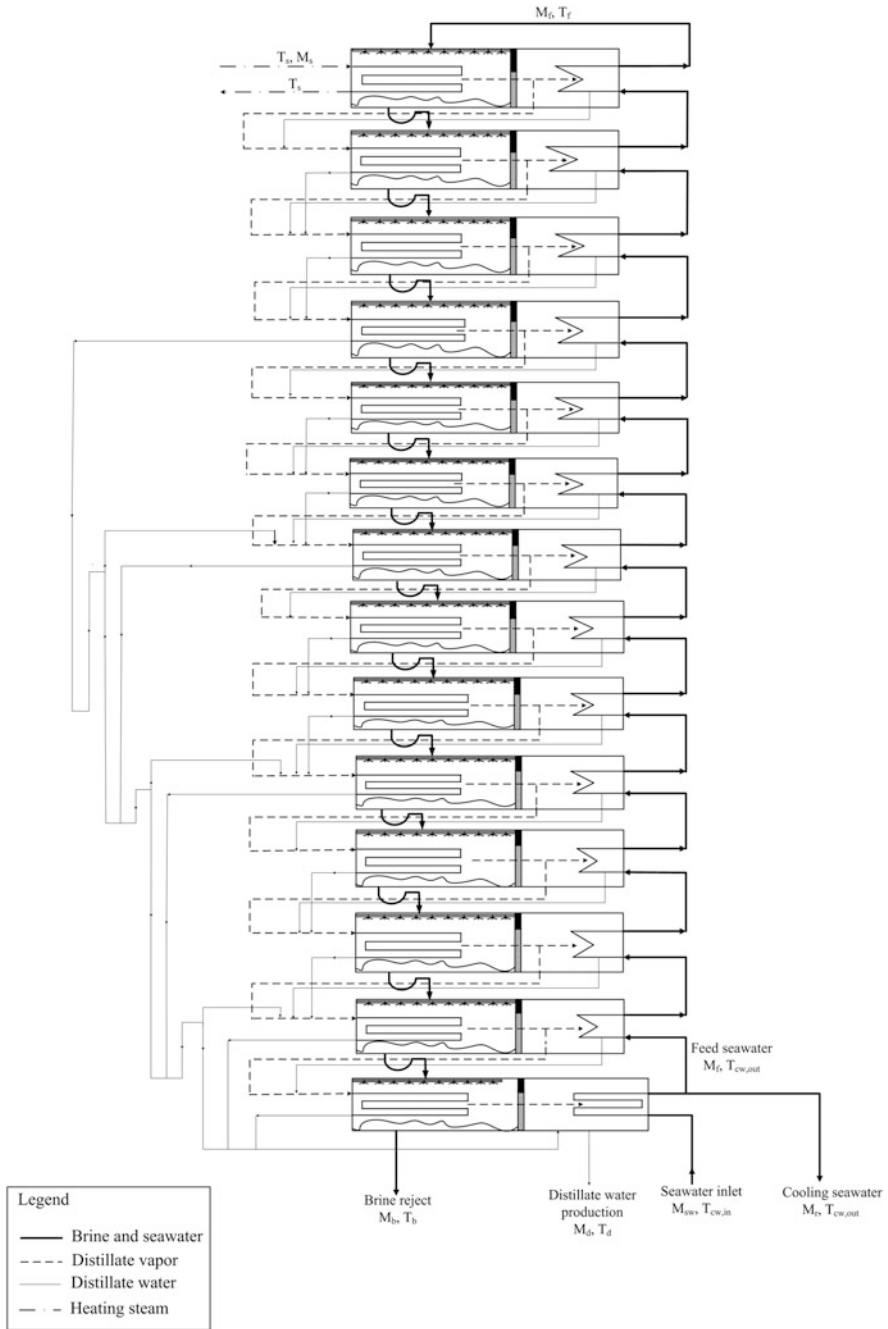
Fig. 3.2 Schematic of MED plant at the Plataforma Solar de Almería

(40 % in nominal conditions), passing through the preheaters, and the rest is rejected to the feed source.

The total plant distillate production consists of the vapour condensed in each effect and in the preheaters plus the distillate generated in the final condenser. As an energy optimisation strategy, the distillate produced goes to other effects instead of being extracted from each one. In some cases, it goes from one effect to the next, and in other cases, it goes to further effects as follows (see Fig. 3.2): In the fourth effect all the distillate is extracted, part of it goes to the seventh effect and the rest to the tenth. Similar extraction is made in the seventh effect, splitting the condensate extracted between the tenth and the thirteenth effects. Another extraction takes place at the tenth effect, part goes to the thirteenth effect and the rest is mixed with the distillate produced in the fourteenth effect. The final extraction is made in the thirteenth effect, after which all the distillate is mixed with that produced in the fourteenth effect. Finally, this accumulated distillate is mixed with the distillate produced in the condenser.

The vacuum system consists of two hydro-ejectors, which are connected to effects 2, 7 and the final condenser. They are connected within a closed circuit to a tank and an electric pump that circulates seawater through the ejectors at a pressure of 3 bar. This system makes the initial vacuum in the plant and also removes the air (lack of air tightness) and non-condensable gases during operation.

The design specifications for the MED-PSA plant are given in Table 3.1.

3.3.1   Experimental Setup

The MED-PSA plant is experimental and therefore it has an exhaustive monitoring system that provides instantaneous values of the measured data. The variables that are monitored are shown in Table 3.2 and also depicted in Fig. 3.2.

The supply water to the desalination plant is obtained from wells and stored in two interconnected pools (see Fig. 3.3) that are in a closed circuit with the desalination plant. The feedwater from the wells is stored in the big pool (see Fig. 3.3a), from where the cooling water is pumped to the tube bundle of the condenser. The feedwater pumped to the first effect is a fraction of this water. All the outlet streams of the plant (distillate, brine and rejected cooling seawater) enter the small pool (see Fig. 3.3b). The rejected cooling seawater is the fraction of water that circulates into the condenser tube bundle and is sent back to the pool without being pumped to the first effect. Therefore, part of the heat released at the condenser

Table 3.1 Design specifications for the MED-PSA plant

Number of effects	14
Feed seawater flow rate (m^3/h)	8
Total brine production (m^3/h)	5
Heating steam mass flow rate (kg/h)	300 kg/h
Total distillate production (m^3/h)	3
Cooling seawater flow rate 25 °C (m^3/h)	20
Vapour production in the last effect at 70 °C (kg/h)	159
Thermal energy consumption in the first effect (kW)	200
Performance ratio	>9
Heating steam temperature (°C)	70
Brine temperature in the first effect (°C)	68
Feed and cooling seawater temperature at the outlet of the condenser (°C)	33

Table 3.2 Monitored data at MED-PSA plant

Measurement	Variable	Magnitude
Flow rate	M_s	Heating steam flow in the first effect
	M_{cw}	Cooling seawater flow
	M_f	Feed seawater flow
	M_d	Product water flow
	M_b	Brine flow
Temperature	T_s	Heating steam inlet temperature
	T_f	First effect sprayed seawater temperature
	$T_{cw,in}$	Cooling seawater inlet temperature
	$T_{cw,out}$	Cooling seawater (rejected) outlet temperature
Pressure	$P_v(1), P_v(2), P_v(4), P_v(6), P_v(8),$ $P_v(10), P_v(12), P_v(14)$	1st, 2th, 4th, 6th, 8th, 10th, 12th, 14th effect vapour pressure
	P_{vc}	Vapour pressure in the condenser
Salt concentration:	X_f	Seawater total dissolved solids at the condenser inlet

goes into the pool and the cooling water temperature could increase during the experiment, which is not desirable. To avoid such an increase in cooling water temperature, there is an external circuit containing a refrigeration tower that cools the water in the small pool before it enters the big pool to be re-used in the MED process. However, sometimes the refrigeration tower is insufficient and it is difficult to maintain a long-term steady state in all its variables, even though the MED plant has control mechanisms at its inputs.

Because the TBT is always kept below 70 °C to avoid scaling, only two simple pretreatments are needed: (1) filtering of the water coming from the wells and the big pool and (2) chemical treatment using a solution based on a policarboxilic acid
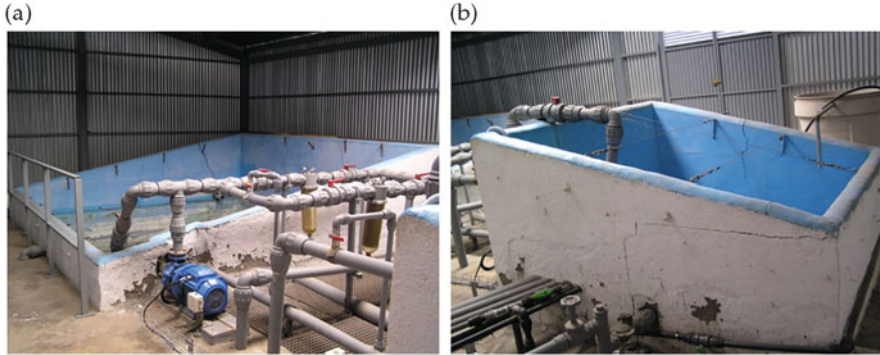
Fig. 3.3 Pools for (**a**) feedwater to the plant and (**b**) rejected streams from the plant

(Belgard EV2050). Cleaning of the plant is carried out once a year using sulphamic acid at 5 %.

3.4 Mathematical Model

MATLAB software was used as an environment for solving the mathematical model describing features of the MED-PSA plant. In order to simplify the model calculations, some assumptions were considered:

- Steady-state operation
- Distillate that passes from one effect to another leaves each effect at the subcooled region at a temperature 2 °C lower than the inlet temperature of the distillate at the inlet of the effect, after transferring its sensible heat to the feedwater
- Flashing of the distillate is not taken into consideration, except in the final condenser
- Thermodynamic loss is assumed to be 1 °C as a real design value, which includes 0.5 °C for non-equilibrium allowance (NEA)
- Two percent of the vapour generated in second and seventh effect, and in the final condenser, is extracted by the vacuum system
- Isothermal physical properties are considered for all cases

To develop the model, the MED system was divided into three components: the preheaters, the effects and the final condenser. Likewise, the effects of the MED system were considered in three different groups, which were modelled individually: the first effect (named group G1), the effects from 2 to N (named group G2) and the final condenser (named group G3). G2 was divided into three subgroups, namely, G2-1 for effects 2, 5, 8, 11 and 14; G2-2 for effects 3, 4, 6, 9 and 12; and G2-3 for effects 7, 10 and 13. Physical properties of water were calculated using a REFPROP dynamic library (NIST 2007) within the MATLAB environment.

Fig. 3.4 Flow diagram of a typical preheater (#*i*)
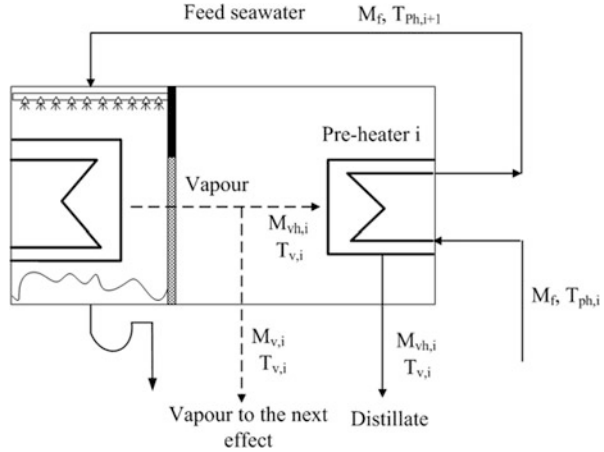
3.4.1 Preheaters

In each preheater, some of the vapour from the effect ($M_{vh,i}$, $T_{v,i}$) condenses and the heat released is used to heat the seawater from $T_{ph,i}$ to $T_{ph,i+1}$. Figure 3.4 shows the flow diagram for a typical preheater (#*i*), presenting the relevant variables that characterize the preheater's inlet and outlet streams. The equations for all preheaters are mathematically similar.

The energy balance and the heat transfer rate for the preheaters are calculated as follows (descriptions of all symbols are given at the beginning of the chapter):

- *Energy balance*: The latent heat that is released in the condensation process is used to heat the seawater flowing through the tube bundle of the preheater.

$$M_{vh,i}\lambda_{vh,i} = M_f C_p\left(T_{ph,i+1} - T_{ph,i}\right) \tag{3.1}$$

- *Heat transfer equation*: The log mean temperature difference (LTMD$_{ph}$) method is used for the heat transfer rate (El-Sayed and Silver 1980).

$$Q_{ph,i} = A_{ph,i}U_{ph,i}\text{LTMD}_{ph,i} = M_f C_p\left(T_{ph,i+1} - T_{ph,i}\right) \tag{3.2}$$

where:

$$\text{LTMD}_{ph,i} = \frac{\left(T_{v,i} - T_{ph,i+1}\right) - \left(T_{v,i} - T_{ph,i}\right)}{\ln\left(\frac{T_{v,i}-T_{ph,i+1}}{T_{v,i}-T_{ph,i}}\right)} \tag{3.3}$$

The overall heat transfer coefficient ($U_{ph,i}$) is calculated using the following correlation from El-Dessouky and Ettouney (2002):

$$U_{\mathrm{ph},i} = 1.7194 + 3.2063 \cdot 10^{-3}T_{\mathrm{v},i} + 1.5971 \cdot 10^{-5}T_{\mathrm{v},i}{}^2 - 1.9918$$
$$\cdot\, 10^{-7}T_{\mathrm{v},i}{}^3 \tag{3.4}$$

3.4.2 Effects

First Effect (G1)

Feedwater (with parameters M_f, T_f, X_f) is sprayed into the effect over a series of tubes. On the other hand, low pressure steam (M_s, T_s) flows inside the tubes, transferring its latent heat to the feedwater, and part of it is evaporated by boiling ($M_{\mathrm{gb},1}$, $T_{\mathrm{v},1}$). This vapour flows to the inside of the tubes of the next effect, acting as the heat transfer source for this effect. The un-evaporated feedwater ($M_{\mathrm{b},1}$, $T_{\mathrm{b},1}$) leaves the effect more concentrated in salts ($X_{\mathrm{b},1}$) and falls by gravity on the next effect. Figure 3.5 shows the flow diagram for the first effect.

The mass, salt and energy balances, and the heat transfer equation are shown below:

- *Mass balance*:

$$M_f = M_{\mathrm{gb},1} + M_{\mathrm{b},1} \tag{3.5}$$

- *Salt balance*: The salinity of the brine stream leaving the effect can be found through a salt balance in which it is assumed that the vapour formed by boiling is pure:

$$X_f M_f = X_{\mathrm{b},1} M_{\mathrm{b},1} \tag{3.6}$$

- *Energy balance*: The latent heat that is released during condensation of the low pressure steam is used to heat the feed to boiling point and then evaporate part of it:

Fig. 3.5 Flow diagram of the first effect
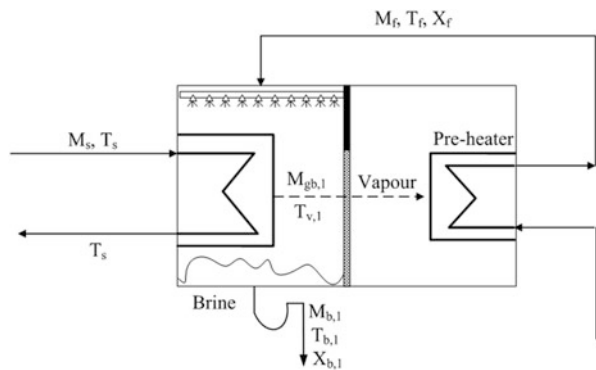
$$M_{gb,1}\lambda_{gb,1} = M_s\lambda_s - M_f C_p(T_{b,1} - T_f) \tag{3.7}$$

- *Heat transfer equation*: The heat transfer rate (Q_s) is equal to the change in enthalpy associated with the condensation of the vapour (λ_s). Because the difference between T_f and $T_{b,1}$ is very small, the driving force is considered to be the difference between the condensation temperature of the steam, T_s, and the boiling temperature of the seawater, $T_{b,1}$:

$$Q_s = U_{eff,1} \cdot A_{eff,1} \cdot (T_s - T_{b,1}) = M_s\lambda_s \tag{3.8}$$

The overall heat transfer coefficient ($U_{eff,1}$) is calculated using the following correlation from El-Dessouky and Ettouney (2002):

$$U_{eff,1} = 1.9695 + 1.2057 \times 10^{-2} \cdot T_{b,1} - 8.5989 \times 10^{-5} \cdot T_{b,1}^2 + 2.5651$$
$$\times 10^{-7} \cdot T_{b,1}^3 \tag{3.9}$$

In the first effect, no distillate is produced from the condensation of vapour generated in the boiling process. In the first effect, the heat source is external (low-pressure saturated steam provided by a parabolic-trough solar collector field) and therefore the distillate produced by its condensation is not taken into account as part of the distillate production of the plant. Therefore:

$$M_d(1) = 0 \tag{3.10}$$

Also, in this effect the feedwater enters at a temperature that is below that of saturation (subcooled), so no vapour is generated by flashing:

$$M_{gf}(1) = 0 \tag{3.11}$$

Effects from 2 to N (Group G2)

The mass, salt and energy balances corresponding to the flashing process for the G2 group are mathematically similar for all the effects. The equations for mass balance, heating source and heat transfer in the tube bundle are also mathematically similar for all the effects of G2. Therefore, all these equations are common to all subgroups of G2. Only the energy balance in the tube bundle and the distillate produced in the effect, as well as its temperature, are analysed for each subgroup of G2 (G2-1, G2-2 and G2-3) and are shown below.

Subgroup G2-1

Brine from the previous effect ($M_{b,i-1}$, $T_{b,i-1}$, $X_{b,i-1}$) enters at a higher temperature than corresponding to the equilibrium temperature at the pressure of this effect.
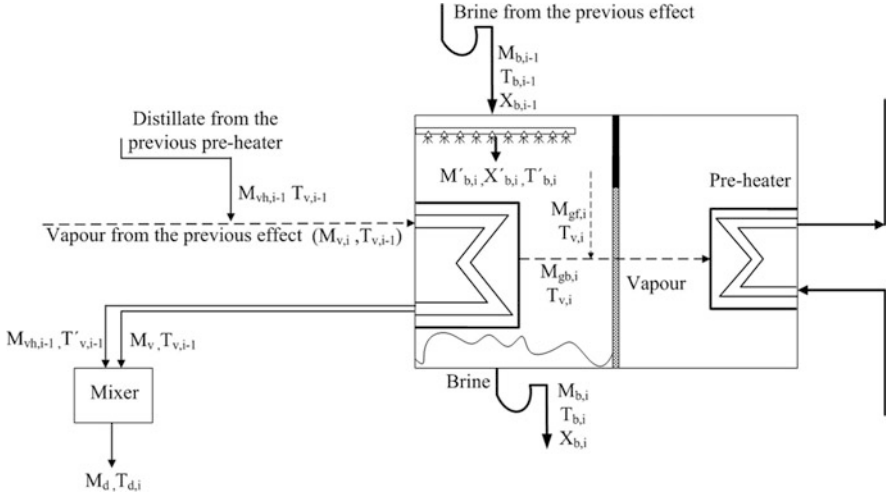
Fig. 3.6 Flow diagram of the subgroup G2-1

A portion of the brine is evaporated by flash ($M_{gf,i}$, $T_{v,i}$) because the effect is at a lower pressure. The un-evaporated brine after the flashing process ($M'_{b,i}$, $T'_{b,i}$, $X'_{b,i}$) is sprayed over a series of tubes. Vapour from the previous effect ($M_{v,i}$, $T_{v,i-1}$) transfers its latent heat ($\lambda_{v,i-1}$) to the brine, evaporating part of it by a boiling process ($M_{gb,i}$, $T_{v,i}$). The resulting vapour from the effect ($M_{gb,i} + M_{gf,i} - M_{vh,i}$, $T_{v,i}$) flows to the next effect as the heat transfer source. The resulting un-evaporated brine ($M_{b,i}$, $T_{b,i}$) leaves the effect more concentrated in salts ($X_{b,i}$) and falls by gravity on the next effect. The distillate generated in the previous preheater as saturated liquid ($M_{vh,i-1}$, $T_{v,i-1}$), enters the effect and transfer its sensible heat to the brine; thus, the distillate leaves the effect as subcooled liquid ($M_{vh,i-1}$, $T'_{v,i-1}$). Figure 3.6 shows a flow diagram of one effect of the subgroup G2-1.

- *Energy balance*:

$$M_{gb,i}\lambda_{gb,i} = M_{v,i}\lambda_{v,i-1} + M'_{b,i}C_p\left(T'_{b,i} - T_{b,i}\right)$$
$$+ M_{vh,i-1}C_p\left(T_{v,i-1} - T'_{v,i-1}\right) \qquad (3.12)$$

- *Distillate produced*: The distillate leaving the effect is the sum of the vapour condensed from the previous effect and the distillate from the previous preheater:

$$M_{d,i} = M_{v,i} + M_{vh,i-1} \qquad (3.13)$$

The temperature at which the distillate leaves the effect ($T_{d,i}$) is determined by the energy balance in the mixer:
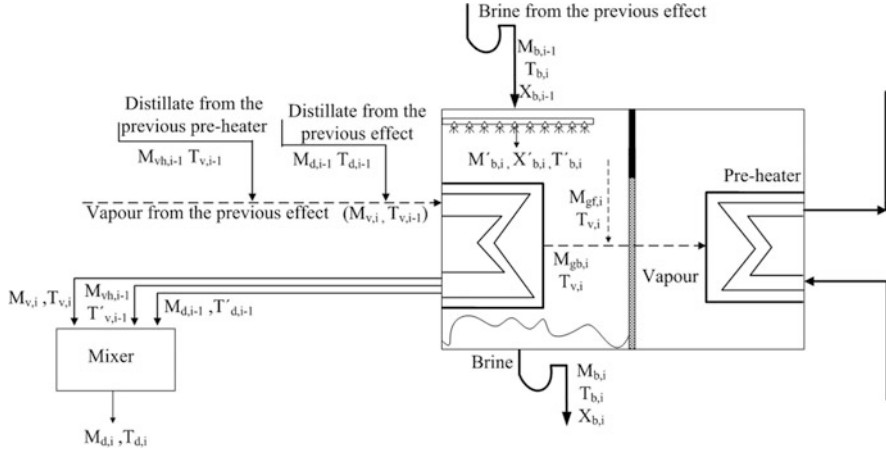
Fig. 3.7 Flow diagram of subgroup G2-2

$$M_{v,i}C_pT_{v,i-1} + M_{vh,i-1}C_pT'_{v,i-1} = M_{d,i}C_pT_{d,i} \tag{3.14}$$

Subgroup G2-2

The processes taking place in G2-2 are the same as for the previous group, but in this case distillate entering the tube bundle of each effect is taken into account. It is the distillate generated in the previous effect as saturated liquid ($M_{d,i-1}$, $T_{d,i-1}$) that enters the effect and transfer its sensible heat to the brine, leaving the effect as subcooled liquid ($M_{d,i}$, $T'_{d,i-1}$). The scheme in Fig. 3.7 shows the effect's inlet and outlet streams for this subgroup.

- *Energy balance*:

$$M_{gb,i}\lambda_{gb,i} = M_{v,i}\lambda_{v,i-1} + M'_{b,i}C_p\left(T'_{b,i} - T_{b,i}\right)$$
$$+ M_{vh,i-1}C_p\left(T_{v,i-1} - T'_{v,i-1}\right) + M_{d,i-1}C_p\left(T_{d,i-1} - T'_{d,i-1}\right) \tag{3.15}$$

- *Distillate produced*: The distillate coming from the previous effect ($M_{d,i-1}$) joins the vapour condensed from the previous effect ($M_{v,i}$) and the distillate from the previous preheater ($M_{vh,i-1}$):

$$M_{d,i} = M_{v,i} + M_{vh,i-1} + M_{d,i-1} \tag{3.16}$$

The energy balance determining the temperature at which the distillate leaves the mixer ($T_{d,i}$) is given by:
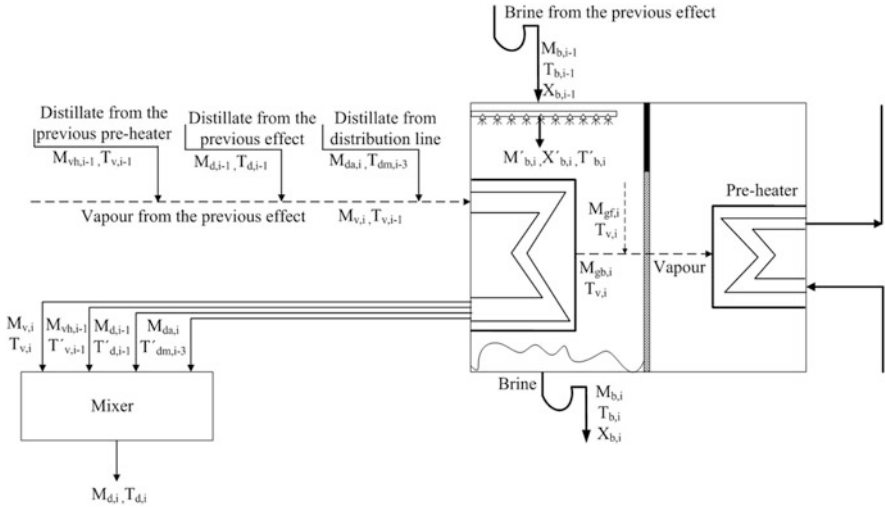
Fig. 3.8 Flow diagram of subgroup G2-3

$$M_{v,i}C_pT_{v,i-1} + M_{vh,i-1}C_pT'_{v,i-1} + M_{d,i-1}C_pT'_{d,i-1} = M_{d,i}C_pT_{d,i} \qquad (3.17)$$

Subgroup G2-3

In these effects (see Fig. 3.2), another heat source is added to the processes mentioned in the previous groups. The heat source corresponds to the portion of distillate that leaves effect 4 (and enters effect 7), effect 7 (and enters the effect 10) and effect 10 (an enters the effect 13). In each case, the portion of distillate as saturated liquid ($M_{da,i}$, $T_{dm,i-3}$) enters the effect and transfer its sensible heat to the brine, leaving the effect as subcooled liquid ($M_{da,i}$, $T'_{dm,i-3}$). The flow diagram of a representative effect of this group, showing the inlet and outlet streams, is presented in Fig. 3.8.

- *Energy balance*:

$$
\begin{aligned}
M_{gb,i}\lambda_{gb,i} = M_{v,i}\lambda_{v,i-1} &+ M'_{b,i}C_p\left(T'_{b,i} - T_{b,i}\right) + M_{vh,i-1}C_p\left(T_{v,i-1} - T'_{v,i-1}\right) \\
&+ M_{d,i-1}C_p\left(T_{d,i-1} - T'_{d,i-1}\right) + M_{da,i}C_p\left(T_{dm,i-3} - T'_{dm,i-3}\right)
\end{aligned}
\qquad (3.18)
$$

- *Distillate produced*: Taking into account the additional distillate coming from further effects ($M_{da,i}$), the distillate produced from these effects is given by the following equation:
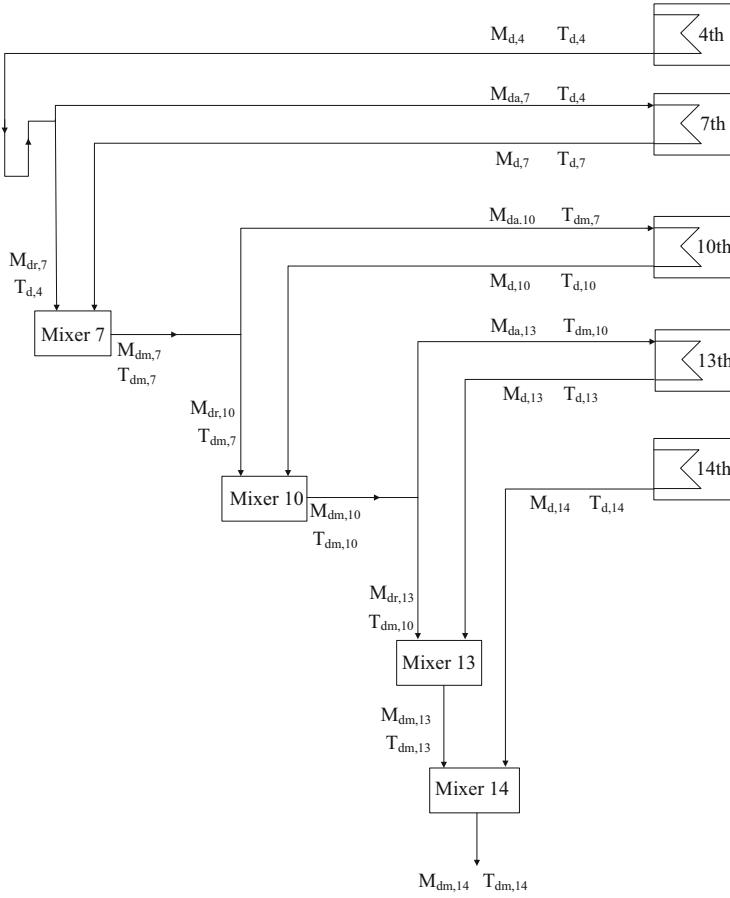
Fig. 3.9 Flow diagram of the distillate distribution system

$$M_{d,i} = M_{v,i} + M_{vh,i-1} + M_{d,i-1} + M_{da,i} \qquad (3.19)$$

The temperature at which the total distillate leaves the mixer ($T_{d,i}$) is determined from the following energy balance:

$$M_{v,i}C_pT_{v,i-1} + M_{vh,i-1}C_pT'_{v,i-1} + M_{d,i-1}C_pT'_{d,i-1} + M_{da,i}C_pT'_{dm,i-3} = M_{d,i}C_pT_{d,i} \qquad (3.20)$$

On the other hand, as an energy optimisation strategy, the MED-PSA plant has a special distillate distribution, as shown in Fig. 3.9. Energy and mass balances through the mixers are shown below:

- *Mass balance (for mixers 7, 10 and 13):*

$$M_{dm,i} = M_{dr,i} + M_{d,i} \tag{3.21}$$

$$M_{dr,i-3} = 0 \quad \text{for Mixer 7} \tag{3.22}$$

$$M_{dr,i} = M_{d,i-3} + M_{dr,i-3} - M_{da,i} \tag{3.23}$$

- *Mass balance (for mixer 14)*:

$$M_{dm,14} = M_{dm,14-1} + M_{d,14} \tag{3.24}$$

- *Energy balance (for mixers 7, 10, 13)*:

$$M_{dr,i}C_pT_{dm,i-3} + M_{d,i}C_pT_{d,i} = M_{dm,i}C_pT_{dm,i} \tag{3.25}$$

$$T_{dm,i-3} = T_{d,i-3} \quad \text{for Mixer 7} \tag{3.26}$$

- *Energy balance for mixer 14*:

$$M_{dm,i-1}C_pT_{dm,i-1} + M_{d,i}C_pT_{d,i} = M_{dm,i}C_pT_{dm,i} \tag{3.27}$$

The mass, salt and energy balances corresponding to the flashing process occurring in all G2 group effects are shown below:

- *Mass balance*: As mentioned before, part of the brine flashes ($M_{gf,i}$) as it enters the effect and the rest ($M'_{b,i}$) is sprayed over the tube bundle:

$$M_{b,i} = M_{gf,i} + M'_{b,i} \tag{3.28}$$

- *Salt balance*: As in all the cases, the vapour formed is assumed to be pure:

$$X_{b,i-1}M_{b,i-1} = X'_{b,i}M'_{b,i} \tag{3.29}$$

- *Energy balance*: The brine coming from the previous effect enters each effect at a higher temperature than that corresponding to the equilibrium temperature at the pressure of this effect. As a result, it flashes and generates steam at the vapour temperature in the effect ($T_{v,i}$); subsequently, the temperature of the un-evaporated water decreases from T_{b-1} to $T'_{b,i}$:

$$M_{gf,i}\lambda_{gf,i} = M_{b,i-1}C_p\left(T_{b,i-1} - T'_{b,i}\right) \tag{3.30}$$

The temperature of the un-evaporated brine ($T'_{b,i}$) is higher than the vapour temperature ($T_{v,i}$) by the non-equilibrium allowance (NEA), which is a measure of the flashing process (El-Dessouky, 2002):

$$T'_{b,i} = T_{v,i} + \text{NEA}_i \tag{3.31}$$

The equations of the mass balance, heating source and the heat transfer equation taking place in the tube bundle are as follows:

- *Mass balance*: In this case, part of the un-evaporated brine after the flashing process is evaporated ($M_{gb,i}$) and the rest ($M_{b,i}$) leaves the effect more concentrated in salts:

$$M'_{b,i} = M_{gb,i} + M_{b,i} \tag{3.32}$$

- *Salt balance*:

$$X'_{b,i} M'_{b,i} = X_{b,i} M_{b,i} \tag{3.33}$$

- *Heat transfer equation*: In each effect, the vapour coming from the previous effect condenses completely while evaporating by boiling the brine sprayed over the tubes. The heat transfer rate ($Q_{eff,i}$) is equal to the change in enthalpy associated with the condensation of the vapour ($\lambda_{v,i-1}$):

$$Q_{eff,i} = U_{eff,i} A_{eff,i} (T_{v,i-1} - T_{b,i}) = M_{v,i} \lambda_{v,i-1} \tag{3.34}$$

Equation (3.8) is used to calculate the overall heat transfer coefficient ($U_{eff,i}$) for all the effects.

The heating source in each effect consists of the total vapour generated by boiling ($M_{gb,i-1}$) and flashing ($M_{gf,i-1}$) minus the vapour consumed in the preheater ($M_{vh,i-1}$), as shown in the following equation:

$$M_{v,i} = M_{gb,i-1} + M_{gf,i-1} - M_{vh,i-1} \tag{3.35}$$

Final Condenser

Vapour from the last effect ($M_{gb,N}$, $M_{gf,N}$, $T_{v,N}$) is condensed in the condenser. Typically, excess seawater (M_{sw}, $T_{cw,in}$) is required to meet the required cooling load. Excess seawater is used for cooling purposes and only the required feedwater (M_f, $T_{cw,out}$) is used for the process and is sent to the first preheater. The rest (M_r, $T_{cw,out}$) is returned back to the source. On the other hand, the distillate resulting from mixer 14 ($M_{dm,N}$, $T_{dm,N}$) enters the condenser and part of it flashes (M_{df}, T_{vc}) because the condenser is at a lower pressure.

Figure 3.10 shows a scheme of the final condenser, representing the inlet and outlet streams.

The energy and mass balance with regards to the flashing process are as follows:
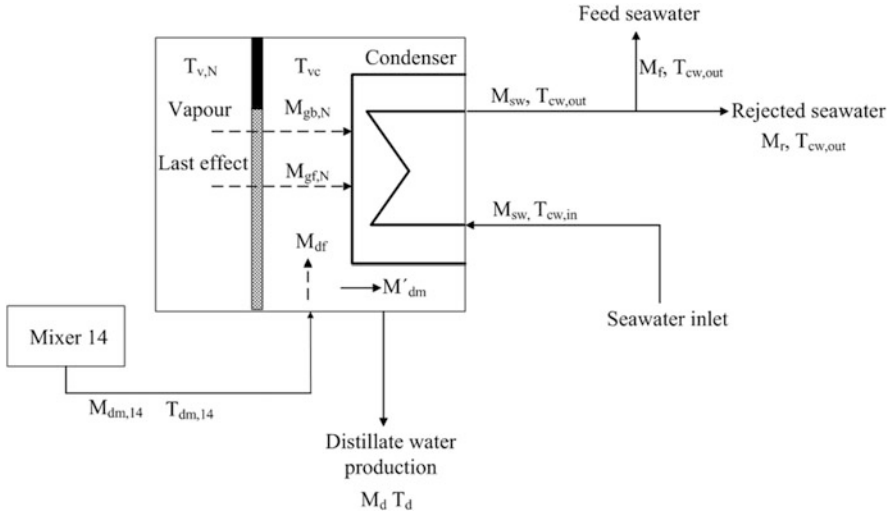
Fig. 3.10 Flow diagram of the final condenser

$$M_{df}\lambda_{df} = M_{dm,N}C_p(T_{dm,N} - T_{vc}) \tag{3.36}$$

$$M_{dm,N} = M'_{dm,N} + M_{df} \tag{3.37}$$

The energy, mass balance and heat transfer equations for the condenser tube bundle are similar to those for the preheaters:

- *Energy balance*:

$$M_{sw}C_p(T_{cw,out} - T_{cw,in}) = (M_{gb,N} + M_{gf,N} + M_{df})\lambda_{vc} \tag{3.38}$$

- *Mass balance*:

$$M_d = M_{gb,N} + M_{gf,N} + M_{dm,14} \tag{3.39}$$

- *Heat transfer equation*:

$$Q_c = A_c \cdot U_c \cdot LTMD_c = M_{sw}C_p(T_{cw,out} - T_{cw,in}) \tag{3.40}$$

where:

$$LTMD_c = \frac{(T_{v,N} - T_{cw,in}) - (T_{v,N} - T_{cw,out})}{\ln\left(\frac{T_{v,N}-T_{cw,in}}{T_{v,N}-T_{cw,out}}\right)} \tag{3.41}$$

The overall heat transfer coefficient (U_c) is calculated using (3.4):

3.5   Running and Validation of the Model

A total of 44 equations are needed to run the model. There are 11 input variables of the model (known variables), consisting of design and operating parameters. The design parameters are the number of effects (N) and the number of preheaters (N_{ph}). Operating parameters are the feedwater mass flow rate spraying over the first tube bundle and its temperature and salt concentration (M_f, T_f, X_f), the heating steam mass flow rate entering the first tube bundle and its temperature (M_s, T_s), the inlet and outlet seawater temperature ($T_{cw,in}$, $T_{cw,out}$), and the vapour and brine temperature in each effect ($T_{v,i}$, $T_{b,i}$). The values of all these variables are specified in Tables 3.3 and 3.4 and are average values of the experimental data. The unknown variables, which are calculated from the simulation run (output variables), are the distillate flow rate formed in the preheaters ($M_{vh,i}$) and in the effects ($M_{v,i}$); the total

Table 3.3 Input variables data

Input variable	Symbol	Value
Feedwater mass flow rate (kg/h)	M_f	8000
Number of effects	N	14
Number of preheaters	N_{ph}	13
Heating steam mass flow rate (kg/h)	M_s	295.92
Heating steam temperature (°C)	T_s	70.8
Feedwater temperature in the first effect (°C)	T_f	66.3
Feedwater salt concentration (g/kg)	X_f	35
Seawater inlet temperature in the condenser (°C)	$T_{cw,in}$	25
Seawater outlet temperature in the condenser (°C)	$T_{cw,out}$	32.3

Table 3.4 Input variables data

Effect	Temperature (°C)	
	Vapour, $T_{v,i}$	Brine, $T_{b,i}$
1	68.0	69.0
2	65.2	66.2
3	62.5	63.5
4	59.8	60.8
5	57.1	58.1
6	54.5	55.5
7	51.8	52.8
8	49.2	50.2
9	46.8	47.8
10	44.2	45.2
11	41.8	42.8
12	39.5	40.5
13	37.1	38.1
14	35.0	36.0

distillate leaving the effects ($M_{d,i}$); the distillate flow rates in the special distribution ($M_{dr,i}$, $M_{dm,i}$, $M_{da,i}$) and their respective temperatures ($T'_{v,i-1}$, $T_{d,i}$, $T'_{d,i-1}$, $T_{dm,i}$, $T_{dm,i-3}$, $T'_{dm,i-3}$); the brine mass flow rates being sprayed in each effect ($M_{b,i-1}$) and mass flow rate of the remaining brine after the flashing process ($M'_{b,i}$), its temperature ($T'_{b,i}$) and its salt concentration ($X'_{b,i}$); the brine leaving each effect ($M_{b,i}$) and its salt concentration ($X_{b,i}$); the sum of the vapour generated by boiling and flashing ($M_{fv,i}$); the seawater inlet mass flow rate in the condenser (M_{sw}); the heat transfer rate in the preheaters ($Q_{ph,i}$), in the effects (Q_s, $Q_{eff,i}$) and in the condenser (Q_c); the overall heat transfer coefficient for the preheater ($U_{ph,i}$), for the effects ($U_{eff,i}$) and for the condenser (U_c); the total distillate water production (M_d); the *GOR*, the recovery ratio (*RR*) which is the ratio of the distillate product flow rate to the feed flow rate supplied; the specific area (*sA*) which is defined as the ratio of the total heat transfer area (for effects, preheaters and final condenser) to the distillate production; and the heat transfer areas (effects, $A_{eff,i}$, preheaters, $A_{ph,i}$, condenser, A_c).

Validation of the model was carried out by comparing experimental data of the MED-PSA plant with results obtained from the simulation runs of the mathematical model. The variables compared were the sum of the vapour generated by boiling and flashing (M_{fv}), the brine leaving each effect (M_b), the total distillate water production (M_d), the seawater inlet mass flow rate in the condenser (M_{sw}), the GOR, the RR and the heat transfer areas (effects, A_{eff}, preheaters, A_{ph}, condenser, A_c).

3.6 Results and Discussion

The results are shown in Tables 3.5 and 3.6 and in Figs. 3.11 and 3.12. Figures 3.11 and 3.12 show a graphic comparison of the values obtained for the generated vapour by boiling and flash (M_{fv}) and for the brine leaving each effect (M_b). As seen, the model results fit quite well with experimental results, especially for the brine leaving each effect, where the difference between them is minimal. Comparing M_{fv} values (Fig. 3.11), the slight increase in the difference between actual and model values could be the result of certain assumptions taken in order to simulate the special distillate distribution.

Table 3.5 shows a numerical comparison of the variables M_{fv} and M_b. Table 3.6 shows a comparison between the total distillate water production, the seawater inlet mass flow rate in the condenser, the GOR, the RR and the heat transfer areas of the effects (A_{eff}), preheaters (A_{ph}) and condenser (A_c). The relative error for predicting all these variables was determined, and ranged between 1 and 9 %, which means that the model results fit quite well with results from the experiments. The maximum error corresponds to the mass flow rate in the condenser (see Table 3.6). This could be a result of the fact that this mass flow rate is not kept constant during each experiment, because the plant does not operate near to the sea. Seawater is simulated in large stores (pools) that feed the plant. As a consequence, the temperature of the seawater entering the condenser tube bundle ($T_{cw,in}$) can increase during the

Table 3.5 Comparison between model and experimental values of the accumulated vapor and brine mass flow rate in each effect

Effect	Accumulated vapor mass flow rate (kg/h)		Brine mass flow rate (kg/h)	
	Actual	Model	Actual	Model
1	257	256.5	7743	7735
2	248	249.0	7495	7486
3	244	246.2	7251	7241
4	239	243.4	7012	6997
5	233	238.0	6779	6760
6	224	231.7	6555	6528
7	224	223.7	6331	6305
8	216	214.2	6115	6091
9	202	204.0	5913	5887
10	208	202.3	5705	5686
11	190	191.0	5515	5495
12	172	180.1	5343	5315
13	178	176.7	5165	5139
14	159	159.3	5006	4981

Table 3.6 Comparison between model and experimental values of the total distillate water production, seawater inlet mass flow rate in the condenser, the gain output ratio, recovery ratio and heat transfer areas of the effects, preheaters and condenser

Parameters	Model	Actual
M_d (kg/h)	3003	2984
M_{sw} (kg/h)	15848	14558
GOR	10.2	9.7
RR	37.6	37.5
A_{eff} (m^2)	33.6	26.3
A_{ph} (m^2)	4.1	5.0
A_c (m^2)	13.1	18.3

Fig. 3.11 Comparison between model and actual values for the accumulated vapour generated by boiling and flashing processes (M_{fv})
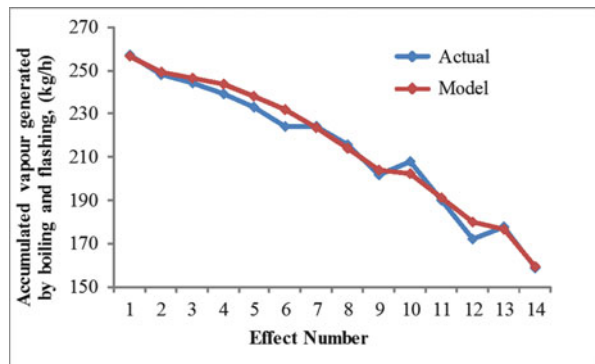
Fig. 3.12 Comparison between model and actual values for the brine mass flow rate leaving each effect (M_b)
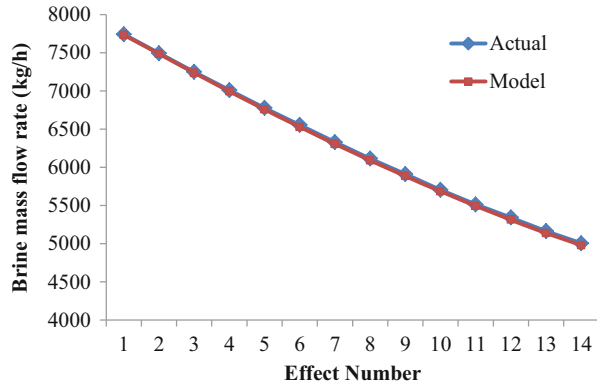
experiment. When this happens, the mass flow rate in the condenser is increased to keep the vapour temperature on the inside constant. This also results in a larger difference between the model and experimental values of the heat transfer area of the condenser. On the other hand, Table 3.6 also shows that the heat transfer areas of the effects and preheaters resulting from the model do not match those of the pilot plant. This is because the plant has the same fixed areas whereas in the model there is no such restriction. The heat transfer areas shown from the calculation are average values for all the effects and preheaters.

References

Aly, N. H., & El-Figi, A. K. (2003). Thermal performance of seawater desalination systems. *Desalination, 158*, 127–142.

Ameri, M., Mohammadi, S. S., Hosseini, M., & Seifi, M. (2009). Effect of design parameters on multi-effect desalination system specifications. *Desalination, 245*, 266–283.

Darwish, M. A., & Abdulraheim, H. K. (2008). Feed water arrangements in a multi-effect desalting system. *Desalination, 228*, 30–54.

Darwish, M. A., Al-Juwayhel, F., & Abdulraheim, H. K. (2006). Multi-effect boiling systems from an energy viewpoint. *Desalination, 194*, 22–39.

Druetta, P., Aguirre, P., & Mussati, S. (2013). Optimization of multi-effect evaporation desalination plants. *Desalination, 311*, 1–15.

El-Allawy M. (2003, 28 Sept–3 Oct). Predictive simulation of the performance of MED/TVC desalination distiller. In: *Proceedings IDA World Congress, Bahamas*. International Desalination Association: Topsfield, MA.

El-Dessouky, H. T., & Ettouney, H. M. (1999). Multiple-effect evaporation desalination systems: Thermal analysis. *Desalination, 125*, 259–276.

El-Dessouky, H., & Ettouney, H. (2002). *Fundamentals of salt water desalination* (1st ed.). Amsterdam, The Netherlands: Elsevier Science.

El-Dessouky, H., Alatiqi, I., Bingulac, S., & Ettouney, H. (1998). Steady-state analysis of the multiple effect evaporation desalination process. *Chemical Engineering and Technology, 21*, 437–451.

El-Nashar, A. M. (2000). Predicting part load performance of small MED evaporators – A simple simulation program and its experimental verification. *Desalination, 130*, 217–234.

El-Nashar, A. M., & Qamhiyeh, A. (1990). Simulation of the performance of MES evaporators under unsteady state operating conditions. *Desalination, 79*, 83.

El-Nashar, A. M., & Qamhiyeh, A. A. (1995). Simulation of the steady-state operation of a multi-effect stack seawater distillation plant. *Desalination, 101*, 231–243.

El-Sayed, Y. M., & Silver, R. S. (1980). *Principles of desalination: Vol. A* (2nd ed.). New York: Academic.

Gautami, G., & Khanam, S. (2012). Selection of optimum configuration for multiple effect evaporator system. *Desalination, 288*, 16–23.

Jyoti, G., & Khanam, S. (2014). Simulation of heat integrated multiple effect evaporator system. *International Journal of Thermal Sciences, 76*, 110–117.

Leblanc, J., Andrews, J., & Akbarzadeh, A. (2010). Low-temperature solar-thermal multi-effect evaporation desalination systems. *International Journal of Energy Research, 34*, 393–403.

NIST. (2007). NIST reference fluid thermodynamic and transport properties database (REFPROP) version 8.0 software. National Institute of Standards and Technology, Gaithersburg, MD

Palenzuela, P., Alarcón, D., Zaragoza, G., Blanco, J., & Ibarra, M. (2013). Parametric equations of the variables of a steady-state model of a multi-effect distillation plant. *Desalination and Water Treatment, 51*, 1229–1241.

Palenzuela, P., Hassan, A. S., Zaragoza, G., & Alarcón-Padilla, D. C. (2014). Steady state model for multi-effect distillation case study: Plataforma Solar de Almería MED pilot plant. *Desalination, 337*, 31–42.

Piacentino, A., & Cardona, E. (2010). Advanced energetics of a multiple-effects-evaporation (MEE) desalination plant. Part II: Potential of the cost formation process and prospects for energy saving by process integration. *Desalination, 259*, 44–52.

Reddy, K. S., Kumar, K. R., O'Donovan, T. S., & Mallick, T. K. (2012). Performance analysis of an evacuated multi-stage solar water desalination system. *Desalination, 288*, 80–92.

Wang, X., Christ, C., Regenauer-Lieb, K., Hooman, K., & Chua, H. T. (2011). Low grade heat driven multi-effect distillation technology. *International Journal of Heat and Mass Transfer, 54*, 5497–5503.

Yilmaz, İ. H., & Söylemez, M. S. (2012). Design and computer simulation on multi-effect evaporation seawater desalination system using hybrid renewable energy sources in Turkey. *Desalination, 291*, 23–40.

Zarza, E. (1991). *Solar thermal desalination project, first phase results and second phase description* (1st ed.). Madrid, Spain: CIEMAT.

Zarza, E. (1994). *Solar thermal desalination project: Phase II results and final project report*. Madrid, Spain: Secretaría General Técnica del CIEMAT, PSA/CIEMAT.

Zhao, D., Xue, J., Li, S., Sun, H., & Zhang, Q. (2011). Theoretical analyses of thermal and economical aspects of multi-effect distillation desalination dealing with high-salinity waste-water. *Desalination, 273*, 292–298.

Chapter 4
Steady-State Modelling of a Parabolic-Trough Concentrating Solar Power Plant

Nomenclature

Variables

A_{abs}	Absorber tube area (m^2)
A_c	Aperture area of the collector's reflective surface (m^2)
A_T	Total collector area required for the solar field (m^2)
C_p	Specific heat (kJ/kg °C)
DCA	Drain cooler approach (°C)
d_i	Inlet diameter of the absorber tube (m)
DNI	Direct normal irradiance (W/m^2)
d_o	Outlet diameter of the metallic tube (m)
E_{th}	Thermal energy required by the process (kWh)
$E_{th,stored}$	Stored thermal energy (kWh)
$E_{th,row}$	Thermal energy supplying a collector row (kWh)
F_{cond}	Refrigeration water flow rate in the power plant condenser (m^3/h)
F_e	Collector foiling factor
F_w	Specific fresh or seawater flow rate (m^3/MW_eh)
GOR	Gain output ratio
h	Specific enthalpy of the steam and liquid in the power cycle (kJ/kg)
h_f	Specific enthalpy of the steam in its final state in the thermodynamic cycle (kJ/kg)
h_i	Specific enthalpy of the steam in its initial state in the power cycle (kJ/kg)
h_{in}	Specific enthalpy of the working fluid at the collector inlet (kJ/kg)

h_{out}	Specific enthalpy of the working fluid at the collector outlet (kJ/kg)
K	Incidence angle modifier
L	Absorber tube length (m)
$\dot{m}$	Mass flow rate of the steam and liquid in the power cycle (kg/s)
$\dot{m}_{fluid}$	Mass flow rate of the oil inside the collector (kg/s)
$\hat{n}$	Normal aperture vector plane in a parabolic-trough collector
N_C	Number of collectors
N_F	Number of rows
N_T	Total number of collectors in the solar field
P	Steam and water pressure in the power cycle (bar or kPa)
P_c	Thermal power dissipated in the condenser (kW_{th})
P_{dry}	Power consumption required for the air condensers (kW_e)
P_{cond}	Power consumption by the pump that draws water from the sea to the power cycle condenser (kW_e)
$P_{i,pump1}$	Ideal power required by pump 1 (kW_e)
$P_{i,pump2}$	Ideal power required by pump 2 (kW_e)
P_{net}	Net electrical power generated in the power cycle (kW_e)
P_r	Thermal power required in the reheater (kW_{th})
$P_{r,pump1}$	Actual power required by pump 1 (kW_e)
$P_{r,pump2}$	Actual power required by pump 2 (kW_e)
P_{pumps}	Total power consumed by the two pumps in the power cycle (kW_e)
P_{turb}	Total power generated by the two turbines in the power cycle (kW_e)
$P_{turb,ST1}$	Power generated by turbine ST1 (kW_e)
$P_{turb,ST2}$	Power generated by turbine ST2 (kW_e)
$P_{Q,collector \rightarrow environment}$	Thermal PTC losses (W_{th})
$P_{Q,collector \rightarrow fluid}$	Useful thermal power supplied by a collector (W_{th})
$P_{spec,dry}$	Specific power consumed by the air condensers ($kW/MW_{nominal}$)
$P_{Q,sun \rightarrow collector}$	Available solar radiation on the collectors' aperture plane (W_{th})
P_{PCS}	Thermal power required in the power conversion system (kW_{th})
P_w	Specific power consumed by the water pump that circulates water through the power cycle condenser (kWh/m^3)
$P_{th,field}$	Thermal power supplied by the solar field (kW_{th})
$P_{th,\ row}$	Thermal power supplied by a row (kW_{th})
P_{th}	Thermal power required by the process (kW_{th})
q_e	Heat transfer per unit of mass of the oil in the power cycle (kJ/kg)

q_s	Heat transfer per unit of mass of the steam in the power cycle (kJ/kg)
Re	Reynolds number
s	Entropy (kJ/kg °C)
$\hat{s}$	Solar vector
$\hat{s}_{E-Z}$	Projection of the solar vector onto the E–Z plane
$\hat{s}_{N-Z}$	Projection of the solar vector onto the N–Z plane
S	Useful pass section of the metallic absorber tube (m^2)
S_E	East coordinate of the solar vector
SM	Solar multiple
S_N	North coordinate of the solar vector
S_Z	Z coordinate of the solar vector
$t_{storage}$	Period for which the system can operate with the thermal energy stored in the storage tank (h)
t_{int}	Time intervals into which the design day is divided (h)
t_{op}	Period of process operation using thermal energy supplied by the collector field (h)
T	Steam and liquid temperature in the power cycle (°C)
T_{abs}	Average temperature of the metallic absorber tube (°C)
T_{amb}	Ambient temperature (°C)
T_i	Oil temperature at the collector inlet (°C)
T_o	Oil temperature at the collector outlet (°C)
T_{sat}	Temperature of the saturated liquid (°C)
TTD	Terminal temperature difference (°C)
U_L	Global thermal loss coefficient from the absorber tube to the environment (W/m^2 °C)
v	Specific volume of the liquid through the pumps present in the power cycle (m^3/kg)
V	Oil velocity inside the absorber tube (m/s)
w_e	Work per unit of mass realised by the steam over the power cycle (kJ/kg)
w_s	Work per unit of mass realised by the steam circulating through the cycle (kJ/kg)
x	Steam quality
γ_c	Average annual usage factor of the thermal storage charge
γ_d	Average annual usage factor of the thermal storage discharge
γ_{St}	Annual storage losses factor
δ_{St}	Fraction of energy absorbed by the solar field that is sent to the storage system
Δh	Specific enthalpy difference of the oil between the collector inlet and outlet (kJ/kg)

ΔT	Temperature increase demanded by the process (°C)
ΔT_c	Oil temperature difference between the collector inlet and outlet (°C)
ρ	Fluid density (kg/m^3)
η_{ST}	Isentropic efficiency of the turbine
η_{th}	Thermal efficiency of the power cycle
μ	Dynamic viscosity of the fluid (kg/m s)
π	Pi number
θ_i	Incidence angle (°)

Acronyms

PTC	Parabolic-trough collector
FWH	Feedwater heater
ST1	High-pressure turbine
ST2	Low-pressure turbine

4.1   Introduction

This chapter describes the modelling of a parabolic-trough (PT) concentrating solar power (CSP) plant that produces electricity. To do this, the modelling of the solar field itself is explained first and then the power cycle, consisting of a reheat Rankine cycle, with steam as the working fluid. This power cycle will be used subsequently to be coupled to a desalination plant, creating what is known as a dual-purpose solar power/water cogeneration plant.

4.2   Modelling of the PT Solar Field

The model used in this research is supported by equations based on the thermal losses of the collector (which uses oil as heat transfer fluid in the absorber tubes), its efficiency curve and the energy balances throughout the collector system (González et al. 2001; Incropera and Dewitt 1996; Zarza 2004). The objective of this model is to size a PT collector (PTC) solar field capable of providing the thermal power required for a dual-purpose solar power/water cogeneration plant. Before explaining these field-sizing equations, some basic concepts of the technology are described.
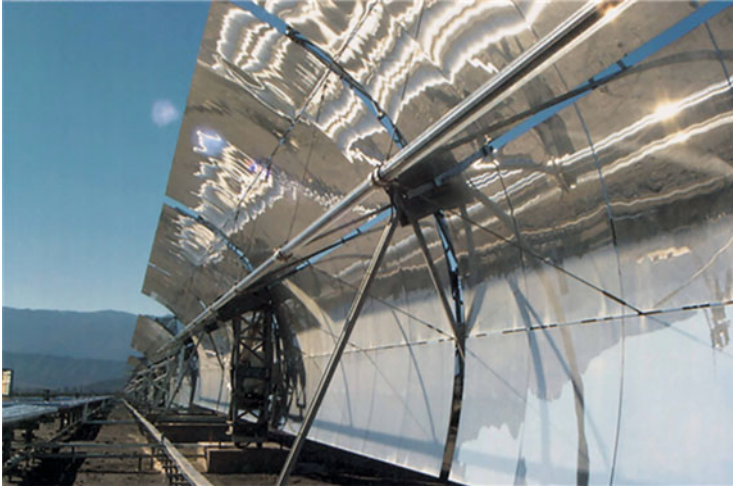
Fig. 4.1 Parabolic-trough collector

4.2.1   Parabolic-Trough Collectors

A PTC (see Fig. 4.1) basically comprises a PT mirror that reflects direct solar radiation, concentrating it onto a receiver (or absorber) tube that is located at the parabolic focal point. Because of its parabolic form, the focal concentration factor is within the 30–100 range of the direct normal irradiance value.

When the solar energy is concentrated on the absorber tube, the fluid that circulates inside the tube heats up, transforming solar radiation into thermal energy in the form of sensible fluid heat, within what is known as the medium temperature range (150–450 °C). A PTC can only make use of direct solar radiation, and this requires the collector to be fitted with a solar tracking mechanism that orientates it throughout the day, following the sun's path across the sky. The most common solar tracking system consists of a mechanism that rotates the PTCs around an axis. Generally, this tracking is carried out with the axis positioned east–west or north–south. Figure 4.2 schematically shows the solar tracking of a PTC.

The PT mirror is mounted above the structure, which is generally metallic (see Fig. 4.3), aligned in such a way that the direct solar irradiation is perfectly concentrated on the focal line of the parabola. The absorber tube surface is far smaller than the collector's aperture area (the flat area delimited by the edges of the collector) because of the optic concentration of the solar radiation; this significantly reduces the collector's thermal losses because these are a result not only of temperature but also of the absorber surface itself.

The main components of the PTC are (see Fig. 4.4):
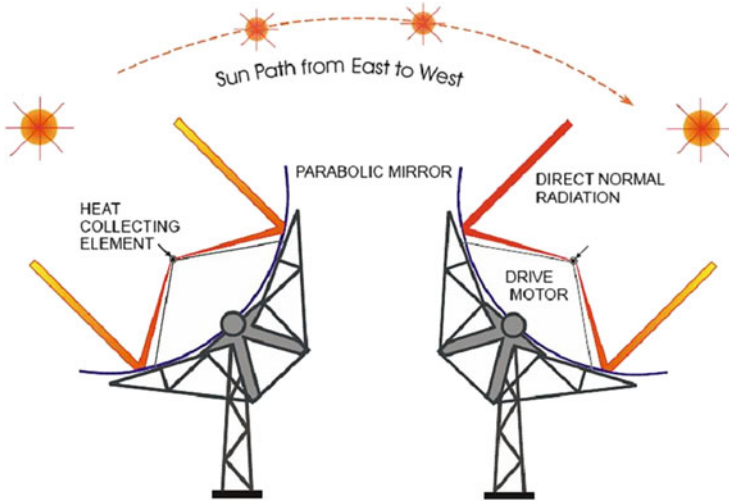
Fig. 4.2 Parabolic-trough collector tracking

Fig. 4.3 Metallic structure onto which the parabolic-trough collector is mounted

- Foundation and support structure
- PT reflector
- Receiver/absorber tube
- Connection between collectors
- Solar tracking system

Of these, the most important are the PT reflector and the receiver/absorber tube because the conversion of solar energy into thermal energy depends on these components.
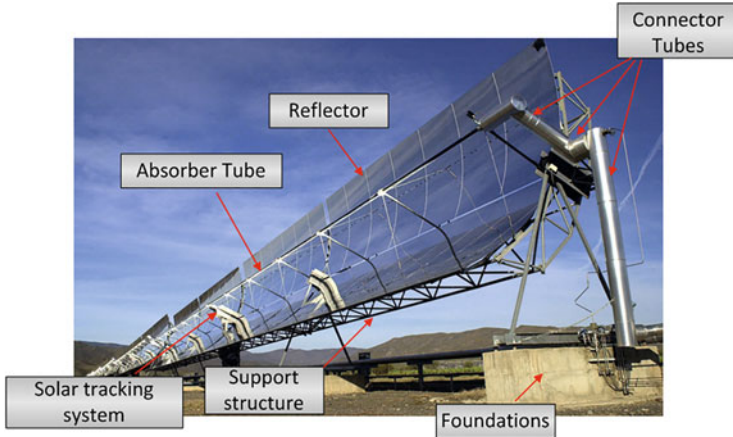
Fig. 4.4 Parabolic-trough collector components

PT Reflector

The PT reflector reflects the solar radiation that falls onto it and projects it in a concentrated form onto the absorber tube situated on the reflector's focal line. In short, this is a mirror, curved parabolically in one of its dimensions, which concentrates all the solar radiation onto the focal line that crosses its aperture plane. The specular surface is made up of silver or aluminium film deposited over a support, which gives it sufficient rigidity. The supports can be metallic, plastic or glass panels (Zarza 2002).

Receiver/Absorber Tube

The lineal receiver for the PTC (see Fig. 4.5) is one of the fundamental elements of all PTCs because the collector's global output largely depends on its operation. The receiver is responsible for converting the concentrated solar radiation into thermal energy, which the calorific fluid transports. It is positioned on the focal line of the PTC, braced to the structure by various support arms. The absorber tube actually consists of two concentric tubes: a metallic interior tube through which the fluid to be heated circulates and a glass exterior tube. They are held together at their ends.

The metal tube is covered with a selective coating that is highly absorbent (about 94 %) in the solar radiation range and has low emission in the infrared spectrum (about 15 %), providing a high level of thermal performance. To avoid thermal loss by convection, a vacuum is required in the space between the interior metal tube and the glass cover. The glass tube is also normally coated with an antireflective treatment on both surfaces to augment its solar radiation transmissivity and, consequently, the collector's optical performance.
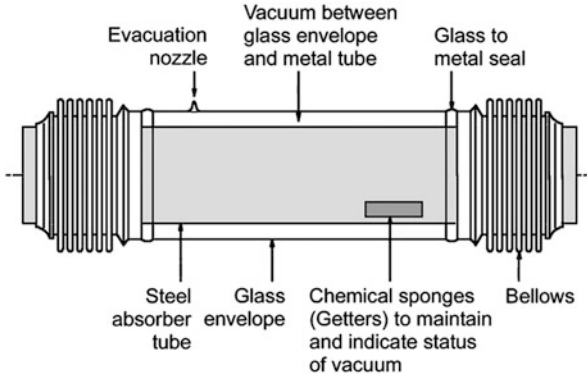
Fig. 4.5 Typical absorber tube from a parabolic-trough collector

Fig. 4.6 Typical parabolic-trough collector solar field

4.2.2   *Sizing of a PTC System*

A typical PTC solar field (see Fig. 4.6) consists of a number of collector rows placed in parallel. The collectors within each row are placed in series in such a way that the working fluid that circulates through the absorber tubes is heated up as it travels from the inlet to the outlet of each row.

The energy source presents a temporal variability; therefore, when designing a PTC field, one must bear in mind that the thermal power supplied by the field at any

moment depends on the boundary conditions existing at that time (available solar radiation, ambient temperature, etc.). Likewise, the thermal power produced by the field equals the nominal power only when the boundary conditions are equal to those assumed in the design.

The set of parameters considered at the design stage of a PTC solar field determines what is known as the "design point"; these include the following:

- Orientation of the collectors' rotation axis
- Day and hour
- Geographical longitude and latitude of the site
- Incidence angle of the direct solar radiation on the collectors
- Direct solar radiation and ambient temperature
- Inlet and outlet temperatures of the collector field
- Nominal thermal power of the collector field
- Type of collector
- Type of working fluid

The choice of these design point parameters is based on a series of considerations, which are discussed next.

Orientation of the Collectors' Rotation Axis

In general, for PTCs, the orientation of the collectors' rotation axis can be either north–south (the normal vector to the aperture area is displaced in the plane formed by the vertical and the cardinal point east) or east–west (the normal vector is displaced in the plane formed by the vertical and the cardinal point south). However, as long as the same applies for all the collector rows, any other orientation type can be adopted. If the orientation of rows was different, then the incidence angle (the angle formed between the surface normal vector and the solar vector) would be different from one row to another, as would the available radiation (which, as we will see later, is a function of the cosine of the angle of incidence). This would make controlling the working fluid temperature at the collector field outlet extremely difficult.

Based on the plant requirements, one or other of the orientations is chosen. The first point to bear in mind is that, depending on the orientation, a greater or lesser seasonal variation in thermal energy is produced by the PTC solar field. Such seasonal variations are mainly determined by the solar radiation incidence angle onto the collectors' aperture plane and by the number of sunlight hours available from sunrise to sunset.

The incidence angle is far larger on winter days than on summer days, making the solar radiation incident on the collector much less in the first case, as defined by the following equation:

Fig. 4.7 Incidence angle variation between winter and summer, considering a north–south orientation
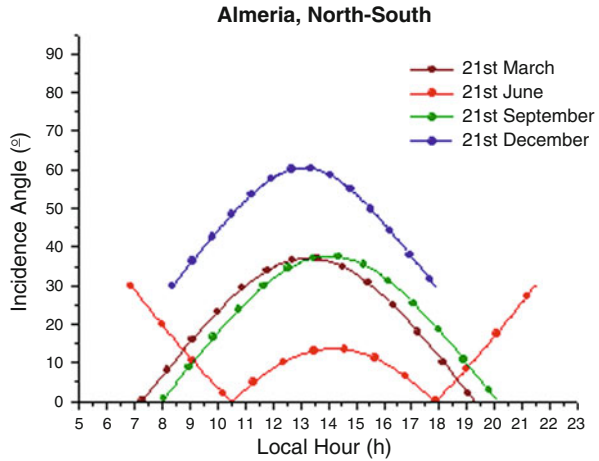
$$P_{Q,\,\text{sun}\rightarrow\text{collector}} = A_c \cdot \text{DNI} \cdot \cos\left(\theta_i\right) \tag{4.1}$$

where $P_{Q,\text{sun}\rightarrow\text{collector}}$ is the available solar radiation on the collectors' aperture plane; A_c is the aperture area of the collector's reflective surface; DNI is the direct normal irradiance and θ_i is the incidence angle.

When the orientation of the collectors' rotation axis is north–south, considerable variations between winter and summer are observed (see Fig. 4.7). Moreover, the number of available sunlight hours from sunrise to sunset is less on a winter's day (21 December) than on a summer's day (21 June). These two factors mean that the thermal energy supplied daily can be three times greater in summer months than in winter months, depending on the geographical latitude and the atmospheric conditions at the installation site.

If the orientation is east–west, the incidence angle variations are far less, generally below 50 %, as can be observed in Fig. 4.8. As a consequence, the thermal input is more stable throughout the year.

For commercial CSP plants, the north–south orientation is preferred because, in spite of the large difference in thermal energy produced between winter and summer, the total energy supplied over the whole year is still greater than that supplied by collectors orientated east–west, which is the aim of such plants.

Day and Time

The design point day is chosen on the basis of the orientation selected. If a north–south orientation has been selected, the choice of design day becomes important when dealing with power plants. If a summer design day is chosen, then during this season the plant is working under nominal conditions, whereas in winter it works well below them, thus affecting its output. Conversely, if a winter design day is chosen, then during the summer a large part of the solar field has to be out of focus

Fig. 4.8 Incidence angle variation between winter and summer, considering an east–west orientation
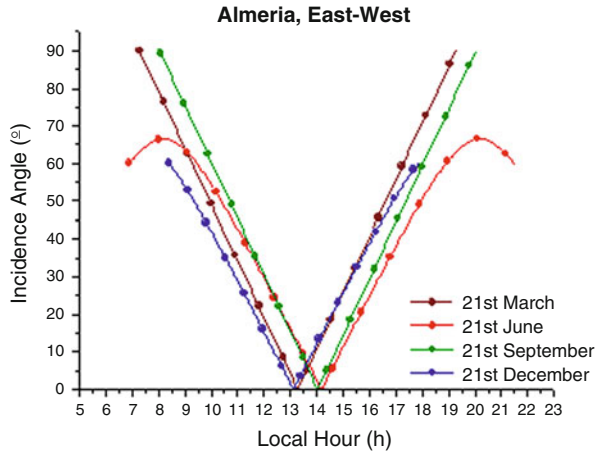
because the turbine is unable to absorb all the thermal power provided by the collector field. Therefore, when a north–south orientation is chosen, a possible option is to design the field on the basis of an autumn or spring day. This means that the turbine works slightly under the nominal load in winter, and the size of the solar field that has to be kept out of operation in summer is less than when a winter design day is chosen.

In the case of an east–west orientation, the choice of a winter or summer day is not of such importance.

It can be concluded that the main points to bear in mind when choosing the design point day are the seasonal variations in peak thermal power and the energy supplied throughout the day by the collector field. This is a result of the varying number of sunlight hours a day and the different solar radiation incidence angles on the solar collectors.

The solar noon is commonly chosen as the design point hour, given that, at that moment, the sun is at its maximum daily elevation and there is more stable direct solar radiation.

Geographical Longitude and Latitude of the Site

The geographical latitude and longitude define the location of the PTC solar field and are data the client should provide on installing the solar plant. They are fundamental input parameters for the solar vector calculation algorithm and are used for the computer programmes that generate the typical meteorological year.

Fig. 4.9 Axes system
adopted for the calculations
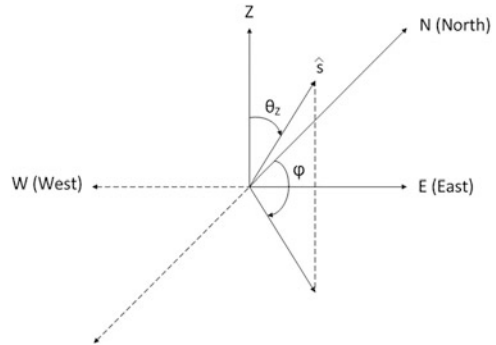
Direct Solar Radiation Incidence Angle on the Collectors

As mentioned above, the incidence angle is the angle that the solar vector and the normal vector form to the PTC aperture plane. This angle is essential in calculating the useful energy that the PTC can supply. Moreover, it is also used to know, or predict, the thermal behaviour of the collector; this depends, among other things, on the geographical coordinates (latitude and longitude) of the collector site, the day of the year and the hour of the day.

The incidence angle is calculated as the arc cosine of the dot product (scalar product) of the normal vector to the PTC aperture plane $(\hat{n})$ and the solar vector $(\hat{s})$, as indicated in the following equation:

$$\theta_i = \cos^{-1}(\hat{n} \cdot \hat{s}) \tag{4.2}$$

First, the calculation of the components of the solar vector $(\hat{s})$ is explained. Figure 4.9 shows which criterion is followed to calculate these components. It should be mentioned that it is easy to find other calculation procedures in the literature that are based on a criterion that has different signs, but the final results are the same if each result is used in accordance with the axes system of the corresponding reference.

In Fig. 4.9, θ_Z is the zenith distance (the angular distance from the zenith to the solar vector) and φ is the solar azimuth angle. These angles can be determined by means of the algorithm developed by Blanco-Muriel et al. (2001). Applying the corresponding trigonometric ratios, the solar vector components are as follows:

$$\begin{aligned}
s_E &= \sin\theta_Z \sin\varphi \\
s_N &= \sin\theta_Z \cos\varphi \\
s_Z &= \cos\theta_Z
\end{aligned} \tag{4.3}$$

Conversely, the normal vector to the aperture plane of a PTC, $\hat{n}$, is calculated taking into account that the PTC is focused when the collector's rotation axis, the solar vector and the normal vector to the collector's aperture plane are on the same plane.

In this case, the normal vector is always the projection of the solar vector onto the corresponding plane, depending on whether the collector's rotation axis is orientated north–south or east–west:

- For north–south orientation, the normal vector is the projection of the solar vector onto the E–Z plane (see Fig. 4.9). Thus, the components of this vector are given by:

$$\hat{n} = \hat{s}_{E-Z} = \left(\frac{s_E}{\sqrt{s_E^2 + s_Z^2}}, 0, \frac{s_Z}{\sqrt{s_E^2 + s_Z^2}} \right) \tag{4.4}$$

- For east–west orientation, the normal vector is the projection of the solar vector onto the N–Z plane (see Fig. 4.9). The components of this vector in this case are given by:

$$\hat{n} = \hat{s}_{N-Z} = \left(0, \frac{s_N}{\sqrt{s_N^2 + s_Z^2}}, \frac{s_Z}{\sqrt{s_N^2 + s_Z^2}} \right) \tag{4.5}$$

Direct Solar Radiation and Ambient Temperature

The direct solar radiation and the ambient temperature of the design point are those corresponding to the chosen design day and hour and are provided by meteorological data for the location of the solar field site.

Inlet and Outlet Temperatures of the Collector Field

The inlet and outlet temperatures of the collector field depend on the operating conditions needed in the process, which is thermally fed by the solar field. The most commonly used values in PT-CSP plants, whose working fluid is thermal oil, are 295 °C and 395 °C for the inlet and outlet temperatures, respectively. The greater the outlet temperature, the greater the power block output. However, in PTC plants employing thermal oil as the working fluid, the limiting factor to attaining higher field outlet temperatures is the thermal oil itself. Even though there are absorber tubes that can work at fluid temperatures above 500 °C, no viably priced thermal oils exist that can be heated above 400 °C without suffering chemical decomposition (consequently, these tubes are currently being used for direct vapour generation).

When setting the necessary fluid temperature at the solar field outlet, one should bear in mind that it needs to be at least 10 or 15 °C above the vapour temperature required at the generator outlet.

Nominal Thermal Power of the Collector Field

The thermal power is that supplied by the solar field and is determined by the characteristics of the process, which is thermally fed by the collector field.

Type of Collector

The choice of PTC type is a function of the temperature required for the thermal process. If it is a low-temperature process, the small or medium-sized PTC models are the most appropriate for the task. If one is dealing with a high-temperature process (as is the case for electricity generation using a vapour cycle) then the most appropriate PTC models are large-scale (LS-3 type, EuroTrough, SenerTrough, etc.) all of which work at practically the same operating temperature. Consequently, the choice of PTC type is based on their working temperature output and cost.

Type of Working Fluid

At present, the most commonly used working fluid in PTC solar fields is thermal oil. Choice of the most suitable oil has to take into account the operating parameters of the solar field (maximum and minimum expected temperatures) and the long-term behaviour of the oil. For working temperatures below 295 °C, the type of oil used is one whose freezing point is sufficiently low (below zero), meaning that there is no need to heat it in an auxiliary boiler when the ambient conditions would otherwise require it. Therminol-55 is oil in this group.

For working temperatures of around 400 °C, Therminol VP-1 (maximum working temperature 398 °C) is the best candidate. However, this type of oil has a high freezing point (+12 °C), meaning that it is necessary to employ an auxiliary boiler during winter periods to prevent the temperature falling to this level.

There are also oils with working temperatures above 400 °C, such as Syltherm-800 (maximum working temperature 425 °C, freezing point −40 °C). Nonetheless, its prohibitive cost means that it cannot be used in large-scale electricity-generating plants. Furthermore, it has been demonstrated that this oil undergoes serious property degradation over the long-term, even reaching the point of becoming dangerous.

The manufacturer of the above-mentioned oils (Solutia) supplies software free of charge that enables selection of the type of oil on the basis of the solar field operating parameters (maximum and minimum expected temperatures). This software also provides values for the density, specific heat and viscosity of the oil as a function of its temperature.

Once the design point parameters of the solar field have been defined, its sizing is carried out. For this it is necessary to determine, first, the number of collectors (N_C)

in each row; second, the number of rows (N_F); third, the total number of collectors needed (N_T) along with the total collector area (A_T) required for the solar field; and, finally, the size of thermal storage (if required).

(a) Calculation of the number of collectors in series within each row.

The number of collectors, N_C, connected in series within each row is given by the following expression:

$$N_C = \frac{\Delta T}{\Delta T_c} \tag{4.6}$$

where ΔT is the temperature increase required by the process fed by the solar field; and ΔT_c is the difference in the working fluid temperature between the inlet and the outlet of an individual collector.

The collector temperature increase, ΔT_c, depends on the oil flow rate that circulates around it. To calculate this, the useful thermal power supplied by a PTC, $P_{Q,\text{collector}\rightarrow\text{fluid}}$, is first determined, being equal to the enthalpy increase of the working fluid between the collector inlet and outlet, as shown in the following equation:

$$P_{Q,\text{collector}\rightarrow\text{fluid}} = \dot{m}_{\text{fluid}} \cdot (h_{\text{out}} - h_{\text{in}}) = \dot{m}_{\text{fluid}} \cdot \Delta h \tag{4.7}$$

where $\dot{m}_{\text{fluid}}$ is the mass flow rate of the working fluid; h_{in} is the specific enthalpy of the working fluid at the collector inlet; and h_{out} is its specific enthalpy at the collector outlet.

On the other hand, the useful thermal power can be calculated from the direct normal solar irradiance and the collector parameters, as indicated in the following equation:

$$P_{Q,\text{collector}\rightarrow\text{fluid}} = A_c \cdot \text{DNI} \cdot \cos(\theta_i) \cdot \eta_{\text{opt},0°} \cdot K(\theta_i) \cdot F_e$$
$$- P_{Q,\text{collector}\rightarrow\text{environment}} \tag{4.8}$$

where $\eta_{\text{opt},0°}$ is the optical performance with the incidence angle at $0°$, also known as the peak optimal performance; $K(\theta_i)$ is the incidence angle modifier; F_e is the collector's fouling factor, the value of which is between 0 and 1 ($0 < F_e < 1$); and $P_{Q,\text{collector}\rightarrow\text{environment}}$ is the thermal losses of the collector.

The parameters involved in (4.8) (A_c, DNI, θ_i, $\eta_{\text{opt},0°}$, F_e) are determined by the conditions established in the design point and by the particular characteristics of the PT collector chosen.

The incidence angle modifier, $K(\theta_i)$, is a function of the incidence angle. When the incidence angle is $0°$, the incidence angle modifier is 1, and when the incidence angle is $90°$, the incidence angle modifier is zero. In order to calculate the incidence angle modifier, a parametric equation is used with the coefficients determined

experimentally (Zarza and Ajona 1988). For the LS-3 collector (manufactured by the Israeli company Solel), the incidence angle modifier is provided by the following equation (González et al. 2001):

$$K(\theta_i) = 1 - 2.23073 \cdot 10^{-4}\theta_i - 1.1 \cdot 10^{-4}\theta_i{}^2 + 3.18596 \cdot 10^{-6}\theta_i{}^3$$
$$-4.85509 \cdot 10^{-8}\theta_i{}^4 (0° < \theta_i < 80°)$$
$$K(\theta_i) = 0 (85° < \theta_i < 90°) \tag{4.9}$$

If the model of the PTC is Eurotrough, the incidence angle modifier is given by:

$$K(\theta_i) = \cos\theta_i - 2.859621 \cdot 10^{-5}\theta_i{}^2 - 5.25097 \cdot 10^{-4}\theta_i \tag{4.10}$$

The thermal losses in a PTC, $P_{Q,\text{collector}\rightarrow\text{environment}}$ are based on the coefficient of global thermal loss from the absorber tube to the environment, U_L, as shown in the following equation (Zarza 2004):

$$P_{Q,\text{collector}\rightarrow\text{environment}} = U_L \cdot A_{\text{abs}} \cdot (T_{\text{abs}} - T_{\text{amb}}) \tag{4.11}$$

where T_{abs} is the average temperature of the metallic absorber tube; T_{amb} is the ambient temperature and A_{abs} is the total absorber tube area. This area is determined using the expression:

$$A_{\text{abs}} = L\pi d_0 \tag{4.12}$$

where L is the absorber tube length (which corresponds to the PTC length); and d_0 is its outer diameter.

As a result of heat flow from the external part of the absorber tube towards the oil circulating inside the tube, the absorber tube temperature is considered to be about 10 °C above the average oil temperature.

The global thermal loss coefficient between the absorber tube and the environment is given by the second-degree polynomial equation (Zarza 2004):

$$U_L = a + b \cdot (T_{\text{abs}} - T_{\text{amb}}) + c \cdot (T_{\text{abs}} - T_{\text{amb}})^2 \tag{4.13}$$

where the coefficients a, b and c are determined experimentally. The temperatures are expressed in degrees centigrade.

With (4.7) and (4.8), the temperature difference of the fluid between the collector inlet and outlet, ΔT_c, can be determined once the mass flow rate of the oil circulating through the collector, $\dot{m}_{\text{fluid}}$, is set in the design point.

The criteria for setting the mass flow rate of the oil is that there is sufficient turbulence inside the absorbent tube to guarantee its optimal refrigeration, but not too much to deform, or even possibly break, the glass sheathing.

Turbulence is assured when the Reynolds number (Re) is equal to, or greater than, 10^5. The Reynolds number can be expressed using the following equation (Incropera and Dewitt 1996):

$$\text{Re} = \frac{V \times d_\text{i} \times \rho}{\mu} \qquad (4.14)$$

where μ is the dynamic viscosity of the fluid, V is the fluid velocity, d_i is the inner diameter of the absorber tube and ρ is the fluid density.

The fluid parameters (viscosity and density) are determined using the tables of properties supplied by the manufacturer. To obtain these parameters at a specific temperature, an average fluid temperature is established between the nominal inlet and outlet temperatures in the solar field.

Using (4.12), and knowing the absorber tube's inner diameter, the fluid velocity needed for a specific Reynolds number can be determined.

Once the fluid velocity is determined using (4.12), the corresponding mass flow rate, $\dot{m}_\text{fluid}$, can also be determined:

$$\dot{m}_\text{fluid} = V \cdot S \cdot \rho \qquad (4.15)$$

The S parameter corresponds to the cross-sectional area of the metallic absorber tube, which is provided by the expression:

$$S = \frac{\pi}{4} d_i{}^2 \qquad (4.16)$$

Once the mass flow rate is established, (4.7) is used to calculate the oil temperature variation throughout the collector. In this equation, the enthalpy increase, Δh, can be expressed as a function of the oil's specific heat at a constant pressure, C_p. Integrating C_p between the oil temperature at the inlet and the outlet of the collector (T_o and T_i, respectively), the following equation is obtained:

$$P_{Q,\text{collector}\rightarrow\text{fluid}} = \dot{m}_\text{fluid} \cdot (h_\text{out} - h_\text{in}) = \dot{m}_\text{fluid} \cdot \Delta h = \dot{m}_\text{fluid} \int_{T_\text{i}}^{T_0} C_\text{p} dT \qquad (4.17)$$

The specific heat of the working fluids normally used in these systems is a linear function of the temperature:

$$C_\text{p} = d + e \cdot T \qquad (4.18)$$

The coefficients d and e are the fitting parameters of the polynomial equation and can be determined using tables that give C_p as a function of the temperature (provided by the manufacturer).

Establishing that the collector's inlet oil temperature, T_i, is equal to the average solar field oil temperature (the average temperature between the inlet and outlet temperatures in the solar field), the following equation is obtained, which can be used to determine T_o:

$$P_{Q,\text{collector}\rightarrow\text{fluid}} = \dot{m}_{\text{fluid}} \cdot \left[d \cdot (T_o - T_i) + 1/2 \cdot e \cdot \left(T_o^2 - T_i^2 \right) \right] \qquad (4.19)$$

With T_o, the increase in fluid temperature ΔT_c is obtained straightforwardly. Finally, by using (4.6), the number of collectors, N_C, to connect in series in each of the solar field rows can be determined. Normally, using (4.6), a real decimal number is obtained. For the most common configuration, "central feed", in which the inlet and outlet of the collector rows are on the same side, in the form of a "U", the number is usually rounded up to an even number to ensure that the two sides of the "U" are of the same length. Rounding up to a higher even number means an increase in the number of collectors per row. An extra collector per row means a flow rate increase in order to obtain the same temperature differential, resulting in an increase in the Reynolds number and, thus, in the heat transfer within the collectors. Therefore, the Re is not too low in winter, especially in the case of a north–south orientation being chosen, resulting in proper operation of the solar field in both summer and winter.

Calculation of the new flow rate, taking into account the new number of collectors, is carried out using the following expression:

$$\dot{m}'_{\text{fluid}} = \dot{m}_{\text{fluid}} \cdot \left(\frac{N_C{}'}{N_C} \right) \qquad (4.20)$$

where $\dot{m}_{\text{fluid}}$ and N_C are the mass flow rate and the initial number of collectors obtained, respectively, and $\dot{m}'_{\text{fluid}}$ and N_C' are the modified flow rate and number of collectors, respectively.

(b) Calculation of the number of parallel rows required by the solar field.

Calculation of the number of parallel rows needed in the solar field is the second step in determining its size. The calculation is different depending on whether the solar system includes thermal storage or not. The procedure for each is explained below.

Solar system with no thermal storage

In this case, the number of rows is determined by dividing the total thermal power required by the process, P_{th}, by the thermal power supplied by a collector row in the design point, $P_{\text{th,row}}$:

$$N_F = \frac{P_{th,process}}{P_{th}} \qquad (4.21)$$

where $P_{th,row}$ is calculated using the following expression:

$$P_{th,row} = P_{Q,collector \rightarrow fluid} \cdot N_C \qquad (4.22)$$

where $P_{Q,collector \rightarrow fluid}$ is determined using (4.8).

Solar system with thermal storage

Here, the number of rows is determined by dividing the thermal energy required by the process, E_{th}, during sunlight hours (from sunrise to sunset on the design day) by the thermal energy supplied by a row of collectors during the design day, $E_{th,row}$, as shown in the following equation:

$$N_F = \frac{E_{th}}{E_{th,row}} \qquad (4.23)$$

The thermal energy required by the process is obtained by multiplying the thermal power of the process working at nominal load by the hours the process has to operate fed by the solar field, t_{op}. Therefore:

$$E_{th} = P_{th} \cdot t_{op} \qquad (4.24)$$

The number of operating hours should be provided by the client, who decides how many hours the plant has to operate with the solar field at nominal load during the design day.

The thermal energy that a row of N_C collectors supplies during the design day is determined by the following expression:

$$E_{th,row} = \sum_{i=0}^{i=24} P_{th,row} \cdot t_{int} \qquad (4.25)$$

where t_{int} are the time intervals into which the design day is divided from sunrise to sunset.

To calculate the thermal energy corresponding to a specific period, the direct solar radiation and ambient temperature data for each of the time intervals throughout the design day are needed, which are normally obtained every 5 or 10 min. Therefore, $P_{Q,collector \rightarrow fluid}$ (4.8) and $P_{th,row,}$ (4.22) are obtained for each instant. Multiplying $P_{th,row}$ by the time interval, the thermal energy can be calculated.

(c) Calculation of the total number of collectors and the total collector area required by the solar field.

Once the number of collectors per row, N_C, and the number of rows in the field, N_F, have been established, calculating the total number of collectors is simply a product of both variables.

The total collector area required for the solar field is determined by multiplying the total number of collectors, N_T, by the aperture area (A_c) of the PTC.

(d) Size of the thermal storage system.

There are periods throughout the design day when the designed collector field supplies less thermal energy than the process demands for operating at nominal charge (a deficit), as well as periods in which the solar field supplies more energy than the process can consume (a surplus). The storage system stores excess thermal energy during times of surplus so that it can become available at times of deficit. Therefore, the size of the thermal storage system can be determined using the quantity of excess energy in times of surplus throughout the day, between t_1 and t_2 instants. This energy, $E_{th,stored}$, is determined using the following expression:

$$E_{th,stored} = \sum_{i=t_1}^{i=t_2} \left(P_{th,field}(i) - P_{th,process}\right) \tag{4.26}$$

$P_{th,field}$ is the thermal power supplied by the solar field and is given by:

$$P_{th,field} = P_{th,row} \cdot N_F \tag{4.27}$$

Two cases can be distinguished. In the first case, the nominal thermal power is lower than the nominal power required by the process; this occurs when the solar field has been sized to work for fewer hours than the available sunlight hours. In the second case, the nominal thermal power is greater than the nominal power required by the process; this occurs when the solar field has been sized to feed the plant for more hours than the sunlight hours available.

The result of the first case is depicted in Fig. 4.10, showing the thermal power demanded by the process along with that supplied by the solar field throughout the design day. The shaded area with diagonal lines shows the surplus thermal energy, whereas the shaded area with crossed lines shows the thermal energy deficit. As can be seen, areas of surplus correspond with the periods from 5.00 to 8.00 h and from 16.00 to 19.00 h, whereas the area of deficit is from 8.00 to 16.00 h. The deficit areas ought to be equal to the surplus areas, ensuring that excess thermal energy resides in the storage system during these surplus periods ready for use during deficit periods.

The result of the second case is shown in Fig. 4.11. As can be seen, the surplus area corresponds to the period from 6.00 to 19.00 h, and the deficit areas from 0.00 to 5.30 h and from 19.00 to 24.00 h.

Another variable to determine in a thermal storage system is the number of hours that the system can operate using the stored energy in the thermal storage tank; this is obtained as follows:
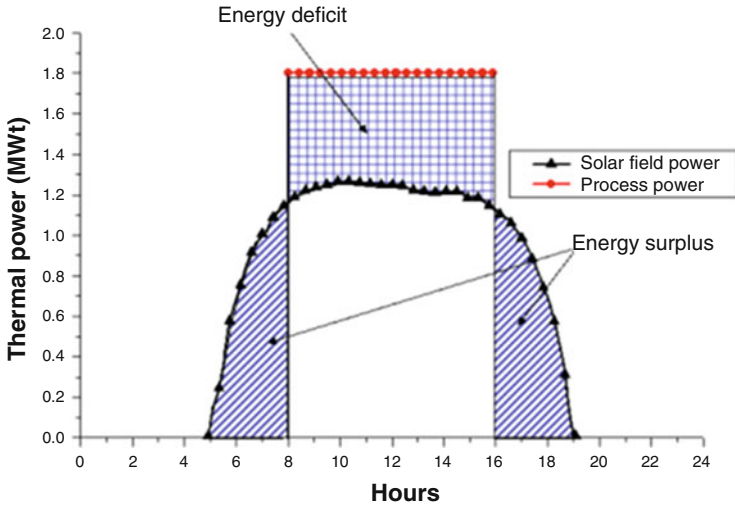
Fig. 4.10 Thermal power produced by the solar field and demanded by the process when the solar field feeds the plant for less hours than the sunlight hours
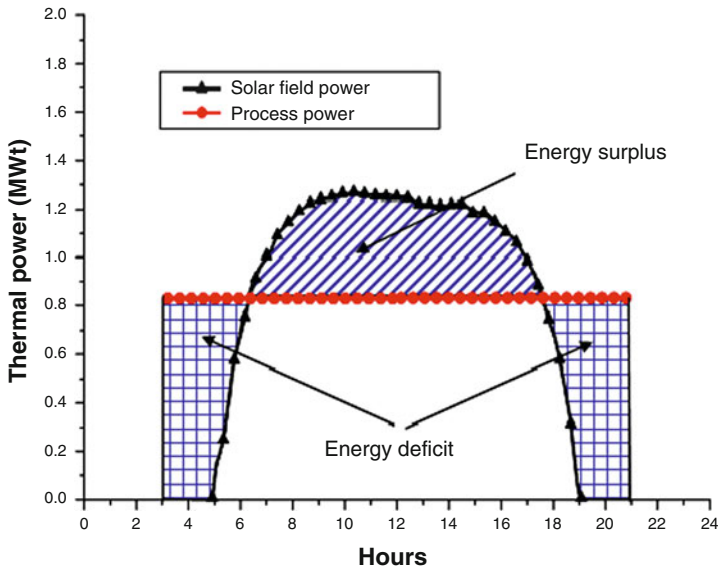
Fig. 4.11 Thermal energy produced by the solar field and demanded by the process when the solar field feeds the plant for more hours than the sunlight hours available

$$t_{\text{storage}} = \frac{E_{\text{th, stored}}}{P_{\text{th}}} \tag{4.28}$$

In all storage systems with a heat exchanger (as is the case with molten salts), thermal losses have to be considered, both in the storage system and in the heat exchangers. This means that the charge and discharge usage factors are less than 1, resulting in lower output than if the energy were transferred directly to the cycle. If δ_{St} is the absorbed energy fraction by the solar field that is sent to the storage system, and γ_{c} and γ_{d} are the average annual charge and discharge usage factors, respectively, the annual general output is lower as a result of the annual storage loss factor, γ_{St}, given by:

$$\gamma_{\text{St}} = 1 - \delta_{\text{St}} \cdot (1 - \gamma_{\text{c}} \cdot \gamma_{\text{d}}) \tag{4.29}$$

Therefore, the storage system should be sized to supply the power needed for the power cycle to work under nominal conditions, considering the existing thermal losses.

On the other hand, there is an important parameter associated with the design point that gives an idea of the oversizing of the solar field with respect to the power cycle (process), the solar multiple (SM). This parameter is defined as the relationship between the power sent by the solar field in the design point, $P_{\text{th,field}}$, and the power needed by the power cycle (process) to work under nominal conditions, P_{th}:

$$\text{SM} = \frac{P_{\text{th, field}}}{P_{\text{th}}} \tag{4.30}$$

When the thermal power supplied by the solar field is enough to make the process work under the nominal conditions at the design point, the SM value is equal to one. However, this only happens at the instant corresponding to the design point; for the rest of the time, it is less than one. In order to make the turbine work under steady-state conditions for longer, the SM value must be greater than one, as can be seen in

Fig. 4.12 Thermal power delivered by the solar field at different solar multiple values
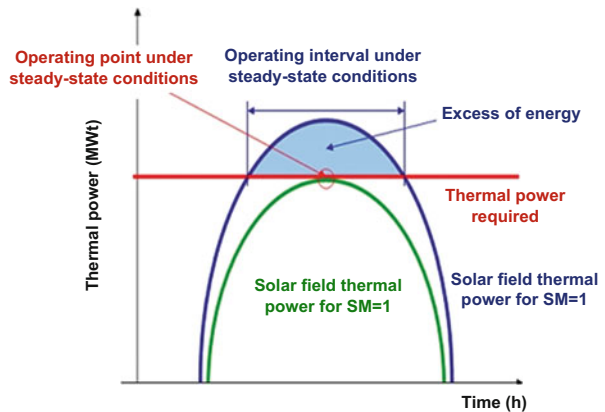
Fig. 4.12. This means that the thermal capacity of the collector field exceeds the steam generator demand and this excess can be accumulated in the storage system. If the sizing of the solar field is carried out assuming thermal storage, the power delivered by the solar field is greater than the power necessary by the power cycle to work under nominal conditions, resulting in the SM always being greater than 1.

Typical values of the SM are between 1.2 and 1.8, which correspond to autonomous periods with the plant at full load for 3 h and 8 h, respectively (although this value depends on the available annual radiation).

4.3 Power Cycle Modelling

4.3.1 Power Cycle

The power cycle used in the Concentrating Solar Power plant is a regenerative Rankine cycle with reheat, which was selected on the basis of commercial CSP plants (Blanco-Marigorta et al. 2011). The cycle diagram is represented in Fig. 4.13

As can be observed, the thermal oil is heated while circulating through the absorber tubes of the solar collectors. Therefore, the solar energy is converted into thermal energy in the form of oil's sensible heat and subsequently stored in the thermal storage system with molten salts. A part of the oil coming from the solar collectors is directed to the oil–salt heat exchanger. Consequently, the thermal energy of the oil is transferred to the salt and this is stored in the hot tank during its load cycle. During the discharge cycle, the salt and oil flows are inverted in the oil–salt heat exchanger and, thus, the thermal energy of the salt is transferred to the oil. The hot oil then passes through a power conversion system (made up of a preheater, an evaporator and a superheater), where steam generation takes place in the power cycle. Furthermore, there is an auxiliary boiler capable of heating the oil in parallel to the collector field to guarantee operation of the solar plant for 24 h a day.

The resulting superheated steam from the power conversion system passes first through a high-pressure turbine (ST1), where it is expanded to reach intermediate pressure. From this turbine, the first regeneration process takes place by extracting part of the steam passing through it. This steam is used to preheat the feedwater in a feedwater heater (FWH 1). Here, the heat is transferred from the extracted steam to the feedwater without mixing the two currents. On the one hand, condensed steam is obtained, and on the other, feedwater at a higher temperature. The resulting condensed steam is introduced to the next feedwater heater (FWH 2) to take advantage of its sensible heat. This occurs after passing through a valve (valve 1), which traps any steam remaining in the condensed current and reduces the liquid pressure to the interior FWH pressure, thus avoiding any evaporation flash (which can occur if the liquid enters a compartment whose pressure is lower than its corresponding saturation pressure).
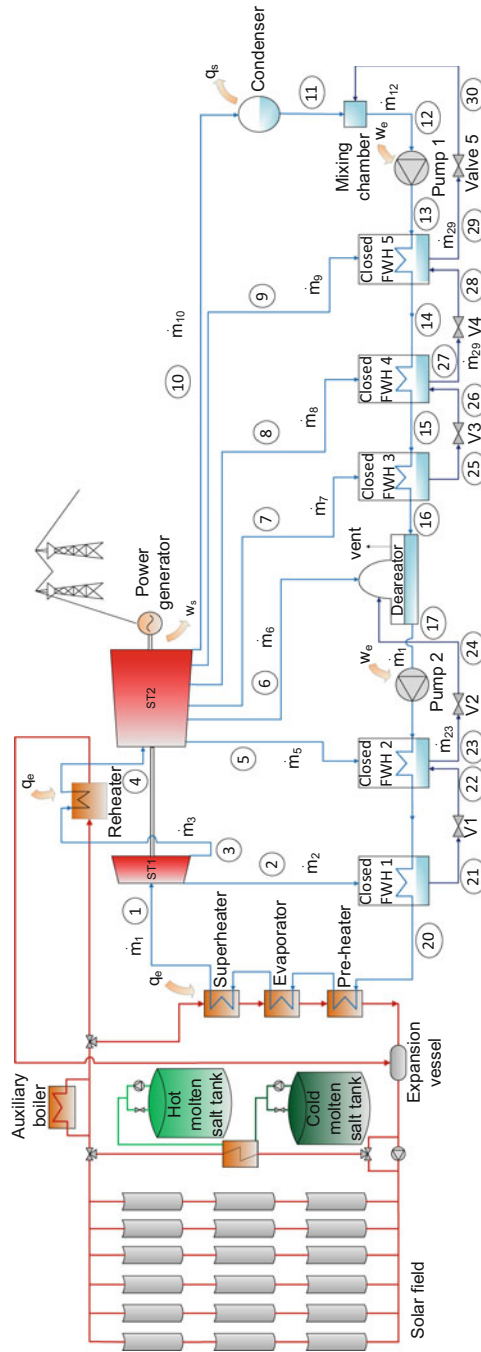
Fig. 4.13 Scheme of the power cycle of the CSP plant, showing points *1–30*

The steam not extracted from the high-pressure turbine continues expanding until it leaves at the required reheater pressure. In the reheater, the steam is superheated by the thermal energy coming from the solar system. Subsequently, the superheated steam enters the low-pressure turbine (ST2), where it expands up to the condenser pressure, producing work by rotation of the electrical generator. A regenerative process is also carried out by this turbine via five steam extractions. In this case, four closed (and one open) feedwater heaters are used (FWH 2–5) to preheat the feedwater. The open FWH is basically a mixing chamber, where the steam extracted from the turbine is mixed with the feedwater, transferring its phase-change enthalpy. Furthermore, it also eliminates the oxygen and the non-condensable gases in the feedwater, thus avoiding corrosion phenomena in the power conversion system. All of the condensed currents leaving the closed water heaters (FWH 2–5) enter the next water heater after passing through the valves (valves 2–5), which trap the steam before entry.

Finally, the exhaust steam that leaves the low-pressure turbine is condensed in the condenser at a constant pressure, by transferring heat from the steam to the refrigeration medium via the condenser. Therefore, exhaust heat is transferred to the environment in this process. The steam leaves the condenser as saturated liquid, which is mixed in the mixing chamber with the condensed steam coming from the last feedwater heater (FWH 5). From this mixture, a condensate (feedwater) is obtained that is pumped at a sufficiently high pressure to circulate through the closed water heaters (FWH 3–5) as well as the interior of the open heater. Following this, the feedwater is pumped again to the open FWH outlet up to the required pressure in the power conversion system. The feedwater passes through the other two feedwater heaters (FWH 1–2) before returning to the preheater of the power conversion system to complete the cycle.

4.3.2 Thermodynamic Analysis of the Cycle Components

The power cycle was modelled assuming that all the components associated with it (pump, power conversion system, FWHs, valves, condenser, mixing chamber and turbine) are adiabatic and operate in steady state. Changes in the potential and kinetic energy of the fluid streams are assumed negligible, as well as the changes in the fluid state between the outlet and the inlet of each component. However, certain pressure losses in the steam lines and the closed FWHs are considered. Finally, the following assumptions are taken in account: condensed steam exits the condenser as saturated liquid ($x = 0$) and no pressure losses occur; feedwater exits the deaerator as saturated liquid ($x = 0$); and the condensate mixture leaves the mixing chamber as saturated liquid ($x = 0$).

Taking some of the above-mentioned considerations into account, the equation for the balance of energy in steady state, applied to the steam that circulates around the cycle, is reduced to:

$$(q_e - q_s) + (w_e - w_s) = h_f - h_i \tag{4.31}$$

where:

- q_e is the heat transfer per unit of mass realised by the heat transfer fluid (in this case oil) in the thermodynamic cycle. This heat transfer corresponds to that produced from the oil exiting the solar field into the thermodynamic cycle (to the power conversion system and the reheaters present in the cycle) (see Fig. 4.13).
- q_s is the heat transfer per unit of mass to the environment realised by the steam that circulates around the cycle. This heat transfer corresponds to that produced from the steam entering the condenser on its way to the outside, as a consequence of its condensation (see Fig. 4.13).
- w_e is the work done, per unit of mass of the steam that circulates around the cycle. This work corresponds to that required by the pumps present in the cycle.
- w_s is the work done by the thermodynamic cycle, per unit of mass of steam that circulate around the cycle. This work corresponds to that realised by the turbines (see Fig. 4.13).
- h_f is the specific enthalpy of the steam when it has reached its final state in the thermodynamic cycle.
- h_i is the specific enthalpy of the steam in its initial state in the thermodynamic cycle.

In the following model, the input parameters are the pressure and temperature of the superheated steam at the entrance to turbine ST1 (P_1, T_1); the pressure of the steam that exits ST1 (P_3); the temperature and pressure of the steam that exits the reheater (P_4, T_4); the pressure of the steam that exits turbine ST2 (P_{10}); the pressure of the steam that is extracted from ST1 (P_2); and the steam pressure for the extractions in turbine ST2 (P_5, P_6, P_7, P_8 y P_9). The output parameters given by the model are the pressures and the remaining temperatures in each of the currents, the mass flow rates and the specific enthalpies for all of the cycle currents.

The model's equations that are applied to each of the cycle components are shown below. In order to obtain the mass flow rates for all the cycle currents, the corresponding equations are expressed as power instead of work.

Turbines

Inside a turbine, steam expands and mechanical work is produced by rotation of the axis connected to the electrical generator. In the thermodynamic cycle presented in Fig. 4.13, there are two turbines, ST1 and ST2.

Turbine ST1

As can be observed in Fig. 4.13, superheated steam at mass flow rate, $\dot{m}_1$, enters the turbine where it expands. Part of this flow, $\dot{m}_2$, is extracted and therefore only partially expands in the turbine. The rest of the steam ($\dot{m}_3 = \dot{m}_1 - \dot{m}_2$) expands completely until reaching the reheater entry pressure. Considering that the steam expands isentropically in the turbine (ideally without irreversibilities), the power generated by this turbine, $P_{\text{turb,ST1}}$, is given by:

$$P_{\text{turb, ST1}} = \dot{m}_1 \cdot (h_1 - h_{2,i}) + \dot{m}_3 \cdot (h_{2,i} - h_{3,i}) \qquad (4.32)$$

where h_1 is the specific enthalpy of the steam entering the turbine; $h_{2,i}$ and $h_{3,i}$ are the specific enthalpies of the steam that is extracted and the steam leaving the turbine, respectively, considering the isentropic steam expansion.

The specific enthalpy and entropy of the steam entering the turbine are a function of the temperature and pressure at that point:

$$h_1 = f(T_1, P_1)$$
$$s_1 = f(T_1, P_1) \qquad (4.33)$$

Conversely, the specific enthalpy of the steam that is extracted from the turbine at point 2 (see Fig. 4.13) is a function of the entropy and pressure at that point:

$$h_{2,i} = f\left(s_{2,i}, P_2\right) \qquad (4.34)$$

where $s_{2,i}$ is the steam entropy in point 2 considering isentropic expansion. In this case, the steam entropies at the outlet and at the inlet are equal:

$$s_{2,i} = s_1 \qquad (4.35)$$

Finally, the steam temperature in point 2 is a function of the entropy and pressure at that point:

$$T_{2,i} = f\left(s_{2,i}, P_2\right) \qquad (4.36)$$

At point 3, the specific enthalpy of the steam at the outlet of turbine ST1 is a function of the entropy and pressure, as indicated here:

$$h_{3,i} = f\left(s_{3,i}, P_3\right) \qquad (4.37)$$

Here, as before, the entropy of the steam at the turbine outlet is equal to that at the inlet:

$$s_{3,i} = s_1 \tag{4.38}$$

The steam temperature in point 3 is a function of the entropy and pressure:

$$T_{3,i} = f\left(s_{3,i}, P_3\right) \tag{4.39}$$

However, as a result of irreversibilities, such as fluid friction, the turbine generates less power than it would under ideal conditions. This is represented using the isentropic efficiency of the turbine (η_t), defined as:

$$\eta_t = \frac{h_{e,t} - h_{s,t}}{h_{e,t} - h_{st,i}} \tag{4.40}$$

where $h_{e,t}$ is the specific enthalpy of the steam entering the turbine and $h_{s,t}$ is the real enthalpy (taking irreversibilities into account) of the steam at the outlet, whereas $h_{st,i}$ is the ideal specific enthalpy of the steam (without irreversibilities).

Applying this equation to turbine ST1, the real specific enthalpies of the steam that is extracted from the turbine, h_2, and that of the steam leaving the turbine, h_3, can be calculated as follows:

$$\begin{aligned} \eta_{ST1,1\rightarrow 2} &= \frac{h_1 - h_2}{h_1 - h_{2,i}} \\ \eta_{ST1,1\rightarrow 3} &= \frac{h_1 - h_3}{h_1 - h_{3,i}} \end{aligned} \tag{4.41}$$

where $\eta_{ST1,1\rightarrow 2}$ and $\eta_{ST1,1\rightarrow 3}$ are the isentropic turbine efficiencies when the steam is expanded from point 1 to 2 and from point 1 to 3, respectively.

In this case, the temperatures and real entropies in points 2 and 3 are given by:

$$\begin{aligned} T_2 &= f(P_2, h_2) \\ s_2 &= f(P_2, h_2) \\[6pt] T_3 &= f(P_3, h_3) \\ s_3 &= f(P_3, h_3) \end{aligned} \tag{4.42}$$

Considering real expansion in the turbine, the power generated is determined as:

$$P_{turb,ST1} = \dot{m}_1 \cdot (h_1 - h_2) + \dot{m}_3 \cdot (h_2 - h_3) \tag{4.43}$$

Turbine ST2

In turbine ST2, the steam (at flow rate $\dot{m}_3$) enters and expands after leaving the reheater, generating a specific power by the rotation of the axis connected to the electric generator. Five extractions are carried out, so some steam (at flow rates $\dot{m}_5$,

$\dot{m}_6$, $\dot{m}_1$, $\dot{m}_8$ and $\dot{m}_9$) is partially expanded in the turbine, and the remainder ($\dot{m}_{10}$ $= \dot{m}_3 - \dot{m}_5 - \dot{m}_6 - \dot{m}_7 - \dot{m}_8 - \dot{m}_9$) expands completely until reaching the condenser pressure.

The specific enthalpy and entropies of the steam entering the turbine (point 4) are a function of the temperature and pressure at that point:

$$h_4 = f(T_4, P_4)$$
$$s_4 = f(T_4, P_4)$$
(4.44)

Considering isentropic expansion at point 5, the specific enthalpy of the steam at this point is a function of the entropy and pressure:

$$h_{5,i} = f\left(s_{5,i}, P_5\right) \tag{4.45}$$

As before, isentropic steam expansion is considered, so the steam entropy at point 5 is equal to the steam entropy at the inlet of the turbine:

$$s_{5,i} = s_4 \tag{4.46}$$

The steam temperature extracted from the turbine at point 5 is a function of the entropy and pressure at that point:

$$T_{5,i} = f\left(s_{5,i}, P_5\right) \tag{4.47}$$

The same methodology is applied to the extractions carried out at points 6, 7, 8 and 9. Finally; applying (4.40) to all of the extraction points of the steam turbine, the isentropic efficiencies in each case are given by the following expressions:

$$\begin{aligned}
\eta_{ST2,4\rightarrow5} &= \frac{h_4 - h_5}{h_4 - h_{5,i}} \\
\eta_{ST2,4\rightarrow6} &= \frac{h_4 - h_6}{h_4 - h_{6,i}} \\
\eta_{ST2,4\rightarrow7} &= \frac{h_4 - h_7}{h_4 - h_{7,i}} \\
\eta_{ST2,4\rightarrow8} &= \frac{h_4 - h_8}{h_4 - h_{8,i}} \\
\eta_{ST2,4\rightarrow9} &= \frac{h_4 - h_9}{h_4 - h_{9,i}} \\
\eta_{ST2,4\rightarrow10} &= \frac{h_4 - h_{10}}{h_4 - h_{10,i}}
\end{aligned} \tag{4.48}$$

From these expressions, the specific enthalpies of the steam are determined at points 5, 6, 7, 8, 9 and 10, taking into account the irreversibilities of the system.

Once the enthalpies are known, the temperature and the steam entropy at those points are determined as follows:

$$
\begin{aligned}
T_5 &= f(P_5, h_5) \\
s_5 &= f(P_5, h_5) \\
T_6 &= f(P_6, h_6) \\
s_6 &= f(P_6, h_6) \\
T_7 &= f(P_7, h_7) \\
s_7 &= f(P_7, h_7) \\
T_8 &= f(P_8, h_8) \\
s_8 &= f(P_8, h_8) \\
T_9 &= f(P_9, h_9) \\
s_9 &= f(P_9, h_9) \\
T_{10} &= f(P_{10}, h_{10}) \\
s_{10} &= f(P_{10}, h_{10})
\end{aligned}
\tag{4.49}
$$

In this way, considering the real expansion in the turbine, the power it generates is expressed as:

$$
\begin{aligned}
P_{\text{turb, ST2}} = {} & \dot{m}_3 \cdot (h_4 - h_5) + \dot{m}_6 \cdot (h_5 - h_6) + \dot{m}_7 \cdot (h_6 - h_7) + \dot{m}_8 \\
& \cdot (h_7 - h_8) + \dot{m}_9 \cdot (h_8 - h_9) + \dot{m}_{10} \cdot (h_9 - h_{10})
\end{aligned}
\tag{4.50}
$$

Finally, the total power obtained from the two turbines present in the cycle is given by:

$$
P_{\text{turb}} = P_{\text{turb, ST1}} + P_{\text{turb, ST2}}
\tag{4.51}
$$

Reheater

Steam at flow rate, $\dot{m}_3$, enters the reheater from turbine ST1, and superheated steam is obtained at the outlet. The thermal power required is given by:

$$
P_r = \dot{m}_3 \cdot (h_4 - h_3)
\tag{4.52}
$$

where h_3 and h_4 are the specific steam enthalpies at the inlet and outlet of the reheater, respectively.

Condenser

Steam at flow rate, $\dot{m}_{10}$, enters the condenser after leaving turbine ST2 as exhaust vapour, and condensed liquid is obtained at the outlet. As mentioned above, the pressure losses from this component are considered negligible; thus, the thermal power dissipated to the atmosphere is determined by the following expression:

$$P_{\text{c}} = \dot{m}_{10} \cdot (h_{10} - h_{11}) \qquad (4.53)$$

where h_{10} and h_{11} are the specific steam enthalpies at the condenser inlet and the liquid at its outlet, respectively.

It is considered that the liquid exits the condenser in a saturated state ($x_{11} = 0$). Knowing the quality and the pressure at the outlet of the condenser, the enthalpy and temperature are easily calculated:

$$h_{11} = f(P_{11}, x_{11})$$
$$T_{11} = f(P_{11}, x_{11}) \qquad (4.54)$$

Depending on the type of refrigeration used (i.e. wet or dry cooling), parameters related to the refrigeration system need to be calculated. In the case of once-through or evaporative water cooling, the water flow rate required in the condenser has to be determined. In the case of once-through cooling, the water flowing through the condenser is seawater, whereas it is fresh water for evaporative water cooling. In both cases, the flow rate necessary, F_{cond}, is determined as follows:

$$F_{\text{cond}} = F_{\text{w}} \cdot P_{\text{turb}} \qquad (4.55)$$

where F_{w} is the specific flow rate of the water required, based on the gross electricity production.

Furthermore, in the case of once-through and evaporative water cooling, the electricity consumption needed to pump the water through the power plant condenser has to be taken into account. This consumption is determined as follows:

$$P_{\text{cond}} = P_{\text{w}} \cdot F_{\text{cond}} \qquad (4.56)$$

where P_{w} is the specific power consumed by the pump.

In the case of dry cooling, the consumption is given by the power consumed by the air condensers:

$$P_{\text{dry}} = P_{\text{spec,dry}} \cdot P_{\text{turb}} \qquad (4.57)$$

where $P_{\text{spec,dry}}$ is the specific power consumed by the air condensers.

Mixing Chamber

The two condensate flows from the condenser (at flow rate $\dot{m}_{10}$) and FWH 5 (at flow rate $\dot{m}_{29}$) are mixed in the mixing chamber. The resulting mixture (at flow rate $\dot{m}_{12}$) leaves the mixing chamber as saturated liquid ($x_{12} = 0$) and at the same pressure as

the mixing currents. This component is evaluated by an energy balance between the inlet and outlet:

$$\dot{m}_{12} \cdot h_{12} = \dot{m}_{10} \cdot h_{11} + \dot{m}_{29} \cdot h_{30} \tag{4.58}$$

h_{11} being the specific enthalpy of the saturated liquid coming from the condenser, and h_{30} the specific enthalpy of the saturated liquid coming from the FWH 5 heater.

The saturated liquid temperature at the outlet of the mixing chamber is determined by its dependence on the pressure:

$$T_{\text{sat}, 12} = f(P_{12}) \tag{4.59}$$

The specific volume of the liquid leaving the mixing chamber can be calculated as a function of the pressure and the quality at that point:

$$v_{12} = f(P_{12}, x_{12}) \tag{4.60}$$

Pumps

Compression of the saturated liquid, which comes both from the mixing chamber and the deareator, takes place in the pumps. During the compression process, the liquid temperature can increase slightly as a result of a slight reduction in volume.

Pump 1

Considering that the saturated liquid flow that enters the pump 1, at flow rate $\dot{m}_{12}$, is compressed isentropically, the required power by this pump is determined as follows:

$$P_{i, pump\,1} = \dot{m}_{12} \cdot (h_{13} - h_{12}) \tag{4.61}$$

where h_{12} and h_{13} are the specific enthalpies of the liquid at the inlet and outlet, respectively.

The required power for the pump can also be determined by the following expression:

$$P_{i, \text{pump}1} = \dot{m}_{12} \cdot v_{12} \cdot (P_{13} - P_{12}) \tag{4.62}$$

where P_{12} and P_{13} are the pressures of the liquid at the pump inlet and outlet, respectively. However, as a result of irreversibilities (such as fluid friction), pressure drops are produced in the power conversion system and in the pipes between the various cycle components. To compensate for these pressure drops, the water has to be pumped at a greater pressure than that required in an ideal cycle.

Therefore, the pump efficiency, called isentropic efficiency ($\eta_{b,1}$), is taken into account and included in the power required by the pump, as follows:

$$P_{r,\text{pump1}} = \frac{P_{i,\text{pump1}}}{\eta_{b,1}} \tag{4.63}$$

The pump outlet temperature, T_{13}, is determined by the pressure and enthalpy at that point:

$$T_{13} = f(P_{13}, h_{13}) \tag{4.64}$$

Pump 2

In the case of pump 2, a saturated liquid flow coming from the deaerator, $\dot{m}_1$, is pumped through the preheaters FWH 1 and FWH 2 until arriving at the power conversion system preheater. Taking into account the same considerations as for pump 1, and considering the irreversibilities of the system, the power required for pump 2 is given as:

$$P_{r,\text{pump2}} = \frac{P_{i,\text{pump2}}}{\eta_{b,2}} \tag{4.65}$$

where $\eta_{b,2}$ is the isentropic efficiency of the pump and $\dot{W}_{i,pump2}$ is the power ideally consumed by pump 2, calculated as follows:

$$P_{i,\text{pump2}} = \dot{m}_1 \cdot (h_{18} - h_{17}) \tag{4.66}$$

where h_{18} and h_{17} are the specific enthalpies of the liquid at the pump inlet and outlet, respectively. The power consumed by the pump can also be calculated as follows:

$$P_{i,\text{pump2}} = \dot{m}_{17} \cdot v_{17} \cdot (P_{18} - P_{17}) \tag{4.67}$$

where v_{17} is the specific volume of the saturated liquid entering the pump and P_{17} and P_{18} are the pressures of the liquid at the pump inlet and outlet, respectively.

The temperature of the liquid leaving the pump is determined by the pressure and the enthalpy at that point:

$$T_{18} = f(P_{18}, h_{18}) \tag{4.68}$$

The power consumed by both pumps is the sum of the power consumed by each one:

$$P_{\text{pumps}} = P_{\text{r,pump1}} + P_{\text{r,pump2}} \tag{4.69}$$

Feedwater Heaters

Feedwater heaters are heat exchangers whose function is to raise the feedwater temperature prior to arrival at the power conversion system, thus improving cycle efficiency (Habib and Zubair 1992). On the one hand, the feedwater is pumped from the outlet of the mixing chamber to the inlet of the power conversion system preheater, where the thermodynamic cycle begins (see Fig. 4.13). On the other hand, the steam extracted from the high and low pressure turbines is the heat transfer fluid (see Fig. 4.13).

Closed Feedwater Heaters

In the case of closed FWHs, heat transfer takes place without the two fluids mixing (the steam and the feedwater). In an ideal FWH, the feedwater is heated up to the steam temperature before leaving the FWH as saturated liquid at the steam pressure. However, in real plants, the feedwater leaves the FWH at a temperature below that of the steam; and the condensed steam leaving the FWH does not do so as saturated liquid at steam pressure. There are two parameters that evaluate the heat transfer performance within the FWH. The first parameter is the terminal temperature difference (TTD), defined as the difference between the saturation temperature corresponding to the steam pressure and the feedwater temperature leaving the FWH. The second parameter is the drain cooler approach (DCA), which is used to deduce the level of liquid present in the FWH and is defined as the difference between the outlet temperature of the condensed steam and the feedwater temperature at the FWH inlet.

Below are descriptions of the equations for each of the heaters present in the power cycle.

FWH 1

Here, the heat transfer takes place from the steam flow extracted from turbine ST1 ($\dot{m}_2$) to a feedwater flow coming from FWH 2 ($\dot{m}_1$). Consequently, the feedwater temperature rises from T_{19} to T_{20} and the steam is condensed, producing a distilled flow equal to the entering steam flow ($\dot{m}_2$). Applying an energy balance through this component, the following equation is obtained:

$$\dot{m}_2 \cdot h_2 + \dot{m}_1 \cdot h_{19} = \dot{m}_2 \cdot h_{21} + \dot{m}_1 \cdot h_{20} \tag{4.70}$$

The enthalpies h_{20} and h_{21} are a function of the pressure and the temperature at the corresponding points:

$$h_{20} = f(T_{20}, P_{20})$$

$$h_{21} = f(T_{21}, P_{21})$$

(4.71)

The condensed steam outlet temperature (T_{21}) is a function of the feedwater temperature at the FWH inlet (T_{19}) and the DCA parameters, as shown below:

$$T_{21} = T_{19} + \text{DCA} \tag{4.72}$$

On the other hand, the feedwater temperature at the FWH outlet (T_{20}) is a function of the saturation temperature to the steam pressure (P_2) and the TTD value:

$$T_{20} = T_{\text{sat}}(P_2) - \text{TTD} \tag{4.73}$$

FWH 3 works in the same way as FWH 1, so the same calculation procedure is applied.

FWH 2

In this component, the heat transfer takes place from the steam flow extracted from turbine ST2 ($\dot{m}_5$) to the feedwater flow coming from pump 2 ($\dot{m}_1$). Furthermore, a liquid flow enters from FWH 1 ($\dot{m}_2$) after passing through valve 1. From this FWH, a distilled flow ($\dot{m}_{23}$) is obtained that is the sum of the condensed flow from the entering steam ($\dot{m}_5$) and the liquid flow that comes from FWH 1 ($\dot{m}_2$). Applying an energy balance through this component, the following equation is obtained:

$$\dot{m}_5 \cdot h_5 + \dot{m}_2 \cdot h_{22} + \dot{m}_1 \cdot h_{18} = \dot{m}_{23} \cdot h_{23} + \dot{m}_1 \cdot h_{19} \tag{4.74}$$

The enthalpies h_{19} and h_{23} are a function of the pressures and temperatures at the corresponding points:

$$h_{19} = f(T_{19}, P_{19})$$

$$h_{23} = f(T_{23}, P_{23})$$

(4.75)

The outlet temperature of the liquid (T_{23}) is determined using the expression:

$$T_{23} = T_{18} + DCA \tag{4.76}$$

The feedwater temperature at the FWH outlet (T_{19}) is given by:

$$T_{19} = T_{\text{sat}}(P_5) - TTD \tag{4.77}$$

This same methodology is used for water heaters 4 and 5 as they work similarly.

Open Feedwater Heaters

Open FWHs use the steam energy extracted from the turbine to heat the feedwater while they are mixing. These types of heaters can also work as deareators, heating the water to a temperature high enough that the gases contained within them (oxygen and non-condensable gases) are released. These gases are released through a trap that is incorporated into the heater. In this FHW, the mixing of the steam flow extracted from turbine ST2 ($\dot{m}_6$) and the feedwater coming from FWH 3 ($\dot{m}_{12}$) takes place. Furthermore, the liquid flow coming from FWH 2 ($\dot{m}_{23}$) enters this heater after passing through valve 2. The mixture obtained ($\dot{m}_1$) leaves the deareator at a higher temperature and at the same pressure as the inlet currents. The energy balance applied through this component is as follows:

$$\dot{m}_6 \cdot h_6 + \dot{m}_{12} \cdot h_{16} + \dot{m}_{23} \cdot h_{24} = \dot{m}_1 \cdot h_{17} \tag{4.78}$$

Because the liquid exiting the deaerator is considered saturated liquid ($x_{17} = 0$), the enthalpy, specific volume and temperature depend on the pressure at this point; as shown below:

$$h_{17} = f(P_{17}, x_{17})$$

$$v_{17} = f(P_{17}, x_{17}) \tag{4.79}$$

$$T_{sat,17} = f(P_{17})$$

Valves

As mentioned before, the valves reduce the liquid pressure to the interior FWH pressure, thus avoiding sudden evaporation when the liquid enters a chamber where the pressure is lower than its corresponding saturation pressure. Moreover, the valves trap steam that might still be present in the condensate coming from the previous heater.

Valve 1

The mass flow of the condensed liquid, $\dot{m}_2$, circulates through valve 1 coming from FWH 1, which enters FWH 2 at a pressure equal to that inside (P_{23}). The energy balance in this valve is given by:

$$\dot{m}_2 \cdot h_{21} = \dot{m}_2 \cdot h_{22} \tag{4.80}$$

The condensed liquid temperature at the valve 1 outlet is a function of the pressure and the enthalpy at this point:

$$T_{22} = f(P_{22}, h_{22}) \tag{4.81}$$

The calculation procedure for the temperature and enthalpy at the outlet of each of the other valves is the same as that explained for valve 1.

Steam Generation System

In this system, heat is transferred from the oil coming from the solar field to the power conversion system, turning the feedwater into superheated steam, which then enters the high pressure turbine (ST1). The thermal power required in the generation system is determined using the equation:

$$P_{PCS} = \dot{m}_1 \cdot (h_1 - h_{20}) \tag{4.82}$$

where h_1 and h_{20} are the specific enthalpies of the liquid at the inlet and of the superheated steam at the system outlet, respectively.

Finally, the thermal cycle efficiency is defined as the ratio between the net electrical power produced by the steam cycle and the nominal thermal power required by the cycle:

$$\eta_{th} = \frac{P_{net}}{P_{th}} \tag{4.83}$$

The net electrical power produced by the steam cycle, P_{net}, is the electrical power produced by the turbine, P_{turb}, minus the electrical consumption of the cycle pumps and the refrigeration system. In other words, the turbine has to produce an additional amount of electricity to compensate for these electricity demands in an established net power production. The electricity consumed by the refrigeration system varies depending on the refrigeration method used (in the equation shown below, it is referred to once-through refrigeration method):

$$P_{net} = P_{turb} - P_{pumps} - P_{pump\_sw} \tag{4.84}$$

On the other hand, the nominal thermal power required by the power cycle, P_{th} is determined as the thermal power required by the power conversion system, P_{PCS}, plus the thermal power required by the cycle reheaters, P_r:

$$P_{\text{th}} = P_{\text{r}} + P_{\text{PCS}} \tag{4.85}$$

The power cycle equations, together with the equations explained in the following chapter (Chap. 5) regarding the integration of desalination plants into a power cycle, provide the model for a dual-purpose solar power/water cogeneration plant. The model of the solar field is used to size the solar field required to supply the thermal power needed by the power and desalination cycle.

References

Blanco-Marigorta, A. M., Sanchez-Henríquez, M. V., & Peña-Quintana, J. A. (2011). Exergetic comparison of two different cooling technologies for the power cycle of a thermal power plant. *Energy, 36*, 1966–1972.

Blanco-Muriel, M., Alarcón-Padilla, D. C., López-Moratalla, T., & Lara-Coira, M. (2001). Computing the solar vector. *Solar Energy, 70*, 431–441.

González, L., Zarza, E., & Yebra, L. (2001). *Determinación del modificador por ángulo de incidencia de un colector solar LS-3, incluyendo las pérdidas geométricas por final de colector. Informe técnico DISS-SC-SF-30*. Almería, Spain: Plataforma Solar de Almería.

Habib, M. A., & Zubair, S. M. (1992). Second-law-based thermodynamic analysis of regenerative-reheat Rankine-cycle power plants. *Energy, 17*, 295–301.

Incropera, F. P., & Dewitt, D. P. (1996). *Fundamentals of heat and mass transfer*. New York: Wiley.

Zarza, E. (2002). *Generación directa de vapor con colectores cilindro parabólicos: Proyecto Direct Solar Steam (DISS)*. Doctoral Thesis. Seville, Spain: Universidad de Sevilla.

Zarza, E. (2004). *Generación directa de vapor con colectores solares cilindro parabólicos: Proyecto Direct Solar Steam (DISS)*. Madrid, Spain: CIEMAT.

Zarza, E., & Ajona, J. I. (1988, September 13–18). Overall thermal loss coefficient and incident angle modifier for an ACUREX 3001 DCS: application to the control system. In W. H. Bloss & F. Pfisterer (Eds.), *Advances in solar energy technology* (Proceedings of the ISES Conference, Hamburg, Germany, Vol. 2, pp. 1649–1653). Oxford, England: Pergamon

Chapter 5
Integration of a Desalination Plant into a Concentrating Solar Power Plant

Nomenclature

Variables

Cr	Thermocompressor compression ratio
$F_{\text{Fw,int}}$	Internal fresh water consumptions in the CSP and Desalination plant (m^3/h)
GOR	Gain output ratio
M_{mv}	Mass flow rate of the motive steam feeding the thermocompressor (kg/s)
M_{s}	Mass flow rate of the steam coming from turbine ST2 that feeds the MED plant (kg/s)
M_{ent}	Mass flow rate of the entrained vapour feeding the thermocompressor (kg/s)
M_{d}	MED plant distillate flow rate (m^3/h)
$M_{\text{d,net}}$	Net fresh water production (m^3/h)
p_{mv}	Motive steam pressure feeding the thermocompressor (kPa)
p_{s}	Compressed steam pressure that comes from the thermocompressor (kPa)
p_{ent}	Entrained vapour pressure that feeds the thermocompressor (kPa)
q_{e}	Heat transfer per unit of mass of the oil in the power cycle (kJ/kg)
q_{s}	Heat transfer per unit of mass of the steam in the power cycle (kJ/kg)
PCF	Steam pressure correction factor of the motive steam feeding the thermocompressor
Ra	Entrainment Ratio
SEC	Specific electricity consumption (kWh/m^3)
TCF	Correction factor of the entrained vapour temperature that feeds the thermocompressor
T_{ent}	Entrained vapour temperature that feeds the thermocompressor (°C)
T_{s}	Steam temperature at the inlet to the heat exchanger tubes of the MED first effect (°C)

P_{desal} Electrical power consumed by the desalination plant (kW_e)
P_{net} Net power production (MW_e)
P_{pumps} Electrical power consumed by the power-cycle pumps (kW_e)
P_{turb} Gross power production (MW_e)
P_{th} Nominal thermal power required by the cycle (MW_{th})
w_e Work per unit of mass realised by the steam over the power cycle (kJ/kg)
w_s Work per unit of mass realised by the steam circulating through the cycle (kJ/kg)

Acronyms

FWH   Feedwater heater
PT-CSP + D   Parabolic-trough concentrating solar power and desalination
LT-MED   Low-temperature multi-effect distillation
LT-MED + TVC   Low temperature multi-effect distillation powered by a thermal vapour compressor
MED   Multi-effect distillation
MED-TVC   Multi-effect distillation with thermal vapour compression
RO   Reverse osmosis
PSA   Plataforma Solar de Almería
ST1   High-pressure turbine
ST2   Low-pressure turbine

5.1   Introduction

This chapter addresses the description and thermodynamic analysis for the integration of desalination plants into the power cycle described in Chap. 4. The systems chosen for this study combine a Concentrating Solar Power plant using parabolic-trough collector technology for electricity generation with various desalination plants, giving rise to what is known as a parabolic-trough concentrating solar power and desalination (PT-CSP + D) plant. The description of the PT-CSP plant, based on the Andasol-1 (Blanco-Marigorta et al., 2011) commercial plant, is detailed in Chap. 4, showing all the model equations. The desalination technologies selected to combine with the PT-CSP plant were multi-effect distillation (MED) and reverse osmosis (RO), as discussed in Chap. 1. On one hand, the simultaneous production of water and electricity using an RO plant connected to a CSP plant seems the simpler option. On the other hand, the integration of a low-temperature MED (LT-MED) plant is an interesting alternative because it allows replacement of the conventional power-cycle condenser by using exhaust steam as the thermal energy source for the desalination plant. However, to satisfy demand, while providing a certain performance, the LT-MED plant inlet temperature should be around 70 °C (corresponding to 0.031 bar absolute), meaning that the steam does not completely expand through the turbine and therefore the power-cycle efficiency

is low compared with a stand-alone electricity-generating plant. This is the reason why another alternative to the MED plant, MED with thermal vapour compression (TVC), is considered. In this case, the steam expands completely in the turbine until it reaches the permitted value for the condenser conditions. However, part of the steam circulating through the turbine is extracted and used as high-pressure steam; this, together with the low-pressure steam coming from one of the MED effects, generates the inlet steam required in the first stage of the desalination plant. Moreover, in this study, a new concept of CSP + MED plants is evaluated (which, until now, has not been studied in published works), a thermally fed LT-MED plant with steam coming from a thermocompressor (LT-MED + TVC). In this case, the low-pressure steam (the entrained vapour) used by the thermocompressor comes from the exhaust steam of a PT-CSP plant instead of one of the MED effects. In each of the systems studied, desalinated water production is evaluated as well as the power and efficiency of the dual thermal solar power and desalinated water cycle.

5.2   Description of the Systems

The following systems are proposed:

- LT-MED plant integrated into a PT-CSP plant (configuration 1)
- LT-MED plant fed by steam coming from a thermocompressor (referred to as LT-MED + TVC), integrated into a PT-CSP plant (configuration 2)
- MED-TVC plant integrated into a PT-CSP plant (configuration 3)
- RO plant connected to a PT-CSP plant (configuration 4)

5.2.1   Configuration 1

The integration of an LT-MED plant into a PT-CSP plant is an attractive prospect because utilisation of the exhaust steam from the turbine as a thermal energy source in the desalination process allows replacement of the CSP refrigeration system. In this way, energy that would otherwise be dissipated through the power-cycle refrigeration system is used for fresh water production, which converts into an added value for the combined system. However, in this case, because the exhaust steam is used to feed the LT-MED plant at 70 °C, it exits at a slightly higher pressure than in the other configurations analysed. This means a reduction in the power-cycle efficiency. A further shortcoming of this configuration is that the desalination plant needs to be situated as close to the turbine as possible because the exhaust steam has a high specific volume and, consequently, a large-diameter pipe is necessary to drive the steam to the desalination plant. This means situating the plant near the coast, where there is generally less direct solar irradiation.

Figure 5.1 shows a flow diagram for this configuration. As observed, in this type of cogeneration system, the LT-MED plant is integrated into the CSP plant, replacing the power-cycle condenser. Given that the final extraction carried out in the power cycle is at a lower temperature than that needed to couple the turbine outlet to the LT-MED plant, only four extractions from the low-pressure turbine (ST2) take place in this cycle instead of the five that occur when complete steam expansion is allowed. Once the steam leaves turbine ST2 (point 1), it is condensed through the first LT-MED plant exchanger, which produces fresh water (point 3) via the evaporation–condensation process. The condensed steam (point 2) mixes with the condensate coming from the feedwater heater, FWH4 (point 5), and the resultant liquid mixture (point 4) is pumped to continue its progress around the power cycle.

5.2.2   Configuration 2

This configuration represents an LT-MED plant fed by the thermal energy from a thermocompressor (the LT-MED + TVC plant). The steam ejector uses steam extracted from the turbine as motive steam and thus, it involves a reduction in the global power production efficiency. Additionally, in this case, complete exhaust steam expansion through the low-pressure turbine (ST2) is permitted, part of this steam being used as entrained vapour in the steam ejector and the remaining exhaust steam is condensed through the power-cycle condenser.

This type of integration is interesting because these energy recovery systems can be used to couple any thermal desalination process to a power cycle with the presence of the condenser, and not only to a MED process. Furthermore, another advantage of this configuration, unlike configuration 1, is that the desalination process does not have to follow the load of the power cycle because of the presence of the PT-CSP plant condenser. Also, an additional advantage is that the condensation of exhaust steam does not depend on operation of the desalination plant which can be a problem in the case of failure in the desalination plant.

With this configuration, in contrast to the conventional MED-TVC process, the MED plant is not coupled to the thermocompressor, because the entrained vapour does not come from the desalination plant but from the power plant. Here, the thermal energy source for the MED process is the compressed vapour (vapour leaving the steam ejector) and not motive steam as in a MED-TVC plant. Thus, the GOR of this plant is the same as for an LT-MED plant and not greater (as in the case of MED-TVC), given that part of the steam generated in the MED process is not recovered.

With respect to the refrigeration needs in the desalination plant, because no steam is extracted from the plant to feed the thermocompressor, all the steam in the last effect has to be condensed in the final condenser. Therefore, the refrigeration requirements are greater than in a MED-TVC plant.

Figure 5.2 shows a diagram of the process flow of configuration 2. As can be observed, the thermocompressor is fed by the motive steam coming from one of the
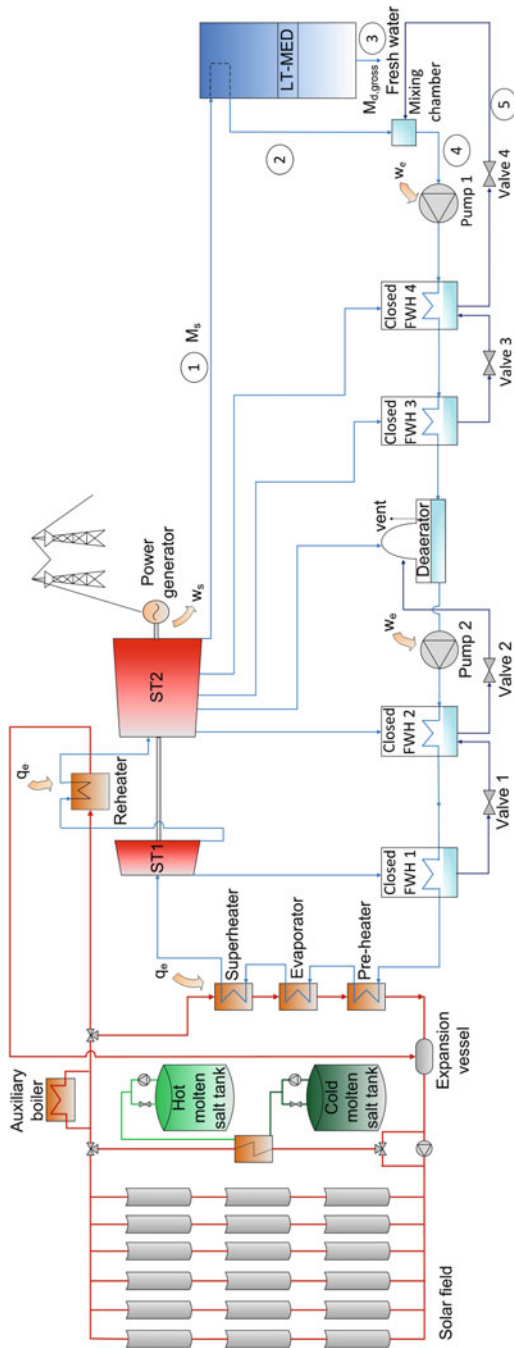
Fig. 5.1 Flow diagram of an LT-MED plant integrated into a PT-CSP plant. Points *1–5* of the process are indicated
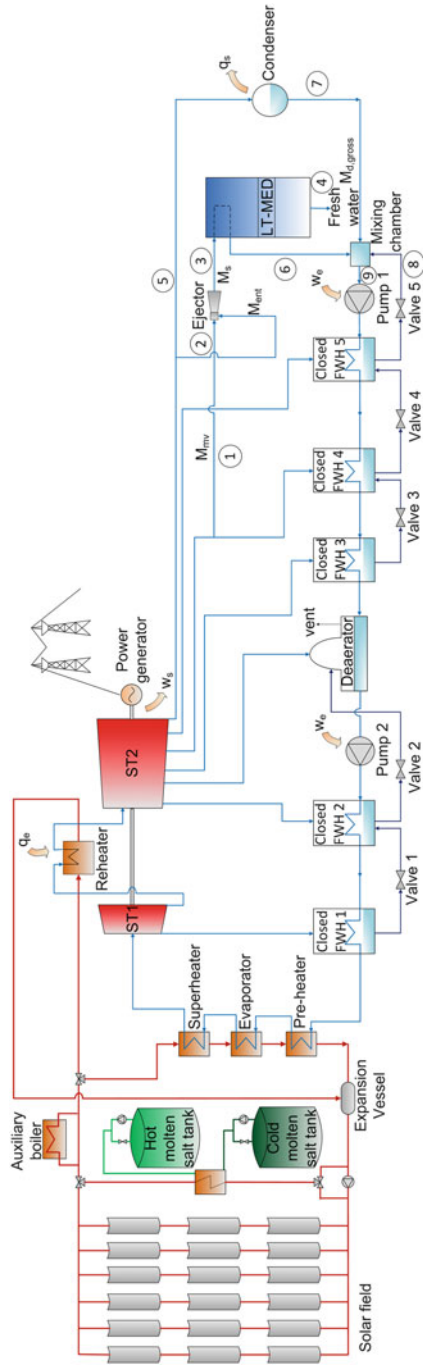
Fig. 5.2 Flow diagram of an LT-MED+TVC plant integrated into a PT-CSP plant using steam extracted from the low-pressure turbine (*ST2*) as motive steam. Points *1–9* of the process are indicated

low-pressure turbine extractions (point 1). Part of the exhaust steam leaving turbine ST2 is used as entrained vapour (point 2). The resulting compressed steam (point 3) is used as a thermal energy source in the LT-MED plant, producing fresh water (point 4). The rest of the exhaust steam that is not used as entrained vapour in the ejector (point 5) is turned into condensate in the power-cycle condenser (point 7), mixing with the liquid condensate that exits the desalination plant first-effect (point 6) and with condensate coming from FWH 5 (point 8). The condensate coming from the mixing chamber (point 9) continues its process in the cycle.

5.2.3   Configuration 3

With the integration of a MED-TVC plant into a PT-CSP plant, complete steam expansion can also take place. The steam condenses in the power-cycle condenser that is not replaced. MED-TVC plant integration into the PT-CSP plant is carried out using high-pressure steam coming from the turbine to feed the thermocompressor, coupled to the MED plant, which consequently diminishes the efficiency of global electricity production. This configuration has the same advantages as configuration 2.

Regarding the distillation unit, the MED-TVC plant has a higher gain output ratio (GOR) than LT-MED plants because less thermal energy is required to produce the same amount of fresh water (part of the steam generated in one of the MED plant effects is recovered). Moreover, the need for refrigeration in these plants is less than in LT-MED plants, given that part of the steam produced in the desalination process is extracted for use in the thermocompressor as entrained vapour and, therefore, less seawater volume is required to condense the steam produced in the last effect of the MED plant.

Figure 5.3 shows a flow diagram of configuration 3. The steam ejector is fed, on the one hand, by steam coming from one of the low-pressure turbine extractions (point 1), called motive steam, and, on the other hand, by steam coming from an intermediate effect of the MED plant (point 2), called entrained vapour. This mixture is introduced into the steam ejector (or thermocompressor), producing steam at an intermediate pressure, called compressed steam (point 3). This compressed steam is introduced into the MED first effect as a thermal energy source to energetically feed the desalination process and thus obtain fresh water (point 4). Using steam from the turbine's fourth extraction ensures that it has the least exergetic content possible and, therefore, does not significantly prejudice the plant's electricity generation. The condensed steam coming from the tube bundle of the MED plant's first effect (point 5) is mixed with the condensate coming from the power-cycle condenser (point 6) and with the condensate from the FWH5 feedwater heater (point 7). The condensate mixture leaves the mixing chamber (point 8) and is pumped to the following feedwater heaters, continuing its way around the power cycle.
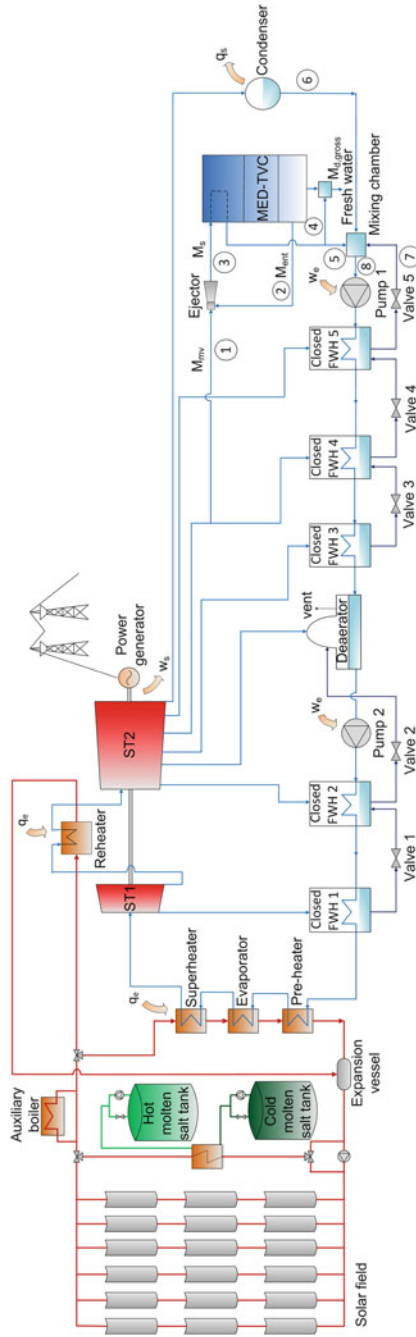
Fig. 5.3 Flow diagram of a MED-TVC plant integrated into a PT-CSP plant using steam extracted from the low-pressure turbine (*ST2*) as motive steam. Points *1–8* of the process are indicated

5.2.4 Configuration 4

This configuration is a basic combination of an RO plant with a PT-CSP plant. It has the advantage over previous configurations of being able to completely separate the desalination process from the electricity-generation process, including geographically. In this case, there are no losses in electricity generation as a result of modifications in the power cycle, as there are in the previous cases. However, because all the steam that leaves the turbine is condensed through the power-cycle condenser, the refrigeration requirements are greater than for configuration 1 (where the need for refrigeration is eliminated completely) and configurations 2 and 3, in which part of the cycle steam is used as motive steam in the thermocompressor (furthermore, in configuration 2, part of the steam leaving the turbine is used as entrained vapour in the thermocompressor).

Figure 5.4 shows the process flow for configuration 4. As can be observed, the electricity generated by the PT-CSP plant (point 1) is used to feed the high-pressure pump, which pumps the seawater through the RO plant membranes (point 2), thus producing desalinated water (point 3).

5.3 Analysis of the Integration of a Desalination Plant into a Power Cycle

This section explains the calculation procedure for desalinated water production from the various desalination plant configurations studied, along with the GOR in the case of thermal distillation plants (LT-MED, MED-TVC and LT-MED + TVC). Furthermore, the electricity-generation calculation is addressed along with the global efficiency of the PT-CSP + D system.

5.3.1 Calculation for Desalinated Water Production and GOR

Low-Temperature Multi-effect Distillation

For the integration of an LT-MED plant into a concentrating solar power plant (Fig. 5.1, configuration 1), fresh water production is determined by taking into account that all the steam flow exiting turbine ST2, M_s, enters the MED plant first effect as a thermal energy source for the desalination process. The total fresh water production from the desalination plant, $M_{d,gross}$, is determined by integrating the LT-MED plant model (which was developed in detail in Chap. 3) into the PT-CSP plant model (explained in Chap. 4).
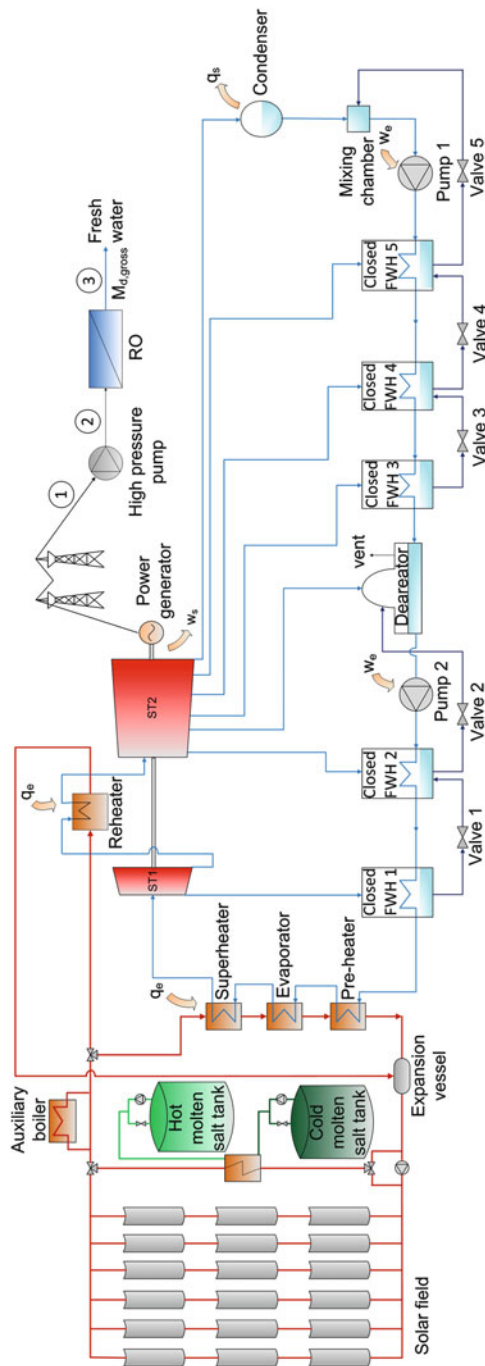
Fig. 5.4 Flow diagram of an RO plant connected to a PT-CSP plant. Points *1–3* of the process are indicated

The parameter that measures the performance of a MED plant working with steam as the thermal energy source is the GOR. This is defined as the kilograms of distillate produced by every mass unit of steam supplied to the distillation plant. Therefore, in the case of the LT-MED plant, it is given by (see Fig. 5.1):

$$\text{GOR} = \frac{M_{\text{d, gross}}}{M_{\text{s}}} \tag{5.1}$$

In all configurations, the net fresh water production ($M_{\text{d,net}}$) is assumed to be the same as in configuration 1, since in this configuration all the steam from the solar power plant is used as the thermal power source in the desalination unit, producing fresh water according to the established thermal efficiency of the distillation plant. On the other hand, the net fresh water production is considered to be slightly lower than the gross ($M_{\text{d,gross}}$), because some of the water produced is consumed internally in the power plant for solar collector mirror cleaning, power block water supply and other internal water consumptions (e.g. drinking water). Also, in the case of evaporative cooling, an additional amount of water must be produced to be used in the evaporative tower:

$$M_{\text{d, net}} = M_{\text{d, gross}} - F_{\text{FW, int}} \tag{5.2}$$

where $F_{\text{Fw,int}}$ is the sum of the fresh water consumed by solar collector mirror cleaning, the power block, the condenser (in case of evaporative cooling) and other internal consumptions (in cubic metres per hour). These are determined considering the specific fresh water consumptions shown in Table 5.1. The values of specific fresh water consumption shown in this table refer to the total power produced by the power and desalination cycle. In the case of mirror washing, the specific fresh water consumption is considered to be 27 L/m^2 year (Richter and Dersch 2009).

MED-TVC and LT-MED + TVC

The LT-MED+TVC and MED-TVC thermal distillation plants are desalination systems integrated into configuration 2 (Fig. 5.2) and configuration 3 (Fig. 5.3), respectively.

The calculation of the GOR varies for each plant, MED-TVC or LT-MED + TVC, as a result of the different thermal energy sources driving the process. In

Table 5.1 Specific fresh water consumptions for the internal water consumed in the power and desalination cycle

	Evaporative water cooling	Power block	Other internal consumptions
Specific fresh water consumption (m^3/MW$_e$h)	3	0.175	0.0029

the case of MED-TVC, the steam supplied to the desalination plant is the motive steam for the ejector, M_{mv}. Thus, the GOR is given as:

$$GOR = \frac{M_{d,gross}}{M_{mv}} \tag{5.3}$$

In the case of the LT-MED + TVC plant (as in a LT-MED plant), the thermal energy supplied to the desalination process is the steam that exits the thermocompressor (compressed steam), M_s, which is not coupled to the MED plant because the entrained vapour used comes from the power cycle instead of from the desalination plant:

$$GOR = \frac{M_{d,gross}}{M_s} \tag{5.4}$$

The equations that determine the steam flow rates in the thermocompressor, as well as the temperatures and pressures in configurations 2 and 3, are given by the thermocompressor model. This model is based on the equations published by El-Dessouky and Ettouney (2002), which used field data from entrainment and compression ratios collected by Power (1994) over a 35-year period. The entrainment ratio is defined as the ratio of the flow rates for the motive steam, M_{mv}, and the entrained vapour, M_{ent}:

$$Ra = \frac{M_{mv}}{M_{ent}} \tag{5.5}$$

This parameter, in turn, is given by the following correlation, proposed by El-Dessouky and Ettouney (2002):

$$Ra = 0.296 \cdot \frac{(p_s)^{1.19}}{(p_{vs})^{1.04}} \cdot \left(\frac{p_{mv}}{p_{ent}}\right)^{0.015} \cdot \left(\frac{PCF}{TCF}\right) \tag{5.6}$$

where p_s, p_{mv} and p_{ent} are the pressures of the resulting steam from the thermocompressor (compressed steam), motive steam and entrained vapour, respectively; PCF is the motive steam pressure correction factor; and TCF is the entrained vapour temperature correction factor, defined by El-Dessouky and Ettouney (2002) as:

$$PCF = 3 \times 10^{-7}(p_{mv})^2 - 0.0009(p_{mv}) + 1.6101 \tag{5.7}$$

$$TCF = 2 \times 10^{-8}(T_{ent})^2 - 0.0006(T_{ent}) + 1.0047 \tag{5.8}$$

where T_{ent} is the temperature of the entrained vapour.

The mass and energy balances through the thermocompressor are given by:

$$M_s = M_{mv} + M_{ent} \tag{5.9}$$

$$h_s \cdot M_s = h_{mv} \cdot M_{mv} + h_{ent} \cdot M_{ent} \tag{5.10}$$

The principle of conservation of energy in the thermocompressor results in a steam temperature at the outlet of the ejector above the 70 °C limit required for the MED plant. Therefore, although not represented explicitly, the use of a desuperheater is required at the thermocompressor outlet.

The compression ratio, Cr, is defined as the ratio of the compressed vapour and the entrained vapour pressures:

$$Cr = \frac{p_s}{p_{ent}} \tag{5.11}$$

All of the above equations are valid within the following ranges:

$$Ra \le 4, \ 500 \ge T_{ent} > 10 \,°C, \ 3500 \ge p_{mv} \ge 100 \text{ kPa and } 6 \ge Cr \ge 1.81.$$

The thermocompressor should be designed and operated under critical conditions to achieve stable and normal operation. This condition is associated with the absence of violent fluctuations in the entrained pressure. A thermocompressor is crucial when the compression ratio is greater or equal to the critical pressure ratio of the entrained vapour. For water vapour, this ratio is 1.81. This means that the entrained pressure has to be less than 0.55-times that of the compressed pressure in order to obtain critical or stable conditions in the steam ejector. The above limit on the compression ratio necessitates the use of two steam jet ejectors in series.

Reverse Osmosis

As mentioned above, in this case, as in configurations 2 and 3, the same net fresh water production, $M_{d,net}$, as that one obtained in configuration 1 is considered. The gross fresh water production, $M_{d,gross}$, is determined using (5.2).

5.3.2   Power and Efficiency Assessment of the Combined CSP and Seawater Desalination Plant

The thermal efficiency of the combined CSP and seawater desalination plant is defined as the ratio between the net power production, P_{net}, and the net output thermal capacity (P_{th}), which is the nominal thermal power that the cycle requires:

$$\eta_{th} = \frac{P_{net}}{p_{th}},$$ (5.12)

The net output thermal capacity is given by:

$$P_{th} = P_{pcs} + P_r$$ (5.13)

where P_{pcs} and P_r are the power required by the power conversion system and the cycle reheaters, respectively.

P_{net} is the gross power production in the turbines minus the power required by the pumps, the desalination plant and the cooling system:

$$P_{net} = P_{turb} - P_{pumps} - P_{desal} - P_{cooling}$$ (5.14)

In all cases, the electrical consumption required by the desalination plant is determined as follows:

$$P_{desal} = SEC \times M_{d, gross}$$ (5.15)

where SEC is the specific electricity consumption required by the desalination plant in each case.

From the model of the combined CSP and seawater desalination plant, a set of computational simulations are conducted to carry out a thermodynamic analysis of the different configurations and, thus, to evaluate the technical feasibility of coupling MED plants to CSP plants under different conditions with respect to the combination of RO with CSP.

References

Blanco-Marigorta, A. M., Sánchez-Henríquez, M. V., & Peña-Quintana, J. A. (2011). Exergetic comparison of two different cooling technologies for the power cycle of a thermal power plant. *Energy, 36*, 1966–1972.

El-Dessouky, H., & Ettouney, H. (2002). *Fundamentals of salt water desalination* (1st ed.). Amsterdam, The Netherlands: Elsevier Science.

Power, B. R. (1994). *Steam jet ejectors for process industries*. New York: McGraw-Hill.

Richter, C., Dersch, J. (2009, September 15–18). *Methods for reducing cooling water consumption in solar thermal power plants*. In: Proceedings of the 15th SolarPACES Conference, Berlin, Germany.

Chapter 6
Techno-economic Analysis

Nomenclature

Cr	Compression ratio
CSP + D	Concentrating solar power and desalination
DNI	Direct normal irradiation (kWh/m^2 year)
EES	Engineering equation solver
GOR	Gain output ratio
LEC	Levelised electricity cost (c€/kWh)
LT-MED	Low temperature multi-effect distillation
LT-MED + TVC	Low temperature multi-effect distillation powered by a thermal vapour compressor
LWC	Levelised water cost (€/m^3)
MENA	Middle East and North Africa
PT	Parabolic trough
Ra	Entrainment ratio
RO	Reverse osmosis
MED-TVC	Multi-effect distillation with thermal vapour compression
P_{net}	Net power production (MW$_e$)
$\dot{m}$	Mass flow rate (kg/s)
F_{FW}	Fresh water flow rate (m^3/day)
P_{cond}	Power consumed by the condenser (MW$_e$)
h	Specific enthalpy (kJ/kg)
P_{th}	Net output thermal capacity (MW$_{th}$)
M_d	Distillate mass flow rate (kg/s)
M_{mv}	Motive steam mass flow rate (kg/s)
M_{ent}	Entrained vapour mass flow rate (kg/s)
η_{th}	Global efficiency
F_{sw}	Seawater flow rate (m^3/day)

$M_{\text{d,net}}$	Net fresh water production (m^3/day)
$M_{\text{d,gross}}$	Gross fresh water production (m^3/day)
P_{turb}	Gross power production (MW$_{\text{e}}$)
A_{a}	Aperture area (m^2)
F_{s}	Solar fraction
crf	Capital recovery factor
K_{invest}	Total investment of the plant (€)
$K_{\text{O\&M}}$	Annual operation and maintenance costs (€)
K_{fuel}	Annual fuel cost (€)
E_{net}	Net electricity delivered to the grid (GWh)
k_{d}	Real debt interest rate (%)
n	Depreciation period (years)
$K_{\text{insurance}}$	Annual insurance rate (%)

6.1 Introduction

This chapter describes a steady-state sensitivity analysis based on a design point, considering each of the four configurations proposed in Chap. 5. This approach deals with a simulation-based analysis that allows estimation of overall efficiency over a wide range of boundary conditions to determine which cogeneration system is the most optimal in terms of capital cost (overall efficiency is directly related to the solar field size required). The analysis was performed for the three existing cooling technologies: once-through, evaporative water cooling and dry air cooling (except for the case in which a low-temperature (LT) multi-effect distillation (MED) unit replaces the condenser in the parabolic-trough concentrating solar power [PT-CSP] plant). The specific electric consumption (SEC) and the exhaust steam temperature were taken as inputs to be varied for a wide range of conditions that cover all the locations between the Mediterranean basin and the Arabian Gulf and match the three cooling systems considered. The simulations were carried out using the models described in Chaps. 3, 4 and 5. The study evaluated in which cases the PT-CSP + MED configurations are more efficient than the PT-CSP + RO configuration. Note that the results given in this chapter are valid only for parabolic-trough solar technology; thus, they could change for a different solar technology. Finally, a detailed techno-economic analysis is described for two representative locations in the Mediterranean basin and the Arabian Gulf, with the aim of determining the most suitable configuration and refrigeration system in each location. Specific operating conditions were established for each location, based on similar studies and information from real plants.

6.2   Sensitivity Analysis

6.2.1   Modelling and Simulation

Both the power cycle and the desalination plant were modelled in a steady state and then integrated to solve the power and desalination (P&D) cycle. The PT-CSP + D systems, whose flow diagrams are shown and explained in Chap. 5, are shown again in Figs. 6.1, 6.2, 6.3 and 6.4, indicating 16 points in the process.

Calculations for the P&D cycle were performed as shown in Fig. 6.5. From the exhaust steam temperature, the procedure consists of iterative calculation of the sizes of the steam turbine and desalination plant. The size of the steam turbine was calculated to meet the required net power generation at design conditions. The size of the desalination plant was determined to satisfy the net fresh water production, as outlined by the computational simulation of configuration 1, where all the steam from the turbine must be condensed in the desalination unit. This establishes the fresh water production according to the thermal efficiency of the distillation plant. The iteration was required because the internal electricity consumption of the various plant components and the fresh water consumed internally in the power plant are dependent on the gross capacities of the CSP and the desalination plant, which are not known at the beginning of the calculation.

Both the power cycle and the desalination plant were modelled and then integrated to solve the P&D cycle. The model of the power cycle was implemented within the Engineering Equation Solver (EES) software environment (Klein et al. 1997). All the components associated with the power cycle (pump, reheater, feedwater heaters [FWHs], valves, heat exchanger, condenser and turbine) were analysed by steady-flow energy and mass transfer equations, as indicated in Chap. 4. The EES software resolves nonlinear equation systems using the Newton–Raphson method by a proper initialisation of the variables. A total of 193 equations are needed to run the model of the power cycle, using as input variables the design and operating parameters detailed below. The output variables are the vapour mass flow rates in the high-pressure turbine (ST1) and low-pressure turbine (ST2); the motive and entrained vapour mass flow rates in the steam ejectors; the condensate mass flow rates flowing through the feedwater heaters and the mixing chambers; the enthalpy of all the streams of the power cycle; the pressure and temperature of the streams whose values are not given in the model; the gross power produced by the turbines; the net output thermal capacity required by the dual cycle and its thermal efficiency; and the internal power and fresh water consumption by the P&D cycle.

The model of the MED plant in the case of configurations 1, 2 and 3 was developed and validated with real data from a pilot MED plant located at the Plataforma Solar de Almería as was indicated in Chap. 3 (Palenzuela et al. 2014).
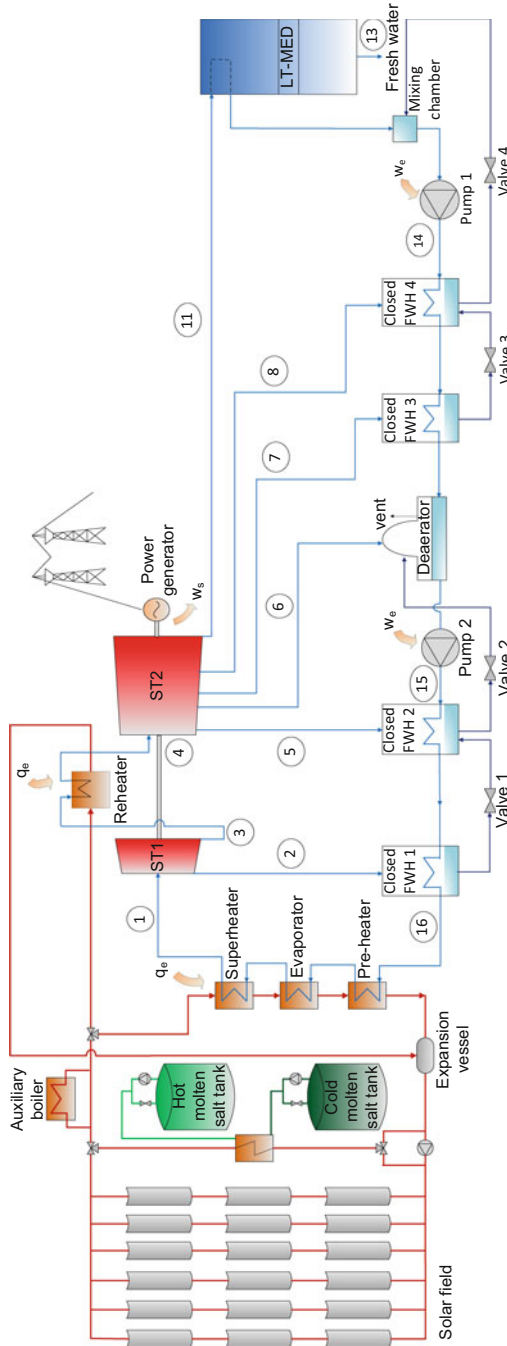
Fig. 6.1 Flow diagram of configuration 1 (PT-CSP+LT-MED)
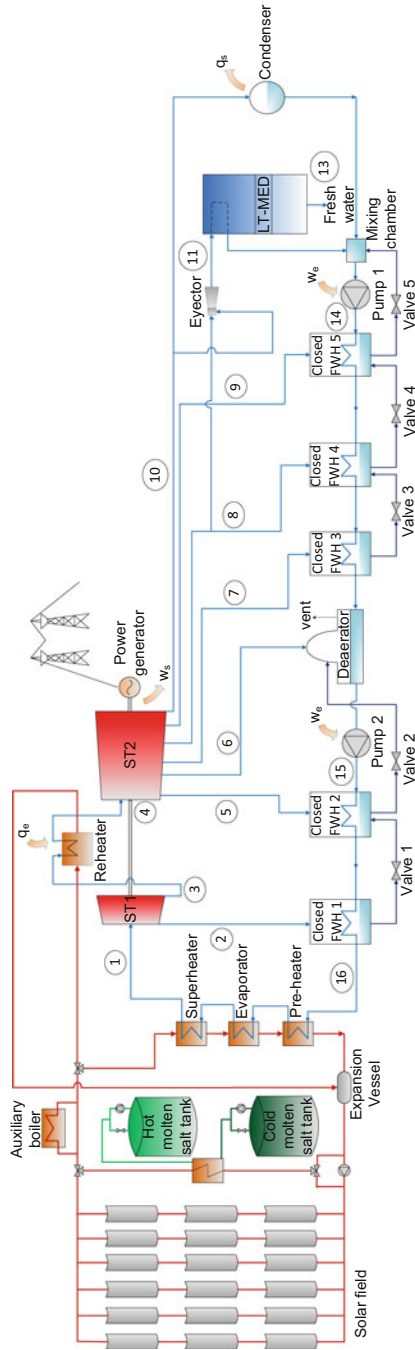
Fig. 6.2 Flow diagram of configuration 2 (PT-CSP+LT-MED+TVC)
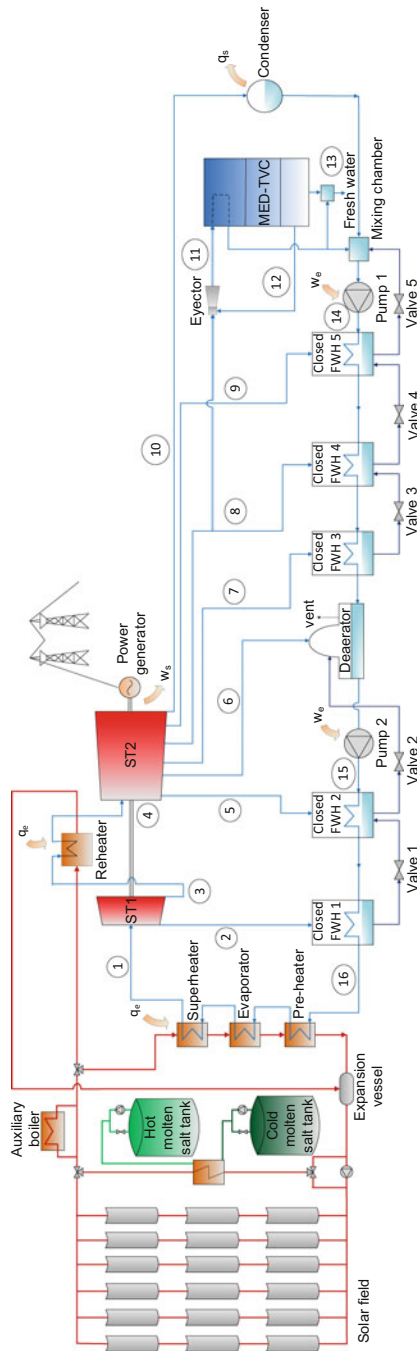
Fig. 6.3 Flow diagram of configuration 3 (PT-CSP+MED-TVC)

Fig. 6.4 Flow diagram of configuration 4 (PT-CSP+RO)
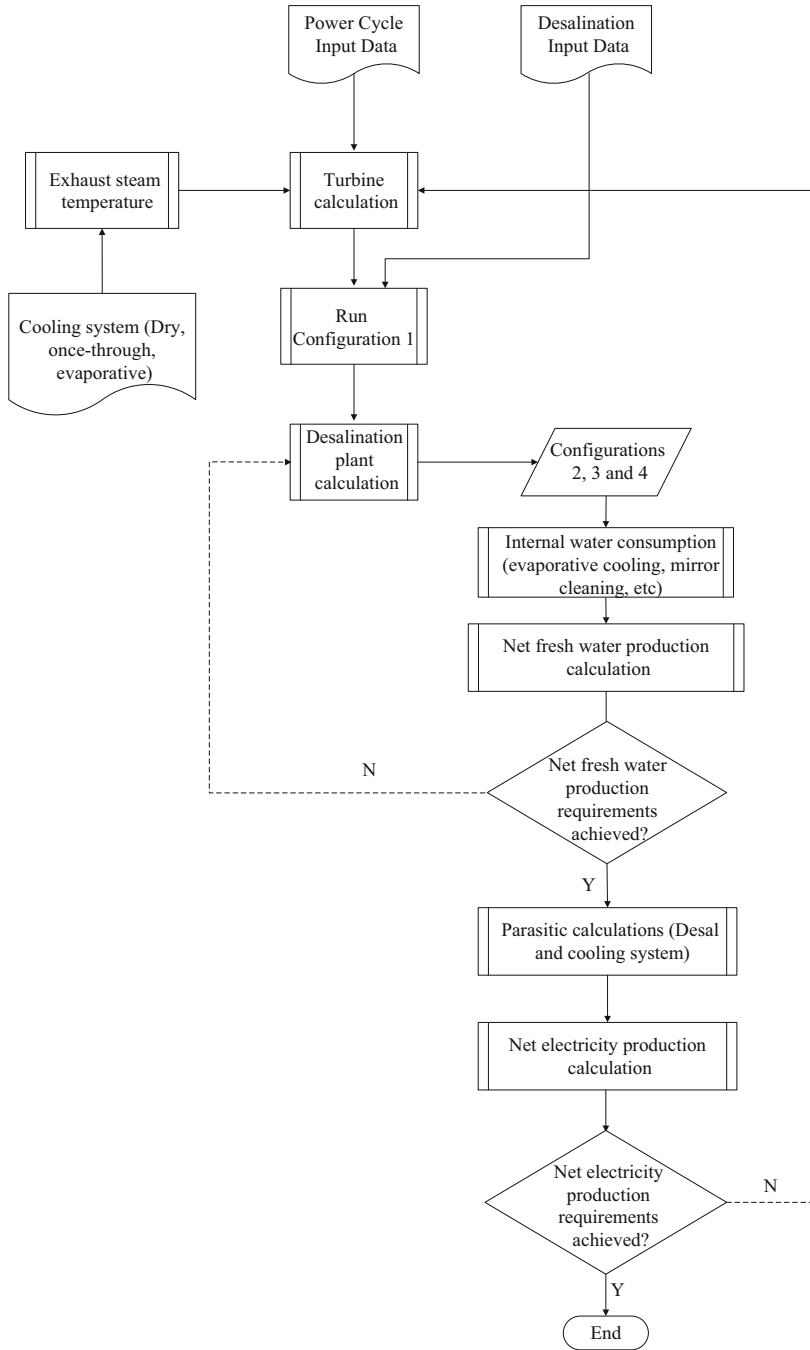
Fig. 6.5 Flow diagram for calculation procedure

Table 6.1 Operation conditions set for the thermodynamic simulation of the systems shown in Figs. 6.1–6.4

Point in the diagram	Parameters	Values
1	Temperature and pressure	373 °C, 100 bar
2	Pressure	33.5 bar
3	Pressure	18.5 bar
4	Temperature and pressure	373.4 °C, 16.5 bar
5	Pressure	14 bar
6	Pressure	6.18 bar
7	Pressure	3.04 bar
8	Pressure	1.17 bar[a]
9	Pressure	0.37 bar
11	Pressure	0.31 bar
12	Pressure	0.18 bar[b]
14	Pressure	8.38 bar
15	Pressure	103 bar

[a]Vapour from the fourth extraction is used, because the lower the motive steam pressure is, the lower the penalty in the overall efficiency of the power cycle. A lower value would be very close to that of steam used to feed the LT-MED unit
[b]The entrained vapour is taken from an intermediate effect of the MED plant

It was implemented within the MATLAB software environment and integrated into the power plant model to run the simulations. As explained in Chap. 5, in the case of MED with TVC, a semi-empirical model developed by El-Dessouky and Ettouney (2002) was additionally used for calculation of the steam ejector mass flow rates (both motive and entrained vapour flow rates). Two important parameters that characterise the steam ejectors are the compression and entrainment ratios (Cr and Ra, respectively). In configuration 3, the compression ratio Cr (the pressure ratio of the compressed and entrained vapours) was kept constant at a value of 1.7. In configuration 2, it varied as a function of the entrained vapour pressure according to the exhaust steam temperature (see Table 6.1). In this case, Cr ranged between 1.8 (for an exhaust steam temperature of 57 °C) and 5.0 (for an exhaust steam temperature of 37 °C). The entrainment ratio Ra (the mass flow rate ratio of the motive and entrained vapours) was constant at a value of 1.4 for configuration 3 and varied between 1.5 (for an exhaust steam temperature of 57 °C) and 4.2 (for an exhaust steam temperature of 37 °C) for configuration 2.

Table 6.1 shows some of the operating conditions taken from the power cycle of the commercial plant Andasol-1 in Spain (Blanco-Marigorta et al. 2011), which were used as input variables for thermodynamic simulation of the P&D cycle.

The cogeneration cycle was modelled assuming that all the components, except the steam ejector, are adiabatic, as no heat losses to the environment were considered. In the steam ejector, saturation conditions were established at the outlet ($x = 1$) so that the vapour at the equilibrium temperature corresponded to the pressure required in the first effect of the MED-TVC and LT-MED + TVC plants.

The saturated vapour is obtained when the superheated steam that leaves the ejector is cooled while passing through a desuperheater located just after the steam ejector (as shown in Figs. 6.2 and 6.3, the steam ejector plus the desuperheater are represented by a unique symbol). Changes in the potential and kinetic energy of fluid streams were assumed to be negligible, as were changes in fluid state between the outlet and the inlet of each component. Pressure losses in the steam lines of the low- and high-pressure FWHs were set to 0.1 bar, and in the feedwater lines of the low and high FWHs were set to 0.1 and 0.5 bar, respectively. Also, pressure losses in the steam generation system (power conversion system) and in the reheater were set to 2 bar. A terminal temperature difference (the difference between the saturation temperature corresponding to the steam inlet pressure and the feedwater outlet temperature) and a drain cooler approach (the difference between drain outlet temperature and feedwater inlet temperature) of 4 °C and 5 °C, respectively, were considered in the FWHs. Isentropic efficiencies of 85.2 and 85 % were set for the high- and low-pressure turbines, respectively, and of 75 % for the pumps included within the cycle. In addition, the following assumptions were made: condensed steam exited the condenser as saturated liquid ($x = 0$) and no pressure losses were set through it; steam was extracted from an intermediate point of the MED-TVC plant as saturated vapour ($x = 1$); condensed steam left the first effect of the MED plants as saturated liquid ($x = 0$); feedwater exited the deaerator as saturated liquid ($x = 0$); and the condensate mixture left the mixing chamber as saturated liquid ($x = 0$).

The net power production of the PT-CSP plant was considered in all configurations to be 50 MW$_e$, which is the normal size of a commercial PT-CSP plant (Geyer et al. 2006). In all the configurations proposed (except PT-CSP + LT-MED, in which the condenser of the power cycle is not required), the sensitivity analysis was carried out for the three cooling technologies: dry cooling, once-through and evaporative water cooling. However, condensation of the vapour generated in the last effect of the MED plants was considered to be carried out by once-through cooling.

The gross power production of the CSP + D plants is higher than the net power production as a result of the power consumed by the pumps, desalination plant and cooling systems. For the cooling systems, the following considerations were taken into account to solve the model:

- For dry cooling, part of the gross electricity production was used to drive the air condensers. The assessment of such consumption was carried out considering a penalty of 5 % in the electricity produced annually (Richter et al. 2009).
- For once-through cooling, part of the gross electricity produced was consumed by the pump that circulates the water from the sea through the condenser, which was determined considering the altitude and distance from the sea of the CSP + D plant. Moreover, a specific seawater flow rate of 87.08 m^3/MW$_e$h (referring

to the total power produced by the power and desalination plant) was taken into account for condensing the exhaust vapour from the turbine (US DoE, 2009).

• For evaporative water cooling, a specific electricity consumption of 0.0329 MW_e/MW was considered (Trieb et al. 2004).

The calculations were first performed for configuration 1 because it determines the net fresh water production that is fixed for the other configurations (point 13 in Figs. 6.1–6.4). For this purpose, as mentioned above, the model of an LT-MED plant explained in Chap. 3 (Palenzuela et al. 2014) was integrated into the power plant model. Two LT-MED plants with different numbers of effects were analysed: a 14-effect LT-MED plant and an 11-effect LT-MED plant. The number of effects was set according to the seawater temperature at the location of interest. The higher the available seawater temperature is, the higher the vapour temperature of the last effect of the MED plant and, therefore, the total number of effects used is lower in order to keep the temperature difference constant between effects (which has a direct impact on the heat exchange area required). Seawater temperatures for the Mediterranean basin and the Arabian Gulf were chosen as 25 and 35 °C, respectively.

A value for GOR, defined as the ratio (in terms of mass flow rate) of distilled water produced, $M_{d,gross}$, to external steam consumed by the desalination process, was obtained from the numerical simulation of this configuration. In the case of the LT-MED plant (configurations 1 and 2), the latter is the steam entering into the first effect of the MED unit, M_s (point 11 in Figs. 6.2 and 6.3), and in the case of the MED-TVC (configuration 3), the external steam is that supplied as motive steam into the ejector, M_{mv} (part of the steam extracted at point 8, Fig. 6.3) (Zarza 1991). Notice that the entrained vapour for the TVC in configuration 3 was taken from effect 8 in the case of the plant with 11 effects and from effect 5 for the 14-effect MED plant. The GOR in each case is defined as follows:

$$GOR_{LT-MED} = \frac{M_{d,gross}}{M_s} \tag{6.1}$$

$$GOR_{MED-TVC} = \frac{M_{d,gross}}{M_{mv}} \tag{6.2}$$

As explained in Chap. 5, the net fresh water production is slightly lower than the gross fresh water production, because part of the water produced is consumed internally within the power plant for solar collector mirror cleaning, water consumption within the power block, etc. Also, in the case of evaporative water cooling, an additional amount of water must be produced to be used in the evaporative tower. The specific fresh water consumptions for the CSP+D plant were indicated in Chap. 5.

6.2.2 Assessment of the Overall Thermal Efficiency

The steady-state sensitivity analysis was carried out to study the effect on the overall efficiency of the system of key parameters of the CSP + D system, such as the specific electric consumption (SEC) of the desalination plants and the exhaust steam temperature. The efficiency is defined by:

$$\eta_{\text{th}} = \frac{P_{\text{net}}}{\dot{m}_1(h_1 - h_{16}) + \dot{m}_3(h_4 - h_3)} \tag{6.3}$$

where P_{net} is the gross power production in the turbines (P_{turb}) minus the power required by the pumps, the desalination plant and the cooling system; $\dot{m}_1$ is the vapour mass flow rate that enters turbine ST1; h_1 is the specific enthalpy of this vapour; h_{16} is the specific enthalpy of the feedwater that enters the preheater of the vapour system generator (composed of preheater, evaporator and superheater); $\dot{m}_3$ is the vapour mass flow rate entering the reheater; and h_4 is the specific enthalpy of the vapour leaving the reheater (note that subscript numbers refer to the points indicated in Figs. 6.1–6.4).

The SEC and the exhaust steam temperatures were varied for a wide range of conditions in order to cover all the locations between the Mediterranean basin and the Arabian Gulf and to match the three cooling systems considered. In both desalination plants, the SEC refers to the internal power consumption for water pumping added to the power consumed for seawater intake, distillate extraction and brine disposal. Black-box values were used for the variable SEC (i.e. no model accounting for dependency on other variables). The SEC of the LT-MED plant was varied in the range 1.4–2.4 kWh/m^3. This is equivalent to assuming a given nominal value for the internal power consumption, considering the different types of engineering used by MED plants manufacturers but adding the pumping of seawater. In the case of the MED-TVC plant, the SEC ranged between 1.2 and 2.2 kWh/m^3, because the nominal value of SEC for this desalination plant is lower due to the lower refrigeration needs in the condenser of the MED-TVC plant (as mentioned in Chap. 5). In the case of the RO plant, the internal power consumption refers mainly to the power consumed by the high pressure pump, which is affected by the salinity of the seawater. The SEC of the RO was varied in a range of 3.5–5.5 kWh/m^3, which reflects the maximum value of 5.5 kWh/m^3 for plants that deal with high salinity seawater (Trieb 2007). The minimum value of 3.5 kWh/m^3 is appropriate for low salinity water and the use of energy recovery devices. Concerning the steam temperature at the outlet of the turbine (point 10 in Figs. 6.1–6.4), a set of different temperatures was considered (37, 42, 47, 52 and 57 °C), which covers a wide range of conditions that match the three cooling systems considered.

The condensing temperature in the cooling system is related to the exhaust steam conditions and to the ambient conditions of the location selected. In the case of dry cooling, the minimum attainable temperature is the dry bulb temperature; thus, low exhaust steam temperatures are usual in places with low ambient temperatures. Therefore, exhaust steam temperatures ranging from 37 to 47 °C are common for

places in the Mediterranean basin, and those between 52 and 57 °C are more suitable for places in the Arabian Gulf. In the case of evaporative water cooling, the minimum attainable temperature is the wet bulb temperature, which depends on the dry bulb temperature and the relative humidity of the location. Thus, low exhaust steam temperatures (between 37 and 47 °C) are more suitable for places in the Mediterranean basin (with low values of the wet bulb temperature) and high exhaust steam temperatures (between 52 and 57 °C) are usual in places within the Arabian Gulf (with high values of relative humidity and dry bulb temperature). In the case of once-through cooling, the minimum attainable temperature is the seawater temperature. Therefore, the higher the exhaust steam temperature, the closer the results are to conditions applicable in the Arabian Gulf (where the seawater temperature is high), and the lower the exhaust steam temperature the closer the results are to conditions in the Mediterranean basin.

6.2.3 Results and Discussion

A comparison was made between the configuration coupled with RO (PT-CSP + RO) and each of the three configurations that integrate MED units in the PT-CSP plant. The same net power production was considered for each configuration, varying the temperature of the exhaust steam and the SEC of the desalination system. From the numerical simulations of configuration 1 for each case, the GOR and the net fresh water production were obtained. For GOR, the following values were achieved: 8.4 for the 11-effect LT-MED plant and 10 for the 14-effect LT-MED plant. The resulting net fresh water production varied as a function of the LT-MED SEC considered: the larger the LT-MED SEC, the larger the gross power of the turbine. This means that when more exhaust steam leaves the turbine more fresh water is obtained from the LT-MED plant. The resulting values ranged between 34,000 and 35,000 m^3/day for the 11-effect LT-MED and between 41,000 and 42,000 m^3/day for the 14-effect LT-MED plant. As mentioned above, the same net fresh water production obtained in this configuration was used in the others for each value of the LT-MED SEC considered in the analysis. Then, the overall efficiency of the dual power and fresh water cycle was obtained for each value of SEC, each value of exhaust steam temperature and each cooling system considered in the PT-CSP plant (except configuration 1, where no cooling system is required).

In the case of the MED-TVC plants, the GORs obtained were 10 and 12 for the 11-effect and 14-effect MED-TVC plants, respectively.

Tables 6.2, 6.3, 6.4, 6.5, 6.6, 6.7, 6.8, 6.9, 6.10, 6.11, 6.12, 6.13, 6.14 and 6.15 (see Appendix) show some of the results of overall thermal efficiency obtained by comparing the cogeneration systems involving thermal desalination with those including reverse osmosis. In all the comparisons, bold values indicate the cases where the overall efficiency of the PT-CSP + MED system is greater than that of the PT-CSP + RO system. Furthermore, an uncertainty propagation analysis was

carried out to calculate how the uncertainties in each of the input variables (exhaust steam temperature and SEC) propagate into the value of the output variable (overall efficiency). The method for determining this uncertainty propagation is described in NIST Technical Note 1297 (Taylor and Kuyatt 1994). Typical uncertainty ranges for industrial temperature and flow measure systems (the flow rate measurement being related directly to the SEC) of 0.85 °C and 0.2 %, respectively, were considered. The absolute errors in the overall efficiencies of the CSP + MED configurations were in the range 0.01–0.05, and in the case of the CSP + RO configuration, the absolute errors varied from 0.05 to 0.1.

From the comparison between the PT-CSP + LT-MED and PT-CSP + RO configurations, for high exhaust steam temperatures, there are two cases where configuration with LT-MED is always better than that with RO. These cases are when dry-cooling and once-through are considered as the cooling methods for the power cycle when connected with RO. When using evaporative water cooling, there is a value of RO SEC (4 kWh/m^3) above which the PT-CSP + LT-MED system is always more efficient than the PT-CSP + RO system.

For low exhaust steam temperatures, the configuration with LT-MED is more competitive only in the case of dry cooling and for very high RO SEC values (above 5 kWh/m^3). However, places with low ambient temperatures (conditions matching the Mediterranean basin) are not likely to have SEC RO as high as 5 kWh/m^3, so in these places the MED configuration is not favourable. For the other cooling systems, most of results are more favourable for the system with RO (see Tables 6.4 and 6.6).

However, when integrating the LT-MED unit into a CSP plant, configuration 1 might not be practical for the reasons explained in Chap. 5. Also, the fully replacement of the condenser in configuration 1 can mean a risk towards the implementation of a CSP + D demonstration plant, since it implies that the power production is entirely dependent on the desalination system. The other two MED configurations (PT-CSP + LT-MED + TVC and PT-CSP + MED-TVC) might be more attractive from the point of view of power plant operation because they are less dependent on the MED plant operation.

Comparing the PT-CSP + LT-MED + TVC and PT-CSP + RO systems, it can be seen that LT-MED + TVC system is an attractive concept only for places with high ambient temperatures where the use of dry cooling is usual [Palenzuela et al. (2011a)]. The results depicted in Table 6.7 show that this system is always more efficient for SEC RO values of 5 kWh/m^3 and above. If once-through or evaporative water cooling are used for high exhaust steam temperatures, only in certain cases of SEC RO and SEC MED (shown in Tables 6.11 and 6.13) is the LT-MED + TVC system better than the system with RO. However for low exhaust steam temperatures, the configuration with RO is always better than the configuration with LT-MED + TVC.

From the comparison between the configuration with RO and that with MED-TVC, it can be seen that there are no cases in which the MED system is better than the RO system, because the penalty in power production of the latter is quite high, as shown by Palenzuela et al. (2011a, b). Only the results obtained for dry cooling are shown as a representative example of this configuration.

Besides the cases in which the integration of LT-MED (configurations 1 and 2) into a CSP plant is preferable to a PT-CSP + RO system, it is important to highlight one advantage of the former configurations with respect CSP + RO, depending on the cooling system used in the power cycle of the latter. In the case of CSP + RO using an evaporative cooling system in the power cycle, the advantage of the CSP + MED system is lower fresh water consumption. In the case of CSP + RO using once-through cooling in the power cycle, the advantage of CSP + MED is lower power consumption. Both statements were proved by results obtained by running the CSP + D models for a case study with a SEC RO of 3.5 kWh/m^3, SEC MED of 1.4 kWh/m^3 and exhaust steam temperature of 37 °C (Tables 6.16 and 6.17). Table 6.16 shows the fresh water flow rate (F_{FW}) needed in the condenser of the power cycle when using evaporative cooling. Table 6.17 shows the power consumed by the condenser (P_{cond}) of the power cycle and of the MED plants when using once-through cooling. These results strengthen the implementation of CSP + MED over CSP + RO even more.

6.3   Case Study

6.3.1   Techno-economic Analysis

The techno-economic analysis was carried out for two specific geographical locations chosen as representative of different regions with widespread development of CSP plants and an increasing water deficit, planned to be mitigated with desalination: Almería, in Spain, and Abu Dhabi, in the United Arab Emirates. Almería receives a high solar irradiation, with a direct normal irradiation (DNI) value of around 1990 kWh/m^2 year, similar to that of the north of Africa and other Mediterranean coastal areas. Abu Dhabi has a DNI of roughly 1925 kWh/m^2 year (Goebel 2010), a value similar to other locations in the Arabian Gulf. The analysis was carried out for the three different cooling technologies: once-through, evaporative water cooling and dry air cooling (except for configuration 1 in which the LT-MED unit replaces the condenser in the PT-CSP plant).

Thermodynamic Analysis

First, the steam temperature at the outlet of the turbine was determined from meteorological data (considering a reference day as the design point) and from the cooling system selected for the analysis. This was followed by the iterative calculation shown in Fig. 6.5.

The steam condensation temperature, T_{ST}, (i.e. the steam temperature at the outlet of the turbine) was established according to the refrigeration method used and the ambient conditions of the location. The lower this temperature is, the higher the

Table 6.18 Ambient conditions at 21st September solar noon for Abu Dhabi and Almería

Location	Ambient temperature (°C)	Direct normal irradiance (W/m²)	Relative humidity (%)
Abu Dhabi	37.1	853	47
Almería	27.1	884	43

Table 6.19 Turbine outlet steam temperatures for each refrigeration method used in the power cycle

	Once-through		Evaporative water cooling		Dry cooling	
	Abu Dhabi	Almería	Abu Dhabi	Almería	Abu Dhabi	Almería
T_{ST} (°C)	45	35	45	37	60	50

power plant efficiency. For both locations, a design point was chosen that would avoid a large difference between summer and winter. If the design point was chosen in summer, the resulting solar field size would be too small to deliver the required thermal power for the power block during winter, when consequently it would work at partial load. By contrast, if the design point was chosen in winter, the larger solar field resulting would be more costly and deliver more thermal power than needed in summer. Taking these considerations into account, the design point chosen was the 21st of September at solar noon. The input variables of solar irradiance and those corresponding to meteorological values of interest at this point are shown in Table 6.18. For each location, the radiation and ambient temperature data were taken from a typical meteorological year using the software Meteonorm. In the particular case of Abu Dhabi, Meteonorm DNI profiles were used but normalised against the real measurement of the annual average of the DNI (1925 kWh/m² year).

In the case of once-through cooling, the temperature difference in the condenser was set at 10 °C, as usually established by environmental regulations. An average value of the seawater temperature was taken for both locations on the basis of published data from commercial desalination plants in the corresponding regions (Trieb 2007), namely, 35 °C for Abu Dhabi and 25 °C for Almería. In evaporative cooling, the temperature difference is obtained by addition of three different factors: the tower approach (the difference between the cooling tower outlet and the wet bulb temperature), the cooling tower range (the difference between the cooling tower inlet and the cooling tower outlet) and the difference between the inlet and outlet temperature in the condenser. The data taken from Andasol-1 plant (Blanco-Marigorta et al. 2011) were 7 °C, 8 °C and 3 °C, respectively. For dry cooling, the temperature differential in the aero-condenser was considered to be 22 °C, based on the average values from a report disseminated by the U.S. Department of Energy (US DoE 2009). The resulting T_{ST} values at point 10 in configurations 2, 3 and 4 are shown in Table 6.19.

The rest of the input variables corresponding to the operating conditions used for the simulation of the P&D cycle are shown in Table 6.1. As in the sensitivity analysis, the calculation was first performed for configuration 1. In addition to the fresh water production, the GOR associated with this production was obtained from the computational simulation of configuration 1. The number of effects of the MED plant was set according to the seawater temperature of each location. For Almería, a 14-effect MED plant was selected, whereas an 11-effect MED plant was considered in the case of Abu Dhabi. As mentioned in Sect. 6.2.3, the GOR values for the 11-effect and 14-effect LT-MED plants were 8.4 and 10, respectively, and 10 and 12 for the 11-effect and 14-effect MED-TVC plants, respectively. The net fresh water production obtained in configuration 1 was 35,607 m^3/day for Abu Dhabi, and 42,927 m^3/day for Almería.

For calculating the power required by the desalination plant, an SEC of 1.5 kWh/m^3 of distillate production was assumed in the case of the MED plant for both locations (Trieb 2007). For the RO, a value of 3 kWh/m^3 was chosen for Almería and 4 kWh/m^3 for Abu Dhabi, taking into account the different conditions of salinity and temperature of the raw seawater (Trieb 2007). The power consumptions described above only refer to the internal consumptions of the desalination processes and do not take into account the pumping of feedwater from the sea to the desalination plants, nor the pumping of cooling seawater for the condenser of the MED plant. These latter power consumptions were calculated assuming that the desalination plants are located close to the CSP plant at an altitude of 150 m above sea level and a distance from the sea of about 60 km. This assumption was based on the commercial CSP located closest to the sea (Shams 1 in Abu Dhabi) and avoids the problems of a lower DNI and a saline environment that could damage the parabolic-trough mirrors.

Once the P&D cycle was solved, the solar field size was determined by considering the net output thermal capacity required by the cycle. The collectors were Eurotrough type with the following dimensions and characteristics: aperture area of 817.5 m^2, 150 m total gross length and a peak optical efficiency of 80 %. The heat transfer fluid circulating through the absorber tubes of the collectors was thermal oil, namely Monsanto VP-1, whose maximum operational temperature is 400 °C. The model of the solar field was implemented in MATLAB, taking into account the collector's thermal losses, its efficiency curve and the corresponding energy and mass balances shown in Chap. 4. In order to analyse the annual solar contribution for the selected design point, the annual solar fraction (defined as the percentage of the thermal power requirement that is provided by the solar field) was calculated. For this purpose, an annual simulation program was developed and implemented in MATLAB for a typical meteorological year in each location.

The simulations of the P&D cycle produced values for thermodynamic parameters such as the thermal power required, overall efficiency and the solar field size required.

Table 6.20 Economic values for the calculation of LEC and LWC

	Values
Hours thermal energy storage	6.5 h
Plant availability (power and desalination plants)	96 %
Land preparation and infrastructure	15 $/m^2
Solar collector	150 $/m^2
Heat transfer fluid and hydraulic circuit	90 $/m^2
Thermal storage system	35 $/kW$_{th}$h
Power block	1,000,000 $/MW$_{gross}$
Auxiliary gas burner	60 $/kW$_{th}$
Reverse osmosis plant	1207 $/(m^3/day)[a]
Multi-effect distillation plant	1230 $/(m^3/day)[a]

[a]IDA (2013)

Economic Analysis

The economic model calculates the electricity and water costs of the proposed configurations. The following definition of levelised electricity cost (LEC) was used (Short et al. 1995):

$$\text{LEC} = \frac{\text{crf} \times K_{\text{invest}} + K_{\text{O\&M}} + K_{\text{fuel}}}{E_{\text{net}}} \qquad (6.4)$$

where K_{invest} is the total investment in the plant, $K_{\text{O\&M}}$ are the annual operation and maintenance costs, K_{fuel} is the annual fuel cost (only applicable in the case of solar energy with backup), E_{net} is the annual net electricity delivered to the grid and crf is the capital recovery factor. The crf is calculated from:

$$\text{crf} = \frac{k_{\text{d}}(1 + k_{\text{d}})^n}{(1 + k_{\text{d}})^n - 1} + K_{\text{insurance}} \qquad (6.5)$$

where k_{d} (6.5 %) is the real debt interest rate, n is the depreciation period in years (20 years) and $K_{\text{insurance}}$ is the annual insurance rate (1 %).

A similar procedure was used for estimation of the levelised water cost (LWC). Table 6.20 shows the values used for the input variables, which were based on data published by the National Renewable Energy Laboratory (NREL 2010) and personal communication from CSP experts (Zarza, personal communication). The area of the solar field obtained from the technical analysis was used as input variable for the economic analysis.

6.3.2   Results and Discussion

The results of the simulations are shown in Tables 6.21 and 6.22, which list the most relevant parameters of the P&D cycle and the solar field in each configuration. The most important parameters for thermodynamic characterisation of the P&D cycle are the thermal power required by the P&D cycle (P_{th}) and the global efficiency of the P&D cycle (η_{th}). The size of the solar field (A_a) is a function of the thermal power required by the cycle. The solar fraction (F_s), which is defined as the relation between the amount of energy obtained through the solar technology used and the total annual energy required by the P&D cycle, provides information about the annual solar contribution for this design. Also shown in the case of configurations 2 and 3 are the steam mass flow rates needed in the ejector M_{mv} and M_{ent}, which give an idea of the power production penalty as a result of using steam from the low-pressure turbine. Regarding the cooling system, Tables 6.21 and 6.22 show the fresh water flow rate consumed in the evaporative tower (F_{Fw}) and the seawater flow rate circulating through the once-through cooling system of the power plant (F_{sw}). Also indicated are the gross power (P_{turb}) and fresh water production ($M_{d,gross}$). Finally, the levelised electric cost (LEC) and the levelised water cost (LWC) are displayed for each case.

The results obtained for Abu Dhabi (Table 6.21) show that the integration of a LT-MED unit into a CSP plant is the most efficient option thermodynamically. The reduction in power cycle efficiency resulting from preventing the expansion of exhaust steam to a lower pressure (configuration 1) was less than that caused by using high-pressure steam from the turbine to feed the steam ejector (configurations 2 and 3). A more interesting result is the fact that coupling with LT-MED through thermocompression (configuration 2) was also more efficient thermodynamically and in terms of electricity cost than the combination with RO (configuration 4) when using dry cooling in the power cycle (28.41 % overall efficiency of configuration 2 compared with 27.58 % of configuration 4; 17.96 c€/kWh LEC of configuration 2 and 18.97 c€/kWh of configuration 4), which is the most frequent condensation process selected in the Arabian Gulf (Goebel 2010).

With respect to the economic results, configuration 1 was also more favourable for all cases in terms of electricity costs (LEC) mainly as a result of the extra power that the CSP must generate for the cooling system in the other configurations. As seen in Table 6.21, a gross power of 63.59 MW$_e$ must be produced in the case of configuration 4 with dry cooling compared with 55.36 MW$_e$ for configuration 1. This means an increase of about 14 % in the LEC. In the case of water costs (LWC), configuration 4 performed the best as a result of the lower investment costs of RO, except in the case of evaporative cooling. Using this refrigeration method, an additional fresh water flow rate of 4462 m³/day was needed in the evaporative tower, which required a desalination plant 11 % larger. The difference between the LWC in configuration 4 with respect to configurations 1 and 2 was not that high (less than 5 %) and might not be a strong enough reason for choosing configuration 4, especially considering the further challenges that RO desalination can have in the

Table 6.21 Results obtained from the techno-economic analysis in Abu Dhabi

	Units	Conf. 1	Conf. 2 (dry)	Conf. 2 (evap.)	Conf. 2 (once)	Conf. 3 (dry)	Conf. 3 (evap.)	Conf. 3 (once)	Conf. 4 (dry)	Conf. 4 (evap.)	Conf. 4 (once)
η_{th}	[–]	30.41	28.41	28.05	26.42	26.13	26.33	24.46	27.58	29.65	26.86
P_{th}	MW_{th}	164	176	178	189	191	190	204	181	169	186
F_{Fw}	m³/day	n/a	n/a	341	n/a	n/a	4043	n/a	n/a	4462	n/a
F_{sw}	m³/day	n/a	n/a	n/a	33,524	n/a	n/a	133,524	n/a	n/a	145,228
M_{ent}	kg/s	n/a	21.72	13.38	13.26	29.68	33.01	29.71	n/a	n/a	n/a
M_{mv}	kg/s	n/a	27.44	36.25	35.93	41.32	45.95	41.36	n/a	n/a	n/a
$M_{d,gross}$	m³/day	35,950	35,959	36,301	35,985	35,979	40,016	36,012	35,997	40,448	36,025
P_{turb}	MW_e	55.36	55.76	55.65	59.89	58.03	57.05	63.89	63.59	62.95	69.49
A_a	m²	807,690	866,550	876,360	931,950	941,760	935,220	1,007,160	892,710	830,580	915,600
F_s	[–]	53.96	54.11	54.02	54.09	54.07	54.10	54.13	54.09	54.11	54.13
LEC	c€/kWh	16.58	17.96	17.73	18.95	19.46	18.76	20.38	18.97	17.40	19.22
LWC	€/m³	0.83	0.83	0.92	0.83	0.83	0.91	0.83	0.79	0.88	0.79

Table 6.22 Results obtained from the techno-economic analysis in Almería

	Units	Conf. 1	Conf. 2 (dry)	Conf. 2 (evap.)	Conf. 2 (once)	Conf. 3 (dry)	Conf. 3 (evap.)	Conf. 3 (once)	Conf. 4 (dry)	Conf. 4 (evap.)	Conf. 4 (once)
η_{th}	[–]	30.02	27.86	27.32	25.49	26.14	26.27	24.48	28.92	30.85	27.95
P_{th}	MW$_{th}$	167	179	183	196	191	190	204	173	162	179
F_{Fw}	m^3/day	n/a	n/a	444	n/a	n/a	4084	n/a	n/a	4424	n/a
F_{sw}	m^3/day	n/a	n/a	n/a	48,054	n/a	n/a	134,798	n/a	n/a	145,109
M_{ent}	kg/s	n/a	16.16	9.65	8.70	29.82	32.63	29.85	n/a	n/a	n/a
M_{mv}	kg/s	n/a	33.64	40.67	41.13	41.51	45.43	41.55	n/a	n/a	n/a
$M_{d,gross}$	m^3/day	43,274	43,285	43,730	43,317	43,301	47,380	43,335	43,310	47,723	43,340
P_{turb}	MW$_e$	56.08	56.50	56.44	61.49	58.62	57.62	64.50	63.24	62.42	69.43
A_a	m^2	752,100	810,960	827,310	886,170	863,280	860,010	922,140	781,530	732,480	807,690
F_s	[–]	47.52	47.56	47.59	47.55	46.32	47.55	47.52	47.59	47.58	47.52
LEC	c€/kWh	18.73	20.35	20.24	21.79	21.69	20.95	22.69	20.37	18.79	20.78
LWC	€/m^3	0.96	0.96	1.05	0.96	0.96	1.05	0.96	0.92	1.01	0.92

Arabian Gulf, such as red algae blooms and problems derived from the high seawater salinity. Therefore, integration of LT-MED in the CSP plant could be preferable in the Arabian Gulf. However, regarding the reluctance of the CSP industry to fully eliminate the condenser of the power cycle (configuration 1), the good results from configuration 2 with dry cooling confirm that it is a good alternative. A further advantage of this configuration is that it offers the possibility of better adaptation to the yearly electricity and water demand curves, because the desalination plant is the same as in configuration 1, the LT-MED could be connected in such a way to facilitate switching between the thermocompression mode (configuration 2) and direct use of exhaust steam (configuration 1).

In the case of Almería (Table 6.22), the ambient conditions allow the exhaust steam from the turbine to expand to lower pressures. This improvement in the power generation efficiency compensates for the extra power consumed by the condenser and the higher electricity consumption by the RO in configuration 4 with respect to the LT-MED. The evaporative cooling enables even lower exhaust steam pressures and lower electricity consumption in the condenser, which makes configuration 4 with this refrigeration method better thermodynamically than configuration 1 (the overall efficiency of the latter was 30.02 % compared with 30.85 % of the former). The difference with respect to electricity costs was negligible in this case (0.3 %) and the LWC values were slightly more favourable for LT-MED (the RO plant was 9 % larger to supply the additional fresh water needed in the evaporative tower). For the remaining cases, configuration 1 performed better than configuration 4 from a thermodynamic point of view, as a result of full replacement of the condenser and thus elimination of the additional power consumed by the cooling system. The extra power that should be produced in configuration 4 for once-through and dry cooling was reflected by a 10 % increase in the LEC. However, the LWC values were slightly improved (4 % lower) for configuration 4 with these refrigeration methods compared with configuration 1.

At these lower steam outlet pressures, configurations 2 and 3 were also more strongly penalised with respect to configuration 4. For Almeria, unlike Abu Dhabi, there were no cases in which configuration 2 gave better results than configuration 4. In the case of dry cooling, configuration 4 had a global efficiency 4 % higher than configuration 2. The costs were very similar, the difference in the LEC being negligible (less than 1 %) and the LWC of configuration 4 being 4 % lower than for configuration 2.

Because the only case that can be more favourable thermodynamic and economically with respect to configuration 4 implies the full replacement of the condenser (configuration 1), it seems more realistic for the Mediterranean basin to opt for the combination of CSP with RO. However, for cooling systems other than evaporative cooling, the differences are not so large and configuration 2 could be contemplated as an option. Improvements in the investment cost or the efficiency of the LT-MED unit could help counterbalance this scenario.

Appendix

Table 6.2 Overall efficiencies of the systems PT-CSP + LT-MED and PT-CSP + RO at an exhaust steam temperature of 37 °C, considering dry cooling as the cooling method

SEC LT-MED (kWh/m^3)	SEC RO (kWh/m^3)									
	3.5		4		4.5		5		5.5	
	LT-MED	RO	LT-MED	RO	LT-MED	RO	LT-MED	RO	LT-MED	RO
1.4	31.5	31.9	**31.5**	**31.4**	**31.5**	**30.9**	**31.5**	**30.5**	**31.5**	**30.0**
1.6	31.3	31.9	31.3	31.4	**31.3**	**30.9**	**31.3**	**30.5**	**31.3**	**30.0**
1.8	31.1	31.9	31.1	31.4	**31.1**	**30.9**	**31.1**	**30.4**	**31.1**	**30.0**
2.0	30.9	31.8	30.9	31.3	30.9	30.9	**30.9**	**30.4**	**30.9**	**30.0**
2.2	30.7	31.8	30.7	31.3	30.7	30.8	**30.7**	**30.4**	**30.7**	**29.9**
2.4	30.5	31.8	30.5	31.3	30.5	30.8	**30.5**	**30.3**	**30.5**	**29.9**

Table 6.3 Overall efficiencies of the systems PT-CSP + LT-MED and PT-CSP + RO at an exhaust steam temperature of 57 °C, considering dry cooling as the cooling method

SEC LT-MED (kWh/m^3)	SEC RO (kWh/m^3)									
	3.5		4		4.5		5		5.5	
	LT-MED	RO	LT-MED	RO	LT-MED	RO	LT-MED	RO	LT-MED	RO
1.4	**31.8**	**29.9**	**31.8**	**29.5**	**31.8**	**29.2**	**31.8**	**28.8**	**31.8**	**28.4**
1.6	**31.6**	**29.9**	**31.6**	**29.5**	**31.6**	**29.1**	**31.6**	**28.8**	**31.6**	**28.4**
1.8	**31.4**	**29.9**	**31.4**	**29.5**	**31.4**	**29.1**	**31.4**	**28.7**	**31.4**	**28.4**
2.0	**31.2**	**29.9**	**31.2**	**29.5**	**31.2**	**29.1**	**31.2**	**28.7**	**31.2**	**28.4**
2.2	**31.0**	**29.9**	**31.0**	**29.5**	**31.0**	**29.1**	**31.0**	**28.7**	**31.0**	**28.3**
2.4	**30.9**	**29.8**	**30.9**	**29.4**	**30.9**	**29.1**	**30.9**	**28.7**	**30.9**	**28.3**

Table 6.4 Overall efficiencies of the systems PT-CSP + LT-MED and PT-CSP + RO at an exhaust steam temperature of 37 °C, considering evaporative water cooling as the cooling method

SEC LT-MED (kWh/m^3)	SEC RO (kWh/m^3)									
	3.5		4		4.5		5		5.5	
	LT-MED	RO	LT-MED	RO	LT-MED	RO	LT-MED	RO	LT-MED	RO
1.4	31.5	33.5	31.5	32.9	31.5	32.4	31.5	31.9	**31.5**	**31.3**
1.6	31.3	33.5	31.3	32.9	31.3	32.4	31.3	31.8	31.3	31.3
1.8	31.1	33.4	31.1	32.9	31.1	32.3	31.1	31.8	31.1	31.3
2.0	30.9	33.4	30.9	32.8	30.9	32.3	30.9	31.8	30.9	31.2
2.2	30.7	33.4	30.7	32.8	30.7	32.3	30.7	31.7	30.7	31.2
2.4	30.5	33.4	30.5	32.8	30.5	32.2	30.5	31.7	30.5	31.2

Table 6.5 Overall efficiencies of the systems PT-CSP + LT-MED and PT-CSP + RO at an exhaust steam temperature of 57 °C, considering evaporative water cooling as the cooling method

SEC LT-MED (kWh/m^3)	SEC RO (kWh/m^3)									
	3.5		4		4.5		5		5.5	
	LT-MED	RO	LT-MED	RO	LT-MED	RO	LT-MED	RO	LT-MED	RO
1.4	**31.8**	**31.4**	**31.8**	**30.9**	**31.8**	**30.5**	**31.8**	**30.1**	**31.8**	**29.7**
1.6	**31.6**	**31.4**	**31.6**	**30.9**	**31.6**	**30.5**	**31.6**	**30.1**	**31.6**	**29.6**
1.8	**31.4**	**31.4**	**31.4**	**30.9**	**31.4**	**30.5**	**31.4**	**30.0**	**31.4**	**29.6**
2.0	31.2	31.3	**31.2**	**30.9**	**31.2**	**30.4**	**31.2**	**30.0**	**31.2**	**29.6**
2.2	31.0	31.3	**31.0**	**30.9**	**31.0**	**30.4**	**31.0**	**30.0**	**31.0**	**29.6**
2.4	30.9	31.3	**30.9**	**30.8**	**30.9**	**30.4**	**30.9**	**30.0**	**30.9**	**29.5**

Table 6.6 Overall efficiencies of the systems PT-CSP + LT-MED and PT-CSP + RO at an exhaust steam temperature of 37 °C, considering once-through as the cooling method

SEC LT-MED (kWh/m^3)	SEC RO (kWh/m^3)									
	3.5		4		4.5		5		5.5	
	LT-MED	RO	LT-MED	RO	LT-MED	RO	LT-MED	RO	LT-MED	RO
1.4	31.5	33.1	31.5	32.6	31.5	32.1	31.5	31.6	**31.5**	**31.2**
1.6	31.3	33.1	31.3	32.6	31.3	32.1	31.3	31.6	**31.3**	**31.1**
1.8	31.1	33.0	31.1	32.5	31.1	32.0	31.1	31.6	31.1	31.1
2.0	30.9	33.0	30.9	32.5	30.9	32.0	30.9	31.5	30.9	31.1
2.2	30.7	33.0	30.7	32.5	30.7	32.0	30.7	31.5	30.7	31.0
2.4	30.5	33.0	30.5	32.4	30.5	31.9	30.5	31.5	30.5	31.0

Table 6.7 Overall efficiencies of the systems PT-CSP + LT-MED and PT-CSP + RO at an exhaust steam temperature of 57 °C, considering once-through as the cooling method

SEC LT-MED (kWh/m^3)	SEC RO (kWh/m^3)									
	3.5		4		4.5		5		5.5	
	LT-MED	RO	LT-MED	RO	LT-MED	RO	LT-MED	RO	LT-MED	RO
1.4	**31.8**	**31.0**	**31.8**	**30.6**	**31.8**	**30.2**	**31.8**	**29.9**	**31.8**	**29.5**
1.6	**31.6**	**31.0**	**31.6**	**30.6**	**31.6**	**30.2**	**31.6**	**29.8**	**31.6**	**29.5**
1.8	**31.4**	**31.0**	**31.4**	**30.6**	**31.4**	**30.2**	**31.4**	**29.8**	**31.4**	**29.4**
2.0	**31.2**	**31.0**	**31.2**	**30.6**	**31.2**	**30.2**	**31.2**	**29.8**	**31.2**	**29.4**
2.2	31.0	31.0	**31.0**	**30.6**	**31.0**	**30.2**	**31.0**	**29.8**	**31.0**	**29.4**
2.4	30.9	30.9	**30.9**	**30.5**	**30.9**	**30.1**	**30.9**	**29.7**	**30.9**	**29.4**

Table 6.8 Overall efficiencies of the systems PT-CSP + LT-MED + TVC and PT-CSP + RO at an exhaust steam temperature of 37 °C, considering dry cooling as the cooling method

SEC LT-MED + TVC (kWh/m³)	SEC RO (kWh/m³)									
	3.5		4		4.5		5		5.5	
	LT-MED + TVC	RO	LT-MED + TVC	RO	LT-MED + TVC	RO	LT-MED + TVC	RO	LT-MED + TVC	RO
1.4	28.7	31.9	28.7	31.4	28.7	30.9	28.7	30.5	28.7	30.0
1.6	28.5	31.9	28.5	31.4	28.5	30.9	28.5	30.5	28.5	30.0
1.8	28.3	31.9	28.3	31.4	28.3	30.9	28.3	30.4	28.3	30.0
2.0	28.1	31.8	28.1	31.3	28.1	30.9	28.1	30.4	28.1	30.0
2.2	27.9	31.8	27.9	31.3	27.9	30.8	27.9	30.4	27.9	29.9
2.4	27.7	31.8	27.7	31.3	27.7	30.8	27.7	30.3	27.7	29.9

Table 6.9 Overall efficiencies of the systems PT-CSP + LT-MED + TVC and PT-CSP + RO at an exhaust steam temperature of 57 °C, considering dry cooling as the cooling method

SEC LT-MED + TVC (kWh/m³)	SEC RO (kWh/m³)									
	3.5		4		4.5		5		5.5	
	LT-MED + TVC	RO	LT-MED + TVC	RO	LT-MED + TVC	RO	LT-MED + TVC	RO	LT-MED + TVC	RO
1.4	29.7	29.9	**29.7**	**29.5**	**29.7**	**29.2**	**29.7**	28.8	**29.7**	**28.4**
1.6	29.5	29.9	29.5	29.5	**29.5**	**29.1**	29.5	28.8	29.5	**28.4**
1.8	29.3	29.9	29.3	29.5	**29.3**	**29.1**	29.3	28.7	29.3	**28.4**
2.0	29.2	29.9	29.2	29.5	**29.2**	**29.1**	29.2	28.7	29.2	**28.4**
2.2	29.0	29.9	29.0	29.5	29.0	29.1	**29.0**	28.7	**29.0**	**28.3**
2.4	28.8	29.8	28.8	29.4	28.8	29.1	**28.8**	28.7	**28.8**	**28.3**

Table 6.10 Overall efficiencies of the systems PT-CSP + LT-MED + TVC and PT-CSP + RO at an exhaust steam temperature of 37 °C, considering evaporative water cooling as the cooling method

SEC LT-MED + TVC (kWh/m³)	SEC RO (kWh/m³)									
	3.5		4		4.5		5		5.5	
	LT-MED + TVC	RO	LT-MED + TVC	RO	LT-MED + TVC	RO	LT-MED + TVC	RO	LT-MED + TVC	RO
1.4	28.8	33.5	28.8	32.9	28.8	32.4	28.8	31.9	28.8	31.3
1.6	28.6	33.4	28.6	32.9	28.6	32.4	28.6	31.8	28.6	31.3
1.8	28.4	33.4	28.4	32.9	28.4	32.3	28.4	31.8	28.4	31.3
2.0	28.1	33.4	28.1	32.8	28.1	32.3	28.1	31.8	28.1	31.2
2.2	28.0	33.4	28.0	32.8	28.0	32.3	28.0	31.7	28.0	31.2
2.4	27.8	33.4	27.8	32.8	27.8	32.2	27.8	31.7	27.8	31.2

Table 6.11 Overall efficiencies of the systems PT-CSP + LT-MED + TVC and PT-CSP + RO at an exhaust steam temperature of 57 °C, considering evaporative water cooling as the cooling method

SEC LT-MED +TVC (kWh/m³)	SEC RO (kWh/m³)									
	3.5		4		4.5		5		5.5	
	LT-MED +TVC	RO	LT-MED +TVC	RO	LT-MED +TVC	RO	LT-MED +TVC	RO	LT-MED +TVC	RO
1.4	29.8	31.4	29.8	30.9	29.8	30.5	29.8	30.1	**29.8**	**29.7**
1.6	29.6	31.4	29.6	30.9	29.6	30.5	29.6	30.1	29.6	29.6
1.8	29.4	31.4	29.4	30.9	29.4	30.5	29.4	30.0	29.4	29.6
2.0	29.3	31.3	29.3	30.9	29.3	30.4	29.3	30.0	29.3	29.6
2.2	29.1	31.3	29.1	30.9	29.1	30.4	29.1	30.0	29.1	29.6
2.4	28.9	31.3	28.9	30.8	28.9	30.4	28.9	30.0	28.9	29.5

Table 6.12 Overall efficiencies of the systems PT-CSP + LT-MED + TVC and PT-CSP + RO at an exhaust steam temperature of 37 °C, considering once-through as the cooling method

SEC LT-MED +TVC (kWh/m³)	SEC RO (kWh/m³)									
	3.5		4		4.5		5		5.5	
	LT-MED +TVC	RO	LT-MED +TVC	RO	LT-MED +TVC	RO	LT-MED +TVC	RO	LT-MED +TVC	RO
1.4	28.8	33.1	28.8	32.6	28.8	32.1	28.8	31.6	28.8	31.2
1.6	28.6	33.1	28.6	32.6	28.6	32.1	28.6	31.6	28.6	31.1
1.8	28.4	33.0	28.4	32.5	28.4	32.0	28.4	31.6	28.4	31.1
2.0	28.2	33.0	28.2	32.5	28.2	32.0	28.2	31.5	28.2	31.1
2.2	28.0	33.0	28.0	32.5	28.0	32.0	28.0	31.5	28.0	31.0
2.4	27.8	33.0	27.8	32.4	27.8	31.9	27.8	31.5	27.8	31.0

Table 6.13 Overall efficiencies of the systems PT-CSP + LT-MED + TVC and PT-CSP + RO at an exhaust steam temperature of 57 °C, considering once-through as the cooling method

SEC LT-MED +TVC (kWh/m³)	SEC RO (kWh/m³)									
	3.5		4		4.5		5		5.5	
	LT-MED +TVC	RO	LT-MED +TVC	RO	LT-MED +TVC	RO	LT-MED +TVC	RO	LT-MED +TVC	RO
1.4	29.8	31.0	29.8	30.6	29.8	30.2	29.8	29.9	**29.8**	**29.5**
1.6	29.6	31.0	29.6	30.6	29.6	30.2	29.6	29.8	**29.6**	**29.5**
1.8	29.4	31.0	29.4	30.6	29.4	30.2	29.4	29.8	29.4	29.4
2.0	29.3	31.0	29.3	30.6	29.3	30.2	29.3	29.8	29.3	29.4
2.2	29.1	31.0	29.1	30.6	29.1	30.2	29.1	29.8	29.1	29.4
2.4	28.9	30.9	28.9	30.5	28.9	30.1	28.9	29.7	28.9	29.4

Table 6.14 Overall efficiencies of the systems PT-CSP + MED-TVC and PT-CSP + RO at an exhaust steam temperature of 37 °C, considering dry cooling as the cooling method

SEC TVC-MED (kWh/m^3)	SEC RO (kWh/m^3)									
	3.5		4		4.5		5		5.5	
	TVC-MED	RO	TVC-MED	RO	TVC-MED	RO	TVC-MED	RO	TVC-MED	RO
1.2	27.6	31.9	27.6	31.4	27.6	31.0	27.6	30.5	27.6	30.1
1.4	27.4	31.9	27.4	31.4	27.4	30.9	27.4	30.5	27.4	30.0
1.6	27.1	31.9	27.2	31.4	27.2	30.9	27.2	30.5	27.2	30.0
1.8	27.0	31.9	27.0	31.4	27.0	30.9	27.0	30.4	27.0	30.0
2.0	26.8	31.8	26.8	31.3	26.8	30.9	26.8	30.4	26.8	30.0
2.2	26.6	31.8	26.6	31.3	26.6	30.8	26.6	30.4	26.6	29.9

Table 6.15 Overall efficiencies of the systems PT-CSP + MED-TVC and PT-CSP + RO at an exhaust steam temperature of 57 °C, with dry cooling as cooling method

SEC TVC-MED (kWh/m^3)	SEC RO (kWh/m^3)									
	3.5		4		4.5		5		5.5	
	TVC-MED	RO	TVC-MED	RO	TVC-MED	RO	TVC-MED	RO	TVC-MED	RO
1.2	27.4	29.9	27.4	29.5	27.4	29.2	27.4	28.8	27.4	28.5
1.4	27.2	29.9	27.2	29.5	27.2	29.2	27.2	28.8	27.2	28.4
1.6	27.1	29.9	27.1	29.5	27.1	29.1	27.1	28.7	27.1	28.4
1.8	26.9	29.9	26.9	29.5	26.9	29.1	26.9	28.7	26.9	28.4
2.0	26.8	29.9	26.8	29.5	26.8	29.1	26.8	28.7	26.8	28.4
2.2	26.6	29.9	26.6	29.5	26.6	29.1	26.6	28.7	26.6	28.3

Table 6.16 Fresh water flow rate (F_{FW}) needed in the condenser of the power cycle with evaporative water cooling

	CSP + RO	CSP + LT-MED	CSP + LT-MED + TVC
F_{FW} (m^3/day)	4078	0	381

Table 6.17 Power consumed by the condenser (P_{cond}) of the power cycle and of the MED plants in the case of using once-through as cooling method

	CSP + RO	CSP + LT-MED	CSP + LT-MED + TVC
P_{cond} (MW_e)	1.25	0.42	0.70

References

Blanco-Marigorta, A. M., Sánchez-Henríquez, M. V., & Peña-Quintana, J. A. (2011). Exergetic comparison of two different cooling technologies for the power cycle of a thermal power plant. *Energy, 36*, 1966–1972.

El-Dessouky, H., & Ettouney, H. (2002). *Fundamentals of salt water desalination* (1st ed.). Amsterdam, The Netherlands: Elsevier Science.

Geyer, M., Herrmann, U., Sevilla, A., Nebrera, J. A., & Zamora, A. G. (2006, June 20–23). *Dispatchable solar electricity for summerly peak loads from the solar thermal projects Andasol-1 & Andasol-2*. In: Proceedings of 13th SolarPACES Symposium, Seville, Spain.

Goebel, O. (2010, September 21–24). *Shams One 100 MW CSP plant in Abu Dhabi. Update on projects status*. In: Proceedings of 16th SolarPACES symposium, Perpignan, France.

IDA. (2013). *IDA desalination yearbook 2012–2013: Water desalination report*. Topsfield, MA: Global Water Intelligence/International Desalination Association.

Klein, S. A., Alvarado, F. L., & Beckman, W. A. (1997). *Engineering Equation Solver (EES), Mc Version 4.447*. F-Chart Software. Middleton, WI.

NREL. (2010). System advisor model (SAM). National Renewable Energy Laboratory. Retrieved from https://sam.nrel.gov/cost

Palenzuela, P., Zaragoza, G., Alarcón-Padilla, D. C., Guillén-Burrieza, E., Ibarra, M., & Blanco, J. (2011a). Assessment of different configurations for combined parabolic-trough (PT) solar power and desalination plants in arid regions. *Energy, 36*, 4950–8.

Palenzuela, P., Zaragoza, G., Alarcón-Padilla, D. C., & Blanco, J. (2011b). Simulation and evaluation of the coupling of desalination units to parabolic-trough solar power plants in the Mediterranean region. *Desalination, 281*, 379–87.

Palenzuela, P., Hassan, A. S., Zaragoza, G., & Alarcón-Padilla, D. C. (2014). Steady state model for multi-effect distillation case study: Plataforma Solar de Almería MED pilot plant. *Desalination, 337*, 31–42.

Richter, C., Dersch, J. et al. (2009, September 15–18). *Methods for reducing cooling water consumption in solar thermal power plants*. In: Proceedings of the 15th SolarPACES Conference, Berlin, Germany.

Richter, C., & Dersch, J. (2010, June 29). *Wasserverbrauch und Wassereinsparung bei solarthermischen Kraftwerken*. Presentation at the DLR 13th solar conference, Cologne, Germany. DLR, Cologne

Short, W., Packey, D.J., & Holt, T. (1995). *A manual for the economic evaluation of energy efficiency and renewable energy technologies* (NREL/TP-462-5173). Golden, Co: National Renewable Energy Laboratory. Retrieved June 29, 2015, from http://www.nrel.gov/docs/legosti/old/5173.pdf

Taylor, B. N., & Kuyatt, C. E. (1994). *Guidelines for evaluating and expressing the uncertainty of NIST measurement results* (Technical Note 1297). Gaithersburg, MD: National Institute of Standards and Technology.

Trieb, F., Kronshage, S., Quaschning, V., Dersch, J., Lerchenmüller, H., Morin, G., et al. (2004). *SOKRATES-Projekt: Solarthermische Kraftwerkstechnologie für den Schutz des Erdklimas*. Stuttgart, Germany: DLR.

Trieb, F. (2007). *Concentrating solar power for seawater desalination* (Aqua-CSP study report). Stuttgart, Germany: DLR (German Aerospace Center).

US DoE. (2009). *Concentrating solar power commercial application study: Reducing water consumption of concentrating solar power electricity generation*. Washington, DC: U.S. Department of Energy.

Zarza, E. (1991). *Solar thermal desalination project, first phase results and second phase description* (1st ed.). Madrid, Spain: CIEMAT.

Index